Brain source localization using SEEG recordings

Vairis Caune

UNIVERSITÉ DE LORRAINE

École doctorale IAEM Lorraine

Brain source localization using SEEG recordings

THÈSE

présentée et soutenue publiquement le 18 juillet 2017

pour l'obtention du

Doctorat de l'Université de Lorraine

Mention Automatique, Traitement du Signal et des Images, Génie Informatique

par

Vairis Caune

Composition du jury

Rapporteurs :	Régine Le Bouquin Jeannes	LTSI UMR 1099 INSERM, Université de Rennes 1
	Olivier Meste	I3S UMR 7271 CNRS, Université Nice Sophia Antpolis
Examinateurs :	Philippe Derambure	Troubles cognitifs dégénératifs et vasculaires, U1171 INSERM, Université de Lille
	Valérie Louis Dorr	CRAN UMR 7039 CNRS, Université de Lorraine
	Steven Le Cam	CRAN UMR 7039 CNRS, Université de Lorraine
	Radu Ranta	CRAN UMR 7039 CNRS, Université de Lorraine
Invités :	Louis Maillard	CRAN UMR 7039 CHRU Nancy, CNRS, Université de Lorraine
	Laurent Koessler	CRAN UMR 7039 CNRS, Université de Lorraine

Centre de Recherche en Automatique de Nancy
UMR 7039 CNRS – Université de Lorraine

2 avenue de la forêt de Haye 54516 Vandœuvre-lès-Nancy
Tél +33 3 83 59 59 59 — Fax +33 (0)3 83 59 56 44

To Uldis and Inga.

Acknowledgements

I would like to acknowledge the hundreds of individuals who have spent their time, nerves and patience to help this work to become a reality. And I mean it.

The biggest of thanks goes to Radu Ranta for getting me into this madness in the first place. We have known each other now for 10 years and I have learned a lot from him. Both his compassion and work ethics is something I can learn from. Together with Steven Le Cam they have restlessly poked me to improve the scientific additions this thesis can bring. Thank you Valérie Louis-Dorr, my supervisor who did not give up on me no matter what. Together all three of them took care of me and Gundars (including finding some beds for us to sleep on when we arrived in an empty French apartment). And of course, thanks to Juris Zagars for sustaining a collaboration between Ventspils and Nancy.

The warmest of thanks to Zane for sticking with me for this last year when it seamed often that I am in another universe and not here. I hope this toughest test will bear its fruits and we can laugh together about it in 50 years, sitting under an apple tree.

The workplace you are in plays an important role. The greatest of thanks to Christine Pierson who gave her fair share of nerves because of me (be it all documents stolen or just plain desperation towards the madness that is French paperwork). Also José Ragot who has always surprised me with the energy that he has and the positive energy that he brings to the workplace. And not to forget Alain and his predecessor Jean-Marie for brightening up the day in office near me.

Big thanks to Louis MAILLARD and Laurent KOESSLER for they priceless input about the medical aspects of the brain and the collaboration between CHRU and CRAN.

I have had quite a lot of office mates and colleagues during my time in CRAN. Thank you Gilles, Benoit, Bruno, Zhenja, Rebeca and Hugo, Raquel, Michelle, Julien, Harry, Tonio and all the others I might not remember now, but I feel thankful to. Thanks to my Latvian colleagues and friends Janis and Gundars (with whom I now work together on beautiful and interesting projects).

Special thanks to Marcos, who was always there for me. Bros be bros.

When I arrived to Nancy the first time, I was lost in translation. Luckily, the person I approached, was Gabriel. Since then we have become close friends. He introduced me to BDE of the time and they were my bridge to get familiar with French culture and appreciate the people there. Thanks to Gabriel, Alice, Xavier, Polo, Gonzi, Bob and all the other team.

Apartment adventures have been rich as well. Thanks to Janis, Juris, Gundars, Paul, Sylvain, Rajiv and Jeanne for bearing with me.

Another special thanks to Rajiv Rughoo – we met once and have travelled to all the sorts of situations since. A great friend and a great person.

Thanks to my Ingress family. Thank you Loirotte for helping me with the LaTeX document you are reading now. Thanks to Rico for supporting me when I was left with hard choices and letting me stay with him and his family.

Thanks to all the great people, who were ready to help me or helped me with proofreading some parts of the thesis – Maruta, Sniedze, Anthony, Anne-Cecile, Rajiv and others that I have forgotten at this very moment.

Finally, thanks to all the members of the jury – Régine Le Bouquin Jeannes, Olivier Meste, Valérie Louis Dorr, Steven Le Cam, Radu Ranta, Louis Maillard and Laurent Koessler. Special thanks to Régine Le Bouquin Jeannes for providing all the corrections that helped significantly to improve the quality of the manuscript.

Thank you all for believing in me even in the moments when I did not believe in myself. A great victory in this war we call life.

Contents

List of Figures

List of Tables

Glossary

BEM Boundary Element Method

BM Bipolar Montage

BOLD Blood Oxygenation Level Dependent

BSS Blind Source Separation

CRM Common Reference Montage

CSL cerebrospinal fluid

CT Computed Tomography

ECD Equivalent Current Dipole

ECG Electrocardiography

ECoG ElectroCorticoGraphy

EEG Electroencephalography

EEG-HR High Resolution EEG

EMG Electromyography

EOG Electrooculography

ESI Electrical Source Imaging

FEM Finite Element Method

fMRI functional MRI

GEVD Generalized Eigenvalue Decomposition

GOF Goodness of Fit

ICA Independent Component Analysis

ICS Intracerebral stimulations

IHM Infinite Homogenous Medium

LORETA low-resolution brain electromagnetic tomography

MEG Magnetoencephalography

MN Minimum Norm

MPDR minimum power distortionless response

MRI Magnetic Resonance Imaging

MUSIC MUltiple SIgnal Classification

MVDR minimum variance distortionless response

OSM One Sphere Medium

PC Personal Computer

PCA Principal Component Analysis

PDE partial differential equation

PET Positron Emission Tomography

RAP-MUSIC Recursively Applied and Projected MUSIC

SEEG Stereo-Electroencephalography

SNR Signal-to-Noise Ratio

SPECT Single-Photon Emission Computed Tomography

SQP sequential quadratic programming

Résumé en français

Contexte et objectifs

Le fonctionnement du cerveau repose sur des processus neuronaux complexes qui nécessitent d'être analysés à différentes échelles spatiales et temporelles, afin de pouvoir décoder l'activité cérébrale de la cellule neuronale jusqu'à son fonctionnement structurel global. Cette complexité est principalement liée à la constitution du cerveau: de l'ordre de cent mille neurones pour l'espèce humaine, soit cent mille milliards de synapses. Les structures neuronales sont organisées en réseaux interconnectés, et le cerveau peut ainsi être décrit comme un système mettant en œuvre des tâches collaboratives, cognitives, réflexives et comportementales, dont les mécanismes sous-jacent restent largement inconnus. Comprendre la dynamique temporelle entre les structures impliquées dans un réseau fonctionnel ou pathologique est fondamental pour comprendre le fonctionnement du cerveau et est un pas décisif dans la résolution de questions neuroscientifiques fondamentales.

Différentes techniques d'imagerie cérébrale et d'instrumentation de mesure électrophysiologique ont été développées pour l'exploration du cerveau humain. Le choix de l'utilisation de l'une ou l'autre technique d'exploration dépend notamment des échelles spatiales et temporelles requises pour l'étude du phénomène que l'on se propose d'étudier. Parmi les modalités disponibles, l'électroencéphalographie (EEG) et la magnétoencéphalographie (MEG) sont d'un intérêt de premier ordre de part la résolution temporelle élevée qu'elles fournissent, permettant d'analyser la dynamique à l'échelle des processus neuronaux. Les deux modalités ont l'avantage d'être non invasives et théoriquement capables de mesurer les activités électromagnétiques cérébrales dans les structures profondes. De nombreuses études ont été réalisées à partir de la MEG/EEG pour la localisation de sources cérébrales (y compris à partir d'enregistrements simultanés EEG/MEG), et les dernières avancées dans ce domaine permettent d'obtenir des qualités de reconstructions spatiales et temporelles de plus en plus précises. Cependant, l'imagerie de source électrique (ESI) à partir de mesures non invasives souffre toujours d'un manque de résolution spatiale du fait du positionnement surfacique des capteurs, et sont notamment connus pour être biaisés par la présence de sources profondes. En outre, en particulier dans le cas de l'EEG, le rapport signal sur bruit (SNR) peut être très faible en raison de l'atténuation de l'os du crâne et des sources externes d'artefact. En effet, les enregistrements peuvent être impactés par des sources non cérébrales, tels que les signaux électro-cardiographiques (ECG), les activités Musculaire Electro-myographique (EMG) ou les activités électro-oculographiques (EOG). Ainsi, les sources d'intérêts peuvent être masquées par ces composantes parasites, surtout dans le cas où les sources à reconstruire sont profondes. Les étapes de pré-traitement sont de ce fait fortement requises (*eg*, filtrage, ICA (Independent Component Analysis)), mais peuvent corrompre le signal d'intérêt lui-même.

L'objectif principal de cette thèse est d'utiliser les enregistrements invasifs afin de localiser les sources. Nous nous intéressons en particulier à la Stereo-électroencéphalographie (SEEG), qui consiste à implanter des aiguilles d'électrodes dans le volume cérébrale afin d'explorer au plus près les générateurs des structures profondes. Cette modalité est mise en œuvre dans la cas de patients épileptiques pour lesquels les solutions pharmaceutiques sont inefficaces. Son rôle est généralement limité à l'évaluation clinique dans le but de confirmer la localisation de la zone épileptique responsable de la pathologie. En effet, l'interprétation neurologique classique des signaux SEEG est basée sur l'hypothèse qu'ils contiennent une information purement ou très largement locale: les capteurs étant très proches des sources, l'effet de la conduction volumique se retrouverait fortement diminué, voir annulé. En pratique cependant, les signaux montrent de fortes corrélations entre eux, et ce constat persiste même après avoir éliminé la référence commune. Pour s'assurer du caractère local des signaux et faciliter leur interprétation, les neurologues transforment le montage en référence commune en montage bipolaire. Notre approche propose de revenir aux mesures en référence commune, prendre en compte la conduction volumique et donc la propagation et le mélange de sources présentes également en SEEG, et les exploiter pour estimer les sources dipolaires équivalentes en résolvant un problème inverse, comme en EEG de surface. Cette manière d'approcher les signaux EEG de profondeur a été très peu exploitée dans la littérature, et la problématique spécifique liée à l'échantillonnage spatiale particuliere en SEEG et aux modèles de propagation adaptés n'a jamais été abordée de manière détaillée. Cette section présente donc nos travaux dans ce domaine, avec un fort accent sur l'influence de ces spécificités sur les performances d'estimation de sources.

La modalité SEEG présente de précieux avantages. En effet, les électrodes sont directement placés dans les populations neuronales où résident les sources à localiser, fournissant un rapport signal à bruit très favorable par rapport à l'EEG. Néanmoins, l'utilisation de cette modalité pour la résolution du problème inverse est loin d'être immédiate, plusieurs points sensibles doivent être analysés. Tout d'abord, la disposition spatiale des électrodes pose la question du conditionnement du problème. En effet, les aiguilles d'électrodes sont implantées en cluster dans la zone supposée contenir les sources d'intérêt, contrairement à la modalité EEG qui couvre de manière homogène l'ensemble du volume cérébral. Ainsi, l'identifiabilité de l'espace source doit être étudiée. Étant donnée une disposition des électrodes SEEG, l'ensemble des contacts à retenir pour garantir une localisation fiable des sources est également une question ouverte. Nous souhaitons en particulier quantifier la fiabilité du processus de localisation dans des contextes de rapport source/bruit réalistes (SNR) et à identifier les zones de confiance (en termes de distance par rapport aux capteurs).

Structure de la thèse, développements et résultats

Chapitre 1 - L'électrophysiologie du cerveau

Le premier chapitre de la thèse consiste en une introduction générale sur l'organisation du cerveau et sur la génération de l'activité cérébrale électromagnétique. La section 1.1 fournit une brève description des structures cérébrales majeures, et en particulier des couches corticales et sous-corticales, qui sont le siège de l'activité cérébrale. Un aperçu des principales fonctions cérébrales est présenté, avant que ne soit introduite la cellule constitutive élémentaire du cerveau: le neurone. Nous expliquons ensuite comment les ensembles de populations neuronales interconnectées donnent naissance au champ électromagnétique, et nous décrivons les principales caractéristiques électro-

physiologiques observées lors de fonctionnement normaux et pathologiques du cerveau. L'activité rencontrée lors d'événements épileptiques des structures temporales est plus particulièrement détaillée. Pour terminer ce chapitre, les principaux outils de neuro-imagerie utilisés à ce jour pour l'exploration du cerveau sont présentées. Nous commençons par une description rapide des modalités d'imagerie anatomo-fonctionnelles couramment utilisée, puis nous introduisons le lecteur aux méthodes de mesures de l'activité électro-magnétique. Une section plus importante est dédiée aux mesures stéréo-électroencephalographiques (SEEG) qui nous intéresse plus particulièrement dans cette thèse (invasive stereo-electroencephalographic) explorées dans cette thèse pour la localisation de sources cérébrales électriques.

Chapitre 2 - L'imagerie de sources cérébrales

La localisation de sources à partir de mesures électromagnétiques est un champ de recherche actif depuis les années 1950 et repose sur plusieurs étapes importantes, à commencer par la modélisation des sources et la résolution du problème direct, reliant les activités sources aux potentiels mesurés sur les capteurs. Dans cet objectif, le choix d'un modèle de propagation physique est déterminant, conditionnant fortement le succès et la précision de la localisation. La première partie de ce chapitre présente ainsi différents modèles de propagation, en traitant de leurs avantages et de leurs inconvénients.

Outre la géométrie du modèle (tête, crâne, cerveau de formes plus ou moins précises), la connaissance précise des positions spatiales des capteurs est également requise. Différentes solutions commerciales existent pour la détermination de la position des capteur EEG sur le cuir chevelu. Dans le cas d'enregistrements SEEG, les positions des capteurs ne sont pas directement accessibles et doivent être déterminées à partir des examens d'imagerie (CT-Scan) du patient. Nous décrivons brièvement ici la procédure de recalage développée récemment par notre équipe.

Sur la base de ces conditions préalables de modélisation, le problème inverse de localisation de sources est ensuite présenté. Un aperçu des approches les plus populaires pour résoudre ce problème est donné, ainsi que des détails sur les algorithmes d'optimisation couramment utilisés. Les mesures du potentiel électrique SEEG étant au centre de cette étude, une partie de ce chapitre est consacrée à une discussion sur la spécificité de cette modalité en matière de localisation des sources cérébrales. Enfin, les étapes importantes de pré-traitement nécessaires pour l'application sur données réelles sont présentées, y compris l'étape de re-référencement, le débruitage du signal, ainsi que la sélection des événements d'intérêt et l'amélioration de leur rapport signal à bruit.

Chapitre 3 - Localisation en SEEG: étude de faisabilité

Le troisième chapitre est essentiellement exploratoire: nous évaluons en simulation la faisabilité de la localisation, avec une méthode de résolution de problème inverse bien connue (approche dipôle équivalent) mais adaptée au contexte SEEG (modèle de propagation simplifié, mauvais échantillonnage spatial des capteurs). Nous nous sommes intéressés à un problème en principe simple: localiser une source dominante à partir des mesures SEEG possiblement bruitées, avec un modèle de propagation simplifié et un échantillonnage spatial de la mesure irrégulier et éparse. Le problème à minimiser s'écrit alors pour un seul dipôle dominant paramétré par sa position $\boldsymbol{r}_1$ et ses moments élémentaires $\bar{\mathbf{d}}_1$:

$$\{\hat{\boldsymbol{r}}_1, \hat{\bar{\mathbf{d}}}_1\} = \arg\min \|\mathbf{V} - \mathbf{k}(\boldsymbol{r}_1)\bar{\mathbf{d}}_1\| \tag{1}$$

Comme mentionné précédemment, deux aspects principaux sont à prendre en compte pour la localisation de sources à partir de mesures SEEG: le modèle de propagation (le problème direct) et l'emplacement des capteurs et leur échantillonnage spatial.

Comparaison de modèles (section 3.2)

Dans un premier temps, nous avons ainsi mené une étude comparative de modèles directs. La question posée est simple: sachant que les modèles (numériques) détaillés dépendent de beaucoup de paramètres difficiles à mesurer avec précision (géométrie, conductivités), est-il plus judicieux d'utiliser des modèles analytiques simples? On peut considérer que la SEEG se trouve à mi-chemin entre l'EEG de surface et les enregistrements à micro-électrodes. En effet, comme l'EEG, la SEEG enregistre des sources macroscopiques, *i.e.*, des populations de neurones synchronisés; on peut supposer un milieu de propagation relativement homogène et isotrope, du moins quand les capteurs et les sources sont suffisamment loin des frontières entre le cerveau et le crâne. Est-il donc possible d'utiliser des modèles homogènes infinis (IHM), ou alors avec une frontière analytique (modèles à une sphère, OSM) pour résoudre efficacement et de manière suffisamment précise le problème de localisation?

Pour répondre à ces questions, nous avons comparé en simulation deux modèles analytiques simples (Infinite Homogeneous Model (IHM) et One Sphere Model (OSM)) à un modèle numérique à géométrie réaliste (Finite Element Model (FEM)). Afin de faire une analyse exhaustive et réaliste, nous avons utilisé un modèle numérique moyen de tête (*Adult MNI-ICBM152 Head Model Package* de l'UCL).

Les erreurs de modèle ont été calculé pour trois dipôles $S1$, $S2$, $S3$, un dipôle profond, un dipôle intermédiaire et un dipôle superficiel. Globalement, l'OSM donne de meilleur résultat que l'IHM et l'erreur est relativement faible autour du dipôle, dans un rayon de quelques centimètres. Autrement dit, on peut s'attendre à des résultats de localisation corrects même en utilisant des modèles simples, en particulier pour l'OSM lorsque les capteurs utilisés ne sont pas très loin de la source recherchée.

Localisation: optimisation, configurations et résultats (sections 3.3 et 3.4)

Optimisation. La localisation par maximisation du GOF/minimisation de l'erreur (1) d'un modèle analytique simple est faisable (surtout pour l'OSM), mais la non-convexité du problème peut conduire vers des minima locaux. Nous avons opté pour une méthode relativement classique d'optimisation sous contrainte. Il s'agit de la méthode itérative SQP (*sequential quadratic programming*), la contrainte étant donnée sur trois des 6 paramètres à optimiser, notamment sur la position $\hat{\boldsymbol{r}}$ du dipôle dominant recherché (1):

$$\|\hat{\boldsymbol{r}}\| < R$$

avec R le rayon de la sphère du modèle OSM ajusté sur le maillage du cerveau.

Etant donné l'aspect non convexe de la fonction à optimiser, la solution classique est l'utilisation de plusieurs initialisations, qui vont converger vers des minima locaux possiblement différents, parmi lesquels on choisira celui qui maximise le GOF. Nous avons donc proposé de répartir de manière équilibrée N points d'initialisation dans la sphère du modèle OSM, en passant par une méthode de minimisation de la s—énergie de Riesz.

Configuration des capteurs. L'analyse des erreurs de modèle montre que, si on veut utiliser un modèle simple, il n'est pas toujours souhaitable d'optimiser le GOF sur l'ensemble des points de mesure possibles, et que les erreurs sont en général plus faibles dans le voisinage du dipôle (sauf quand on s'approche trop des frontières). D'autre part, il est aussi évident que, pour des signaux bruités et surtout en présence d'activités cérébrales autres que le dipôle dominant (ce qu'on peut assimiler à du bruit spatialement coloré), il est préférable d'utiliser dans la procédure d'optimisation les points de mesure proches de la vraie position du dipôle (certes, inconnue avec précision), car le rapport signal/ bruit sera nécessairement meilleur. Avec ces considérations en tête, nous avons proposé plusieurs manières possibles de configurer le problème d'optimisation, *i.e.*, la recherche des paramètres du dipôle dominant, notamment en choisissant un nombre limité d'électrodes à utiliser:

- les 6 électrodes qui enregistrent le potentiel le plus grand en valeur absolue (*i.e.*, proche du dipôle dominant, sans être dans le plan orthogonal à son orientation), en partant de l'hypothèse qu'on a besoin de 6 équations pour estimer les 6 paramètres dipolaires;
- l'ensemble d'électrodes situées dans l'hémisphère cérébral supposé du dipôle recherché (ipsi-latéral);
- l'ensemble d'électrodes situées dans l'hémisphère cérébral opposé (contra-latéral);
- toutes les électrodes disponibles.

Les localisations ont été faites en utilisant les deux modèles analytiques (IHM et OSM), avec et sans bruit. Dans le cas sans bruit, le modèle OSM est plus fiable que le modèle IHM. Comme attendu, Les dipôles de l'hémisphère mieux implanté sont mieux localisés (sauf configuration contra-latérale où le nombre d'électrodes est réduit). Une localisation avec 6 capteurs n'est pas suffisante en général, même si parfois on obtient des très bons résultats (analyse non détaillée ici). Une localisation avec des électrodes situées dans l'hémisphère opposé est en général hasardeuse, alors qu'une localisation avec les électrodes ipsi-latérales est comparable à une localisation avec des électrodes dans les deux hémisphères, voire meilleure dans l'hémisphère bien implanté (*i.e.*, les électrodes supplémentaires dans l'hémisphère opposé améliorent relativement peu, voir pas, les résultats). Ce dernier point est important car, dans le cas bruité, on peut s'attendre même à une dégradation des performances si on inclut des capteurs trop éloignés, avec un très mauvais RSB.

Pour le cas bruité, nous avons uniquement évalué les performances des meilleures configurations du cas non-bruité, *i.e.*, la localisation effectuée avec le modèle OSM et les configurations de capteurs ipsi-latéraux et tous les capteurs. La conclusion générale est la même: il vaut mieux utiliser les électrodes proches, mais en nombre suffisant, que d'utiliser l'ensemble de mesures disponibles.

Cette étude en simulation montre que la localisation d'un dipôle dominant à partir de mesures intra-cérébrales SEEG est possible. Elle peut avoir des conséquences pratiques importantes, comme la réduction du nombre d'électrodes implantées dans le cerveau ou la définition d'un emplacement optimisé.

Résultats sur signaux réels (section 3.5)

La méthode de localisation est appliquée et évaluée sur des enregistrements SEEG réels issus du CHRU de Nancy. Deux types de signaux sont présentés: la SEEG enregistré au cours de séance de stimulation intra-crânienne (ICS),

donc dans le cas d'un générateur connu, ainsi que des enregistrements SEEG correspondant à une séquence de pointes épileptiques inter-critiques.

Nous avons testé notre procédure de localisation pour trois sites de stimulation: profonde, intermédiaire et superficielle. De façon général, nous concluons que la configuration ipsi-latérale offre les meilleures performances de localisation, avec des erreurs de position inférieures à 9mm et des erreurs d'orientation inférieures à 22.4 degrés (indépendamment de la position de la source ICS et du modèle utilisé pour l'inversion (IHM ou OSM)). Si nous nous concentrons sur les dipôles profonds et intermédiaires, l'utilisation de l'ensemble des capteurs fournit également de bons résultats (erreurs inférieures à 10mm), mais cette configuration de capteurs montre ses limites en considérant la source ICS la plus externe, motivant la recherche d'un sous-ensemble de capteurs pour une localisation plus fiable.

Dans le cas des signaux épileptiques réels, les résultats sont également très convaincants: après avoir éliminé l'électrode sur laquelle les pointes présentent une amplitude maximale (electrode R' permettant de situer cliniquement le site de la source en montage bipolaire), la localisation a été faite en utilisant les deux modèles analytiques (IHM et OSM), après avoir sélectionné et moyenné plus de 20 pointes afin d'améliorer le Rapport Signal à Bruit (RSB). Les résultats sont très similaires et très précis: la source est localisée à moins de 5mm du contact présentant l'amplitude la plus élevée (R'6), et dans la même structure anatomique. Nous montrons également qu'une augmentation du nombre de pointes considérées dans la moyenne améliore le SNR, et donc la précision de localisation. En revanche, lorsque le nombre de pointes disponibles est faible, nous montrons qu'une une configuration de capteur adéquate proche de la source améliore sensiblement le résultat.

Chapitre 4 - Développement d'une approche locale

En se basant sur les expériences menées dans le chapitre précédent, nous avons extrait plusieurs observations sur l'ensemble adéquat de capteurs à choisir. Tout d'abord, l'utilisation de l'ensemble des capteurs disponibles ne garantit pas de fournir les meilleurs résultats de localisation. Si dans les cas sans bruit et bruit blanc additif l'utilisation de l'ensemble des capteurs semble en effet être le meilleur choix (malgré l'imprécision du modèle utilisé pour l'inversion (OSM vs FEM)), nous avons souligné la supériorité de l'utilisation restreinte aux capteurs ipsi-latéral dans le contexte plus réaliste du bruit corrélé, c'est-à-dire lors de co-occurrences de sources de bruits physiologiques. Cela indique qu'un choix judicieux des capteurs peut avoir un impact significatif sur la précision et la robustesse de la localisation. En effet, l'utilisation de capteurs proches de la source garantit un rapport signal à bruit plus élevé et écarte les mesures éloignées susceptibles d'être corrompues par d'autres activités.

D'autre part, dans le chapitre précédent, il a également été souligné qu'un nombre minimum de capteurs est nécessaire pour obtenir des résultats de localisation satisfaisants, avec une précision accrue lorsque le dipôle est entouré de capteurs. Un compromis est donc à trouver entre la proximité des capteurs, le nombre de capteurs ainsi que leur répartition spatiale.

Approche locale: les conditions nécessaires (section 4.1)

La limitation de l'étendue spatiale des capteurs utilisés garantit que les capteurs ayant le SNR le plus élevé sont utilisés pour localiser la source, cependant un nombre de capteurs suffisant est requis pour fiabiliser les résultats. Ces observations motivent l'introduction d'un critère de répartition prenant en compte ce compromis, basé sur la notion

de conditionnement spatial et calculé comme le rapport entre l'axe le plus long et le plus court du plus petit parallélépipède rectangle dans lequel s'inscrit l'ensemble des capteurs sélectionnés. Plus ce facteur de conditionnement est bas, plus le nuage de capteurs est équilibré. Un rapport de un est associé à une répartition équilibrée dans chaque direction (les capteurs sont inclus dans un cube), tandis qu'un rapport élevé est associé à un nuage presque limité à un plan 2D. Toujours en considérant un modèle FEM pour le problème direct et un modèle OSM pour résoudre le problème inverse, et en considérant successivement chacune des 509 positions dipolaires, l'algorithme de localisation est appliquée en utilisant des sous-ensembles de capteurs de tailles croissantes, en commençant par les capteurs les plus proches de la position de la source. Le critère de conditionnement est alors calculé pour chaque localisation, et permet d'évaluer la qualité de la localisation en fonction de ce critère.

Dans le cas sans bruit, les meilleurs résultats de localisation sont obtenus pour les valeurs de conditionnement spatiale faible, c'est à dire quand un grand nombre de capteurs est utilisé, comme observé dans le chapitre précédent. Lorsque du bruit coloré est ajouté au mesure, les meilleurs résultats sont obtenus pour des valeurs de conditionnement compris dans l' intervalle $2-3$, avec des médianes autour de 5 mm à 10 mm pour des SNR réalistes. Ces conditionnement correspondent à des nombre de capteurs réduits (il est en effet à noter que l'application du critère de conditionnement spatial à l'ensemble des capteurs donne lieu à une valeur de conditionnement de ≈ 1.9), confirmant la conclusion précédente sur l'importance de réduire l'ensemble de capteurs. Néanmoins pour atteindre de tel niveau de conditionnement, il apparaît que les capteurs doivent être situés sur au moins trois aiguilles d'électrode différentes, et que le nombre de capteurs utilisés doit être conséquent: une médiane de 89 capteurs est obtenue pour des valeurs de conditionnement entre 2 et 3, avec des quartiles inférieur et supérieur égal à 55 et 114 respectivement. Ce résultat traduit bien le compromis entre proximité spatial et nombre de capteurs énoncé ci-dessus.

Nous concluons dans un premier temps qu'un conditionnement inférieur à 3 est requis pour envisager un résultat de localisation fiable. Étant donné ce résultat, une stratégie de sélection de capteurs est établie, consistant à considérer l'ensemble des capteurs les plus proches ayant un conditionnement inférieur à 3. En effet une analyse supplémentaire montre que de meilleurs résultats sont en effet obtenus lorsque, à conditionnement équivalent (et inférieur à 3), l'ensemble des capteurs le plus restreint donne en moyenne les meilleurs résultats. Cette stratégie est évaluée dans la suite du chapitre.

Approache locale et évaluation (section 4.2)

Nous proposons une méthode de localisation en introduisant la stratégie de sélection des capteurs décrites ci-dessus, et résumé dans l'algorithme 1. Elle consiste en un schéma d'optimisation de type dipôle équivalent où à chaque itération est utilisé le sous-ensemble minimal de capteurs bien conditionnés (ratio de conditionnement inférieur à 3 par rapport à la position actuelle estimée du dipôle). Le critère d'optimisation est classique: minimiser $f_{loc}(\ xb)$, défini comme l'erreur quadratique normalisée restreinte aux potentiels du sous-ensemble sélectionné des capteurs les plus proches $\boldsymbol{\phi}^{loc}$ ou, de façon équivalente, maximiser un critère de GOF local GOF_{loc}:

$$\begin{aligned} f_{loc}(\mathbf{x}) &= \frac{\|\boldsymbol{\phi}^{loc} - \boldsymbol{\phi}_0^{loc}(\mathbf{x})\|}{\|\boldsymbol{\phi}^{loc}\|} \\ GOF_{loc}(\mathbf{x}) &= \sqrt{1 - f_{loc}(\mathbf{x})^2} \end{aligned} \tag{2}$$

avec $\boldsymbol{\phi}_0^{loc}(\mathbf{x})$ la projection du dipôle courant sur les capteurs locaux sélectionnés, et $\mathbf{x}$ les paramètres de position et d'orientation du dipôle.

Comme précédemment, nous considérons trois niveaux de bruit coloré (20dB, 10dB et 3dB) ainsi que le cas sans bruit (InfdB), et nous simulons 100 niveaux de bruit pour chaque SNR. Afin de limiter la charge de calcul, nous fixons une orientation radiale pour les 509 dipôles (perpendiculaires à la surface de la sphère). Dans cette partie, il a été également nécessaire de revoir le critère de sélection de la solution finale. Dans le cas de l'algorithme proposé, l'ensemble des 20 solutions obtenus pour chaque localisation (20 multi-start) donnent généralement lieu à des GOF locaux élevés, bien que certaines solutions soient mauvaises. La meilleur solution présente rarement le meilleur GOF local, et cette stratégie de sélection doit être reconsidéré. Les résultats de simulations montrent en effet que la stratégie locale est sensiblement meilleur que celle utilisant l'ensemble des capteurs lorsque la meilleur solution parmi les 20 solutions obtenus est bien sélectionnée, les médianes d'erreur de localisation étant divisé par près d'un facteur 2 dans les cas sans bruit et 20dB (de $\approx$ 6.3mm à $\approx$ 3.5mm en médiane). En revanche lorsque le critère de GOF local est employée en sortie de l'algorithme local proposée, les médianes s'élèvent largement (*e.g.*, au delà de 15mm pour un SNR de 20dB).

Afin de palier à ce problème de sélection de la solution dans le cas de l'approche locale proposée, nous avons établi un critère de GOF hybride conciliant l'adéquation local ainsi que l'adéquation globale à l'ensemble des mesures. En effet ce travail de thèse se place dans le cadre de l'identification d'un dipôle dominant, ce qui implique que la source à identifier doit non seulement expliquer les potentiels sur les capteurs proches qui l'entourent, mais également les mesures obtenus sur les capteurs les plus éloignés. Nous adoptons ainsi une stratégie de sélection en deux étapes: dans un premiers temps les dipôles présentant des GOF locaux trop faibles sont éliminés (où le seuil dépend du niveau de bruit), puis la solution présentant le GOF global maximal parmi les solutions restantes est finalement sélectionnée. Les résultats obtenus avec cette stratégie sont encourageants et permettent de surpasser les performances obtenus lorsqu'une stratégie globale est utilisée. De plus, une bonne robustesse au bruit est obtenu avec une médiane augmentant de 6.0 mm à 6.9 mm lorsuqe le SNR passe de 20dB à 10dB.

Ces résultats restent néanmoins bien en deçà de ceux obtenus lorsque la meilleur solution parmi les 20 est manuellement sélectionné (cas de simulation où la position de la source est connue), et nous terminons cette section en proposant une version où le choix final est laissé au clinicien. En effet nous montrons que la meilleur solution que nous cherchons à sélectionner est contenu dans le sous-ensemble obtenu par filtrage sur le GOF local (où les solutions présentant un GOF local sous le seuil sont éliminées). En simulation, il s'avère que ce sous-ensemble est drastiquement réduit: entre 2 et 4 solutions en médiane sont pré-sélectionnés pour des niveaux de bruit entre 20dB et 10dB. En partant de cet ensemble réduit, le clinicien peut choisir la solution la plus plausible au regard de son expérience et de l'examen clinique préalable du patient, ou encore rejeter l'ensemble des solutions en cas d'indétermination trop importante.

Zones de confiance (section 4.3)

Une dernière section de ce chapitre est dédiée à l'établissement de zones de confiance en fonction d'une implantation d'électrodes donnée. Ceci vise à fournir au clinicien un certain degré de confiance face à un résultat de localisation en fonction de sa distance avec l'électrode la plus proche, afin de l'aider à accepter ou rejeter ce résultat. Nous délimitons ainsi quatre zones différentes du cerveau en termes de distance au nuage de capteurs. La première zone

correspond à une enveloppe de 2cm entourant l'ensemble des capteurs. La seconde zone est l'enveloppe extérieure entre 2 et 3cm, la troisième zone va de 3 à 4cm, et la dernière zone est l'espace extérieur ayant une distance de plus de 4cm aux capteurs.

Pour chaque zone est calculé le pourcentage de *hits*, *i.e.*, le pourcentage de dipôles positionné dans cette zone et bien localisé (moins de 1cm). On donne également le pourcentage de faux-positif pour chaque zone, défini comme le nombre total de mauvaise localisation dans cette zone divisé par le nombre total de dipôles localisés (trouvés par l'algorithme) dans cette zone. Il s'avère que dans le cas où la meilleur solution est choisie manuellement, la méthode locale proposée donne de bien meilleurs résultats de localisation que la méthode utilisant l'ensemble des capteurs. En revanche lorsque la solution finale est choisie à l'aide des GOF (GOF global dans le cas où tous les capteurs sont utilisés et méthode heuristique en deux étapes pour le cas de notre approche locale), les différences s'amenuisent et la supériorité de notre approche est peu évidente.

Néanmoins, Si l'on considère le cas d'un SNR favorable (20dB), il est possible de considérer une zone de confiance allant jusqu'à 3cm (près de 90% des dipôles identifiés dans cette zone vs environ 25% de faux positifs parmi les sources identifiées dans cette zone). En rappelant que ces positions sont déterminées par un échantillonnage régulier du maillage de la matière grise, cela suggère qu'environ 65% du cerveau est couvert par l'implantation de SEEG réaliste adoptée tout au long de cette thèse. En outre, cela signifie que si un point d'une région d'intérêt est à moins de $3cm$ d'un capteur, et si un SNR d'environ 20dB peut être garanti par l'étape de pré-traitement (en faisant la moyenne de plusieurs événements), alors il est possible de placer une confiance raisonnable dans le résultat de localisation obtenu. Cette distance est réduite à 2cm lorsque le rapport signal à bruit est de 10dB, par exemple lorsque l'événement à localiser est d'amplitude faible.

Résultats sur signaux réels (section 4.4)

Nous considérons dans un premier temps que la position de la source à localiser est connue et nous évaluons la performance de la localisation en fonction du nombre de capteurs employés. Cela nécessite bien entendu un cas réel déjà expertisé, et pour cela nous utilisons les pointes épileptiques déjà étudiées dans le chapitre précédent, pour lesquelles la position du dipôle est connue. Lorsque le nombre d'événements de pointes est important, un SNR élevé peut être obtenu, et la sensibilité aux nombres et à l'étendu des capteurs utilisés est réduite. En revanche, lorsque le nombre d'événements à moyenner est réduit, cette exemple montre qu'il faut choisir une configuration de capteur adéquate proche de la source. Pour ce cas réel, un bon compromis (erreur de localisation inférieure à 1cm) est obtenu en faisant une moyenne de 5 à 10 pics (1.1 à 4.2 dB) en utilisant un sous-ensemble de 24 capteurs dans un rayon de 2.5cm autour de la position de la source. L'utilisation de capteurs plus éloignés dégrade ce résultat.

Notre approche locale est ensuite évaluée sur des signaux de stimulation. Dans ce cas de fort RSB, le site de stimulation est localisée de façon satisfaisante avec la stratégie de localisation proposée. Nous sommes confrontés à une situation plus délicate lorsque le site des pics inter-critiques doit être identifié. Premièrement, il semble que l'amélioration du SNR par calcul de la moyenne soit obligatoire pour qu'une solution pertinente puisse être produite. La moyenne de plus de 20 événements permet d'améliorer le SNR de $-3,3$dB à $7,3$dB, représentant toujours un cas de rapport signal/bruit plutôt faible. Cependant, la source étant distante de moins de 1 cm pour les capteurs les plus proches, elle est localisée avec succès dans la plupart des configurations de capteurs. Lorsque moins d'événements sont moyennés (SNR inférieur), les meilleurs résultats de localisation sont en effet obtenus en utilisant un nombre

limité de capteurs entourant la source épileptique (tel qu'identifié par l'expert) en utilisant notre stratégie de sélection de capteur.

Introduction

The brain is a complex process or set of processes that can be studied at different spatial and temporal scales: from the neuronal cell to its overall structural functioning. This complexity is primarily due to its constitution (of the order of one hundred billion of neurons for the human species, or one hundred thousand billion synapses) but also to the extent and nature of its functions. These concern both the regulation of the different functions of the body and the interaction of the latter with the external world. They range from reflex functions to the most complex executive functions. Neurons are activated by transporting ions through the membrane. These neurons constitute an interconnected network and the transmission of information takes place through the synapses. The brain can be described as a collaborative system of sources and interconnected structures dedicated to motor, cognitive, reflective and behavioral tasks, the underlying mechanism of which remains largely unknown. Understanding the temporal dynamics between the structures involved in a given functional network is a key to understand the functioning of the brain and is a decisive step in resolving fundamental neuroscientific issues. Indeed, it is now well established that most functional tasks are not dealt with by a single structure, but rather by organized networks. Learning how these structures exchange information together would be useful to understand the precise role of each for a given task. The primary objective of research on the brain is to understand the disorders caused by functional deficits, ie to diagnose them and to design and adopt the appropriate therapies. It is obvious that more fundamental work on the understanding of cerebral functioning is also a path indirectly contributing to clinical objectives.

Different imaging modalities and measurement techniques are developed to explore the human brain. They are selected according to the spatial and temporal scales required for the studies to be carried out. Among the available modalities, the electroencephalography (EEG) and the magnetoencephalography (MEG) are of primary interest due to the high time resolution they provide, the dynamics of transient epileptic events being of the order of few milliseconds (*e.g.*, epileptic spikes). Both modalities have the advantage to be non-invasive, and are theoretically able to measure deep brain electromagnetic activities from the scalp surface. Numerous studies have been carried out for epileptic source localization from the EEG/MEG (including studies exploiting simultaneous EEG/MEG recordings), and recent developments have reported to provide more and more reliable epileptic source localizations and time-course reconstructions. However, such Electrical Source Imaging (ESI) still suffer from poor spatial resolution: they are known to be prone to depth bias by producing under-estimates of the deep sources. Also, in particular for the EEG modality, the Signal to Noise Ratio (SNR) can be dramatically low due to the attenuation of the skull bone and artefact sources. Multiple activities are impacting the recordings, such as ElectroCardioGraphic (ECG) signals, muscle ElectroMyoGraphic (EMG) activities or ElectroOculoGraphic (EOG) activities (eye blinks). Thus the targeted sources might be completely drawn in these spurious components, especially if they are situated in deep structures.

Pre-processing steps are strongly required (*e.g.*, filtering, Independent Component Analysis (ICA)), because sources may corrupt the signal of interest, thus introducing errors in the localization task.

The main goal of this thesis is to introduce intracerebral recordings as alternative modalities for solving the ESI inverse problem. In particular we focus on the Stereo-Electroencephalographic modality (SEEG), which consists of several electrode shafts implanted within the deep structures of interest, a dozen equally-spaced electrode contacts being spread on each electrode. The SEEG is used in the context of severe epileptic pathological case for which the medication is ineffective. Its role is limited to clinical evaluation for confirming the precise localization of the epileptic zone responsible for the pathology before applying targeted treatments or excision of the identified structures. The recordings are quasi-exclusively used on bipolar montage (difference of two consecutive electrode contacts), thus the extent of observation remains limited to the local area surrounding the electrode contacts, canceling the contribution of far sources. However the SEEG modality has some key advantages that are likely to contribute to the source localization task. Indeed, the electrodes are directly placed within the structure of interest near the sources, guaranteeing favorable Signal to Noise Ratio when compared with EEG. Nevertheless, its use is not straightforward and several sensitive points must be analyzed. First, the electrode shafts are implanted in clusters within the area rumored to contain the sources of interest, unlike the EEG modality which homogeneously cover the whole brain volume, and the identifiability of the source space has to be questioned. Also, this particular implantation of the SEEG (clusters of align contacts) can be at the origin of conditioning problem when the inverse problem is to be solved. The set of contacts to be explored to guarantee a reliable localization with regards to a given SEEG implantation and sources configuration is also an open question. We aim at quantifying the reliability of the localization process depending on realistic Source to Noise Ratio (SNR), and to identify zones of confidence (in terms of distance to the sensors). These issues are tackled in this manuscript following the structure described below.

Chapter 1: Electrophysiology of the human brain

In this introductory chapter, we present the general context of the thesis starting with general knowledge on the brain anatomy and its general functioning, from the functional organization of the main macroscopic structure down to the description of its most elementary cell, the neuron. The main characteristics of the human brain electrophysiology observed during some common functional tasks or during pathological events are described, in particular in the context of temporal lobe epilepsy whose electrophysiologic development along the seizure is well known. An introduction to the main anatomical and functional data acquisition tool commonly used in clinical observation is then presented. We give a particular insight on the Stereo EEG (SEEG) modality and on its particularity with regard to the source localization task, anticipating on the key points that will have to be tackled toward a reliable source localization procedure based on this modality.

Chapter 2: Forward modeling and source localization

Brain source localization relies on the definition of both a source model and a model of the medium (brain tissues) through which the electrical field propagates from the source to the sensors. In this chapter, we recall the common

dipolar source model widely adopted in the EEG/MEG source localization literature. Then we detail the usual technique to compute the projection coefficients of the sources on the sensors (known as the forward model), under the assumption of an instantaneous and linear propagation of the electric field. The analytical models are presented (from the most basic Infinite Homogeneous Medium model to models based on sphere approximations of the head shape), as well as more realistic numerical models based on finite element computation techniques. We continue by giving an overview of some popular methods for brain source localization, starting by these addressing the severely under-determined inversion of distributed models where the whole brain volume is covered with elementary sources. We pursue with the Equivalent Current Dipole (ECD) method which is well adapted when a single dominant source is to be identified, such situation being encountered in the context of epileptic interictal spikes.

Chapter 3: Localization in SEEG: feasibility study

While the ESI problem has been extensively studied from the EEG/MEG modalities, we wish to address the feasibility of this inversion from the SEEG modality. Indeed the specific configuration of this sensor setup, consisting in electrode shafts of aligned sensors, yields the question of the conditioning of the inverse problem in terms of spatial repartition of the sensors and of their distance to the sources. Also in this context of intracerebral recordings we address the question of the needed level of accuracy for the computation of the forward model, and we argue that a One Sphere Medium (OSM) is confident enough at this macroscopic level, taking account of the main conductivity barrier : the skull bone. We then evaluate the performance of a classical ECD approach based on extensive simulations, by trying to identify brain sources with various positions (homogeneously sampling the gray matter) and orientations, and considering several sensor configurations that can be encountered in clinical routine as well as different scenarios of noise (white or correlated). ECD localizations are finally performed on real data of intracerebral stimulation (ICS), for which the position of the electrical source is known, as well as data of interictal spikes recorded within the brain of a patient with lobe temporal epilepsy, and for which the surgery outcomes were successful.

Chapter 4: Local approach for SEEG dipole fitting

Based on the observations and the conclusions made in the **chapter 3**, this fourth chapter aims at proposing a genuine electrodes selection strategy for achieving better source localization accuracy. It appears that a compromise between the number of electrodes and their distance to the source of interest has to be reached toward successful ESI from SEEG. Also a well balanced spatial repartition of the sensors is of importance to provide enough different viewpoints on the actual position of the sources, *i.e.*, a source surrounded by sensors is more easily identified than a source outside the cloud of sensors. We then introduce a spatial conditioning criterion aiming at adequately describing these requirements on the sensor configuration. Under supervised simulation (the position of the source is known), we identify eligible value of this criterion yielding globally the highest source localization performance. Subsequently, the strategy is assessed using the simulation framework of the **chapter 4**, demonstrating the theoretical superiority of our local approach. We then propose various strategies for selecting solutions or producing a set of eligible solutions to the clinician, involving its expertise in the decision process. From these results we analyze the reliability of the solutions with respect to their distance to the sensors, thus extracting statistics (in terms of true

and false positives) allowing to delimit zones of confidence, giving to the clinician quantitative facts on the reliability of a found source localization. Our local approach is then applied and evaluated on real data corresponding to intracerebral stimulations (ICS) and to recordings of epileptic spikes such as carried out in the **chapter 3**. sensor

Chapter 1

Electrophysiology of the human brain

This first chapter is an introduction to background information on the organization of the brain and on the generation of electromagnetic brain activity. Section 1.1 provides a short description of the brain structure, and particularly of the cortical and sub-cortical layers, which are the seat of brain activity. An overview of the principal brain functions is given before the elementary constitutive cell of the brain, the neuron, is described. We then explain in Section 1.2 how sets of inter-connected neuronal populations give birth to the electromagnetic field, and we shortly describe the normal as well as the pathological electrophysiology of the brain. Specifically, we give an overview of epilepsy and of its electrophysiological characterization. Finally, Section 1.3 presents the main neuro-imaging tool currently used to explore the brain. After imaging anatomo-functional modalities are shortly described, we introduce the reader to magnetoencephalography, before deepening the electroencephalographic acquisition setup, and in particular the invasive stereo-electroencephalographic (SEEG) measurements explored in this thesis for electrical brain source localization.

1.1 A short introduction to the brain

The brain can be divided in three parts: the cerebrum, the cerebellum and the brainstem (see Figure 1.1). The cerebellum, located underneath the cerebrum, plays an important role in motor control (body balance, muscle movements, *etc.*). The brainstem acts as a relay with the spinal cord and maintains vital body functions such as breathing and heart rate control. The cerebrum is the largest part of the brain. It is composed of two approximately symmetrical hemispheres, responsible for high level perceptive and cognitive functions. The outer part of the cerebrum is called the cerebral cortex, 2 to 4 mm thick and folded to reach a higher surface area within the limited space offered by the skull. Four main parts are generally considered: the frontal, the parietal, the temporal, and the occipital lobe. The cortex is organized in layers, and several subcortical structures such as the hippocampus, the thalamus, the olfactory bulb or the amygdala can also be distinguished. These sub-structures are involved in the processing of very specific tasks, often handled collaboratively, and their roles can be different from one hemisphere to the other.

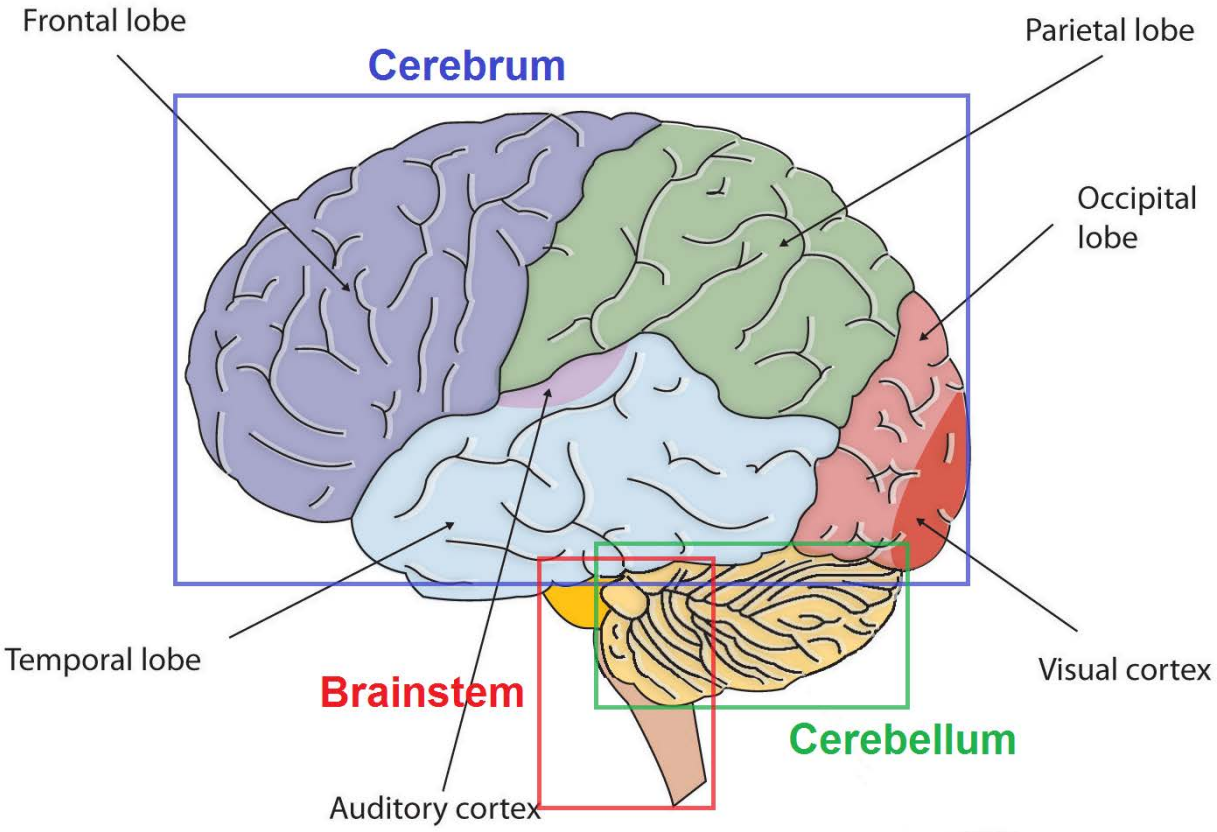

Figure 1.1: Main parts of the human brain – cerebellum, brainstem and cerebrum. Cerebrum divided in four lobes (frontal, pariental, occipital and temporal) [Eysenck 1958].

1.1.1 The cerebral cortex

The organization of the cerebral cortex in six layers has been established by Korbinian Brodmann in 1909 [Sholl 1956]. The five upper layers are mainly constituted of neurons (grey matter), whereas the sixth most profound layer

consists of nerve fibers which establish the connections between distant areas (the white matter). Each of the five upper cortical layers embeds their own neuronal organization. In particular, the superficial layers mainly consists of glial cells, extensions of apical dendrites of pyramidal neurons and horizontally oriented axons. The simultaneous excitations of these pyramidal neurons are at the root of the observable electromagnetic activity.

Interconnections span the whole cortex thickness, yielding connections locally among the layers, forming cortical microcircuits called cortical columns and minicolumns. It has been established that the functional activity of the brain is homogeneous within columns, while abrupt changes are observed in population of close columns [Mountcastle 1997]. However, the functional organization of the brain is to be observed at a wider scale. Indeed, connections between distant cortical and sub-cortical regions are established through the white matter. For example, most sensory information is routed to the cerebral cortex via the thalamus. Olfactory information passes through the olfactory bulb to the olfactory cortex (piriform cortex). In the next section we give a quick overview on the functional organization of the brain.

1.1.2 Functions

Cortical areas related to three sub-groups of functions can be distinguished: sensory, motor, and association areas.

- The sensory areas are the areas receiving sensory input from the thalamus. We can cite the primary visual cortex, the primary auditory cortex and the primary somatosensory cortex, which are responsible, respectively, for the vision, the audition and the touch. It is well established that the right hemisphere handles the sensory stimuli of the left side of the body, and inversely the left hemisphere receives the sensory information from the right side of the body. There is a high topographic coherence between these areas and their corresponding sensing organs, which gave birth to the somatosensory homunculus of Penfield [Penfield and Boldrey 1937], mapping the different parts of the body with their corresponding sensitive (and motor) cortical areas (see Figure 1.2).

- The motor areas are responsible for the planning, the control and the execution of voluntary movements. These areas are located across both hemispheres within the frontal lobe. The main structures are the primary motor cortex, the premotor cortex, the supplementary motor area, as well as the basal ganglia.

- The association areas are related to our perception of the world, to movement planning, to our ability of memorization, abstract thinking, and language learning. Three main areas can be distinguished: the prefrontal, the inferior temporal, and the parietal-temporal-temporal-occipital areas. Various distributed networks over these areas are each handling a specific association function. We can cite in particular the broca's area, a region in the frontal lobe of the dominant hemisphere (usually the left one) which is responsible for speech production.

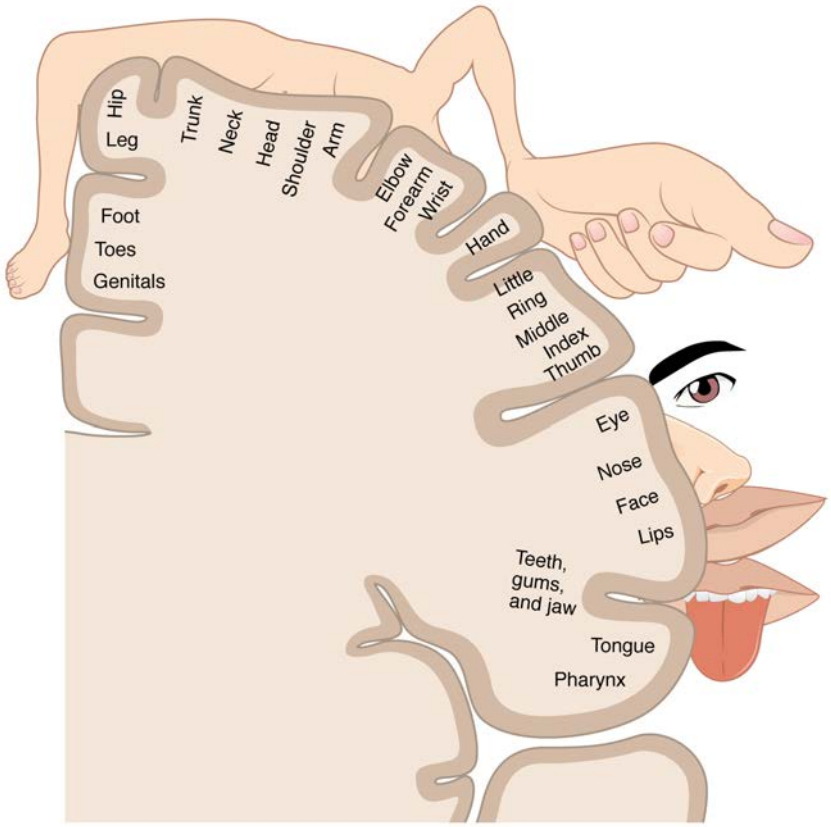

Figure 1.2: Graphical illustration of the Penfield Homunculus [Betts 2013].

1.1.3 The neuron

The neuron is the elementary unit for information processing in the cortex. It can be separated in three main parts (see Figure 1.3): **the dendrites**, which receive stimuli from thousands of other afferent cells, **the soma** or cell body, which contains the nucleus, and **the axon**, which transmits information to different connected neurons. The connection points handling the transmission between the axon of an afferent neuron and the dendrites of the receiving neuron are called synapses.

One can distinguish different types of neurons from the shape of their cell body (star-shaped, fusiform, conical, polyhedral, spherical, pyramidal). These shapes, as well as the number and size of dendrites, are related to the specific function of the neurons. In this thesis we will focus on the activity of the pyramidal neurons, which can be found in the cerebral cortex, the hippocampus, and the amygdala, and are at the origin of most of the measured electromagnetic activity (see Subsection 1.2.1). They are named after the triangular shape of their soma (see Figure 1.4a), and are organized in palisades within the neo-cortex, *i.e.*, parallel alignment, one relative to the other and perpendicular to the plane of the layers. In the prefrontal cortex, they are implicated in cognitive ability, and particularly in the recognition of complex objects within the visual processing areas of the cortex.

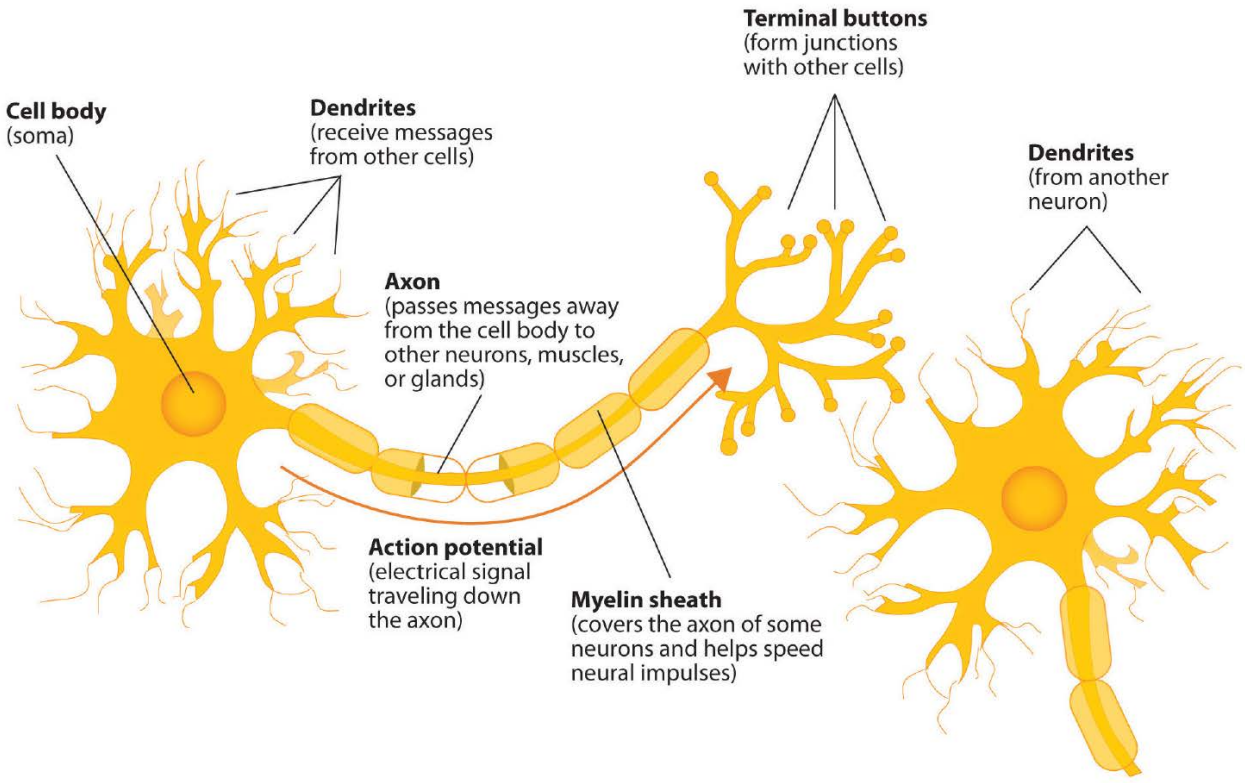

Figure 1.3: Main parts of a neuron [Eysenck 1958].

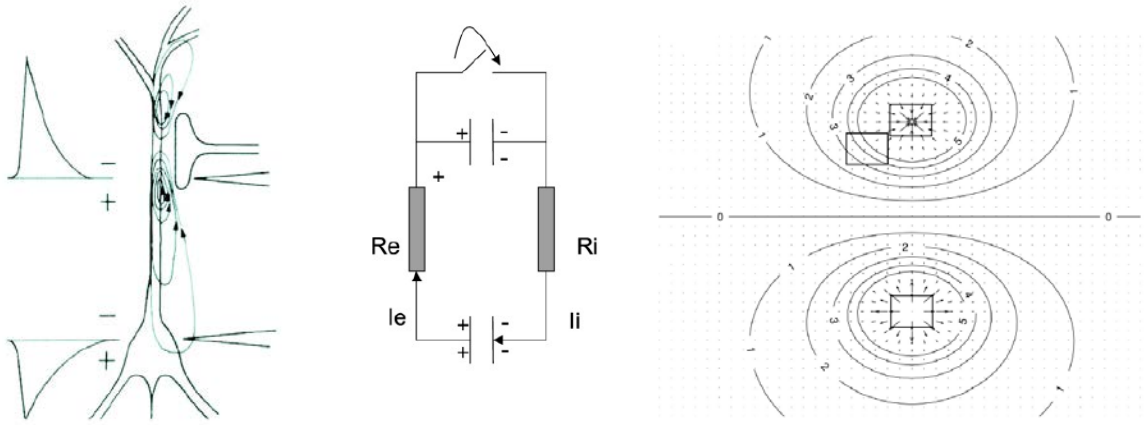

(a) **(b)** **(c)**

Figure 1.4: Illustration of electromagnetic field generated by pyramidal neuron. (a) – A neuron with an excitatory synapse at the apical dendrite. (b) – A simplified equivalent circuit. (c) – The current density and equipotential lines in the vicinity of a dipole.[Hallez et al. 2007]

1.2 Brain electrophysiology

1.2.1 Electromagnetic brain signal generation

In this thesis we will analyze the electric field generated by the brain recorded using an electroencephalographic setup. This electrical activity originates in the synchronous activation of a large number of contiguous pyramidal cells. Their organization in palisades at the surface of the cortex implies that their synchronized activities are summed, thus generating a visible electromagnetic field on the macroscopic electrodes.

At the level of the cell, the electromagnetic field is due to the emission of action potential by the neurons. These neuronal firing activities are induced by the exchange of ion through the voltage-gated ion channels embedded in the cells. If the potential of the cell membranes reaches a given threshold (due to the inflow of excitatory pre-synaptic activities into the cell), the gates open and allow an influx of sodium ions, which provokes the generation of an action potential, yielding an additional rise of the membrane potentials of the neighboring cells. By an ensemble effect, a higher number of ion channels are then opened, giving birth to action potentials over a possibly wide neuronal population.

These post-synaptic action potentials form a current sink in the vicinity of the synapse, whereas the axonal end of the post-synaptic neuron becomes more positive, forming a current source (in Figure 1.4c). The conjunction of these two phenomena forms a current dipole oriented along the dendrite of the cell, justifying the dipolar source model that will be used in this thesis. The addition of several small dipolar activities within a large neuronal population are modeled as an equivalent current dipole summing up the synchronized activity of the population. The electric signal has to propagate through several layers (scalp skull, brain tissue, *etc*.) before reaching the scalp surface. The skull represents the most severe barrier, attenuating the signal about a hundred times more than other tissues. In the context of epilepsy, it is reported that an activated cortex surface of the order of $10cm^2$ is needed to produce a visible electric field on the head surface using scalp electrodes [Kobayashi et al. 2005, Tao et al. 2005]. When considering intracerebral electrodes, the skull barrier is avoided, and a surface of a few millimeter square can be sufficient to produce a visible electric field, depending on the distance to the closest intracerebral contact.

1.2.2 Normal electrophysiology

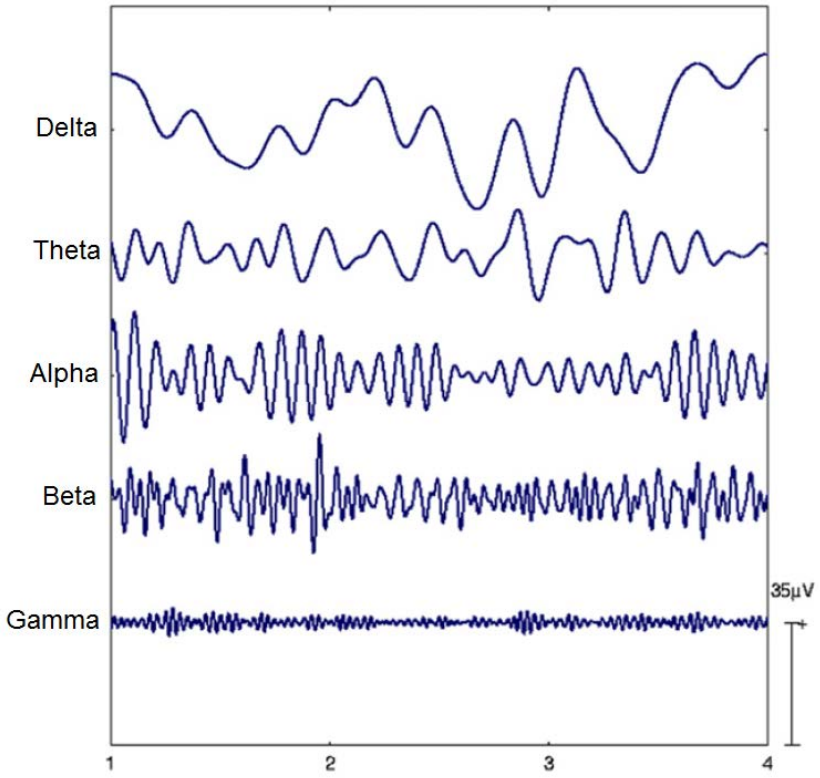

Figure 1.5: Five normal brain rhythms, from low to high frequencies. Delta, theta, alpha, beta and gamma rhythms comprise the background EEG spectrum [Urigüen and Garcia-Zapirain 2015].

The neural electric activity of the human brain spans a large range of rhythms, mostly below $100Hz$ and sometimes higher for specific activities. Their amplitude and frequencies are descriptors of the states the brain can take, such as wakefulness, sleep, resting state or processing state (*e.g.*, of cognitive or motor tasks). These characteristics can vary from one human to another, but some general families of brain rhythms can still be distinguished in the electrophysiology of healthy adults. In 1974, the *International Federation of Societies for Electroencephalography and Clinical Neurophysiology* established a classification of the brain rhythms in 5 main ranges: delta (δ), theta (θ), alpha (α), beta (β) and gamma (γ) rhythms from lowest to highest frequency rates (seen in Figure 1.5 and 1.6).

- δ (0,5-4 Hz): these low frequency range activities are generally associated to deep sleep states in the adult brain. It constitutes the principal rhythm for children under the age of one. Scalp recordings are often highly impacted by low frequency muscle activities lying near the head surface (mostly of the neck and jaw), whereas the deep signal of interest is seen with lower amplitude due to the propagation attenuation. Intra-cranial recordings are less prone to such signal to noise ratio issues, the electrodes being implanted near the electric generators.

- θ (4-8 Hz): are observed within the neo-cortex in a wide range of brain states: sleep states, within periods of unconsciousness and deep meditation, but are also associated to a state of arousal. Still in the neo-cortex, these frequency ranges are predominant in the brains of children, and tend to be less present in an adult brain, for which an abundant presence of such activities is associated with abnormality (mental disorder, a state of depression, *etc...*) [Vespignani 2003]. It has to be noted that the presence of such rhythms in the hippocampus bears other meanings related to memorization tasks.

- α (8-13 Hz): are often encountered in the human brain as round-shaped oscillations of high amplitudes. This oscillatory α pattern is observed when eyes are closed (occipital alpha waves) or during a relaxed mental state, but tend to disappear with the eyes open or with mental concentration. The origin and functional role of such waves are still open questions, but are widely used for neurofeedback training, enabling individuals to regulate their brain activity and to increase or decrease the production of their α waves depending on the objective of the treatment [Tesche and Karhu 2000].

- β (13-30 Hz): is the normally observed activity of the brain in an awake state, associated with active thinking, attention, concrete problem solving. They are suppressed prior to and during movement changes.

- γ (>30 Hz): are supposed to be observed during higher processing tasks and cognitive functioning [Varela et al. 2001]. In particular, they have been proven to play a major role in the process of learning. Its low amplitude makes them difficult to be observed on the scalp surface, but they can be observed using intracranial EEG measurements.

In addition, higher frequency normal brain rhythms have been recorded beyond the γ band using intracerebral recordings, but their function in human cognitive processing has not been fully elucidated yet. However, it has been demonstrated that such fast ripple activities (up to $500Hz$) are implicated in memory coding and recall [Kucewicz et al. 2014].

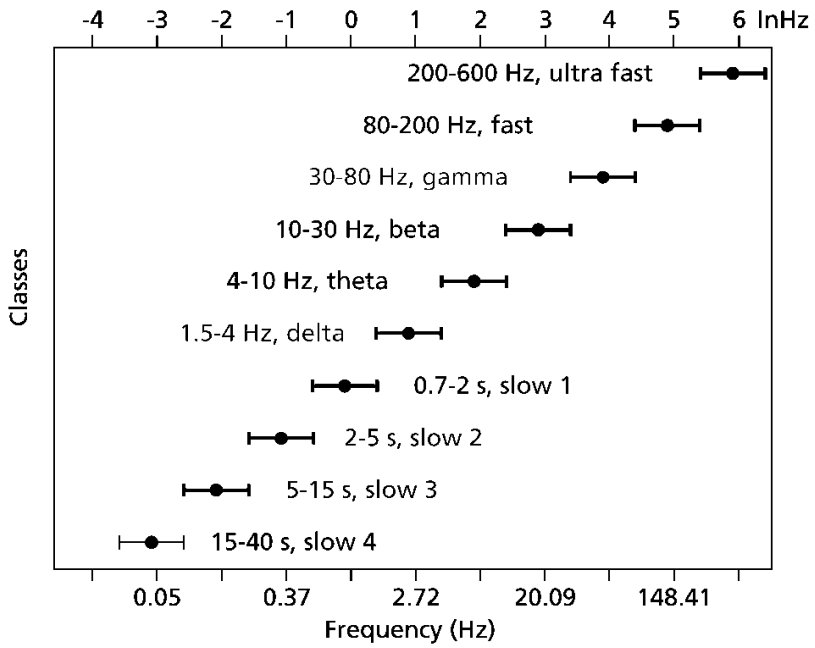

Figure 1.6: A system of interacting brain oscillations. Oscillatory classes in the cortex. Note the linear progression of the frequency classes (written next to the commonly used name for each rhythm), on the natural log scale. This geometrical order is despite the fact that these frequency families were defined based on phenomenological correlates [Buzsáki and Watson 2012].

1.2.3 Pathological electrophysiology

In presence of a pathology, the brain activity either elicits abnormal patterns, or tends to suppress and distort normal patterns. A tremendous number of such abnormalities can be cited, Sharbrough [Sharbrough 2005] proposed to divide them in three descriptive categories based on their localization (lateral, bilateral or widespread) and their temporal length (transient to persistent waves): (i) widespread slow wave abnormalities related to brain dysfunction, often within the δ range, (ii) bilateral persistent EEG associated with impaired conscious cerebral responsivity, and (iii) focal persistent EEG activities, associated with focal cerebral disturbance. In the following, we will focus on the characteristics of these abnormalities in the case of two well known pathologies: dementia and epilepsy, with more insights on this last class of pathology for which real cases will be treated in this thesis.

1.2.3.1 Dementia

Dementia is a general class of pathologies which translates to a loss of cognitive and intellectual abilities. The most common form of this kind of disease is Alzheimer, which is a chronic degenerative disease of cortical cells leading to short-term memory loss in its first stage, further worsening in behavioral issues. We can also cite Creutzfeld-Jacob, which is also a cortical disease, and Parkinson, which is a sub-cortical disease mainly affecting the basal ganglia and provoking progressive disorders of the motor system. Clinicians have more and more often resorted to electrophysiological recordings to improve their diagnosis of Dementia. From scalp recordings, particular EEG patterns of cortical degenerative diseases are visible. Alzheimer disease translates to a slow down of the α rhythms along with an increase of the θ and δ waves. Creutzfeld-Jacob disease causes slowing down of the θ and δ wave activities, and periodic sharp waves appear almost every second about 3 months after the beginning of the disease. In the case of Parkinson, which is a sub-cortical disease, the diagnosis is more complex from surfacic recordings, the signal being

generated in deep structures of the brain. However, from a spectral analysis it is possible to extract specific patterns of this illness, which consist of an increase of the δ and θ waves activities [Neufeld et al. 1994].

Often the observation of the EEG signal alone is not sufficient to distinguish between diseases with overlapping electrophysiological symptoms. In this case, brain source localization can bring decisive information on the location of the generators of the abnormal pattern, helping to differentiate the disease from *prior* clinician knowledge on the affected structures. For example, an EEG-based localization procedure was shown to be helpful in differentiating between mild cognitive impairment (a transitional state toward Alzheimer) and Alzheimer's disease [Babiloni et al. 2009].

1.2.3.2 Epilepsy

EEG recordings have been extensively used for the detection and the prediction of epileptic events. This pathology induces important changes in the frequency characteristics of the patient electrophysiology, which goes from chaotic signatures to a prominent sinusoidal form during the paroxistic period of the crisis. Two main classes of epilepsy can be identified: generalized and partial epilepsies. Generalized epilepsy is a type of seizure that impairs consciousness and affects the electrical activity of a large portion of the brain, often over both hemispheres. The most known form of this type of epilepsy is the tonic-clonic epilepsy (formerly known as grand mal seizures), sometimes leading to violent shaking or vibrating uncontrolled movements of the epileptic subject. Inversely, partial epilepsy is confined to a limited number (or to a single) of cortical brain structures, sometimes spreading to other parts of the brain along the evolution of the crisis.

Independently of the nature of the seizure, the electrocardiography patterns are easily recognizable in comparison with other common artifacts. These activities are characterized by sudden abnormal electric discharges, called paroxysmal discharges, going from spiky forms to very repetitive sinusoidal discharges depending on the period of the crisis. As far as partial epilepsy is concerned, a classic scenario of a crisis can be described as follows: in between two crises the patient is in the interictal states, characterized by the sporadic apparition of interictal spikes, which are spiky waveforms recognizable by inspection of the EEG recordings by trained eyes. During the onset of the crisis, a bursting of spikes is commonly observed during a few seconds, corresponding to the sudden discharge of a focal area (such as the temporal pole in the case of partial temporal epilepsy), before the activity slows down and becomes nearly silent for a long moment (up to 30 seconds). Finally the crisis derives to the paroxistic events eliciting sinusoidal waveforms of high amplitudes, usually spread over the θ, α and β ranges depending on the patient and on the instant of the paroxistic burst.

The mechanism behind focal epilepsy is now widely believed to be driven by a network of abnormally hyperconnected structures, due to a wrong balance between inhibitory and excitatory inter-neurons within the involved structures [Bromfield et al. 2006]. In the case of the temporal lobe epilepsy, several distinct cortical and sub-cortical structures are recruited in the epileptic process during the seizure [Maillard et al. 2004]. This network reconfigures itself all along the crisis. The identification of its dynamic might yield precious information on the initiating and leading structures, and opening doors for a better understanding of this pathology leading to more accurate and efficient treatment [Achard et al. 2006, Wendling et al. 2010]. The relations between the structures can be deduced from the EEG recordings by computing statistical relationships between the dynamic activity recorded from distinct

brain areas [Achard et al. 2006, Bullmore and Sporns 2009, Wendling et al. 2010]. If such analysis can be done from the raw EEG, the volume conduction problem arises and makes such analysis highly unreliable. Epileptic source localization and reconstruction of their time-courses is thus a key to the subsequent analysis of the epileptic event.

1.3 Investigation modalities

Different modalities have been used to explore the most complicated human organ – the brain. These modalities differ in cost, invasiveness, as well as temporal and spatial resolution. A quick overview is given in Figure 1.7, demonstrating the time and spatial resolutions these modalities are giving access to. In this study we are particularly exploring the possibilities of SEEG due to its good temporal and spatial resolution, as well as its high signal to noise ratio (SNR) due to the proximity of the invasive electrode contacts with the sources of interest.

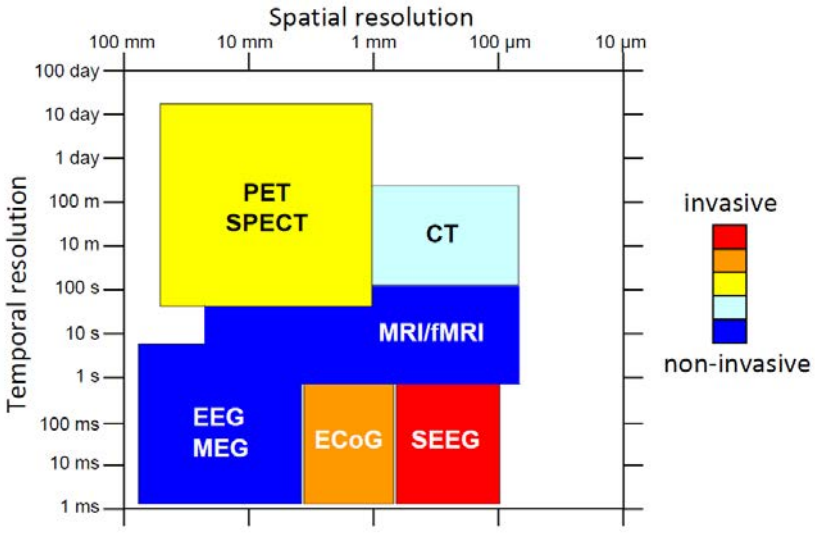

Figure 1.7: Spatial and temporal resolutions of the different brain imaging techniques (PET: Positron Emission Tomography, SPECT: Single-Photon Emission Computed Tomography, CT-scan: Computed Tomography scan, MRI: Magnetic Resonance Imaging, fMRI: functional MRI, EEG: ElectroEncephaloGraphy, MEG: MagnetoEncephaloGraphy, ECoG: ElectroCorticoGraphy, SEEG: Stereo-EEG) [Ansari-Asl 2005, Hofmanis 2013].

1.3.1 Anatomical and functional data

The anatomical data provides an insight on the possible lesions and malformations in the brain structures, which can explain the presence and identify the seat of a given pathology (abnormalities or tumors). This data is recorded by several brain imaging modalities such as radiological images, scanners or Magnetic Resonance Imaging (MRI). As a result of achievements made in the field of brain imaging in recent years, it is now possible to indirectly record the activity of certain parts of the brain via functional MRI (fMRI). In the context of brain source localization, these modalities can be used as *priors* for driving the localization process within the most likely area pointed by them. They are also important for the construction of the forward model (see Section 2.2), as they enable the segmentation of the different tissues within the head and give access to an automatic identification of the recording contact positions in the case of intracerebral setup [Hofmanis et al. 2011].

1.3.1.1 Computed Tomography (CT) scan

Computed tomography (CT) is based on the principle of the acquisition of incremental X-ray scan images from different angles to produce cross-sectional (tomographic) images (virtual "slices") of specific areas of the brain (see Figure 1.8a). The distance between two acquired sections is accurate if the object of interest is still, but remains a problem in the case of brain acquisition which can be strongly affected by patient motion. Since the rise and enhancement of Magnetic Resonance Imaging (MRI), there has been less interest on this modality, as its sensitivity to detect fine lesions associated with epilepsy is relatively low (accuracy of about 20% is reported in the case of temporal lobe epilepsy [Swartz et al. 1992]) and is strongly linked to the type of epilepsy, to the age of the disease and to the associated neurological signs.

Nevertheless, there are circumstances when the CT is still useful. Mainly, on newly diagnosed patients, CT examination can produce an initial evaluation of the pathology due to its fast computation. In addition, CT is the only available anatomic imaging modality when the patient has a contraindication to MRI.

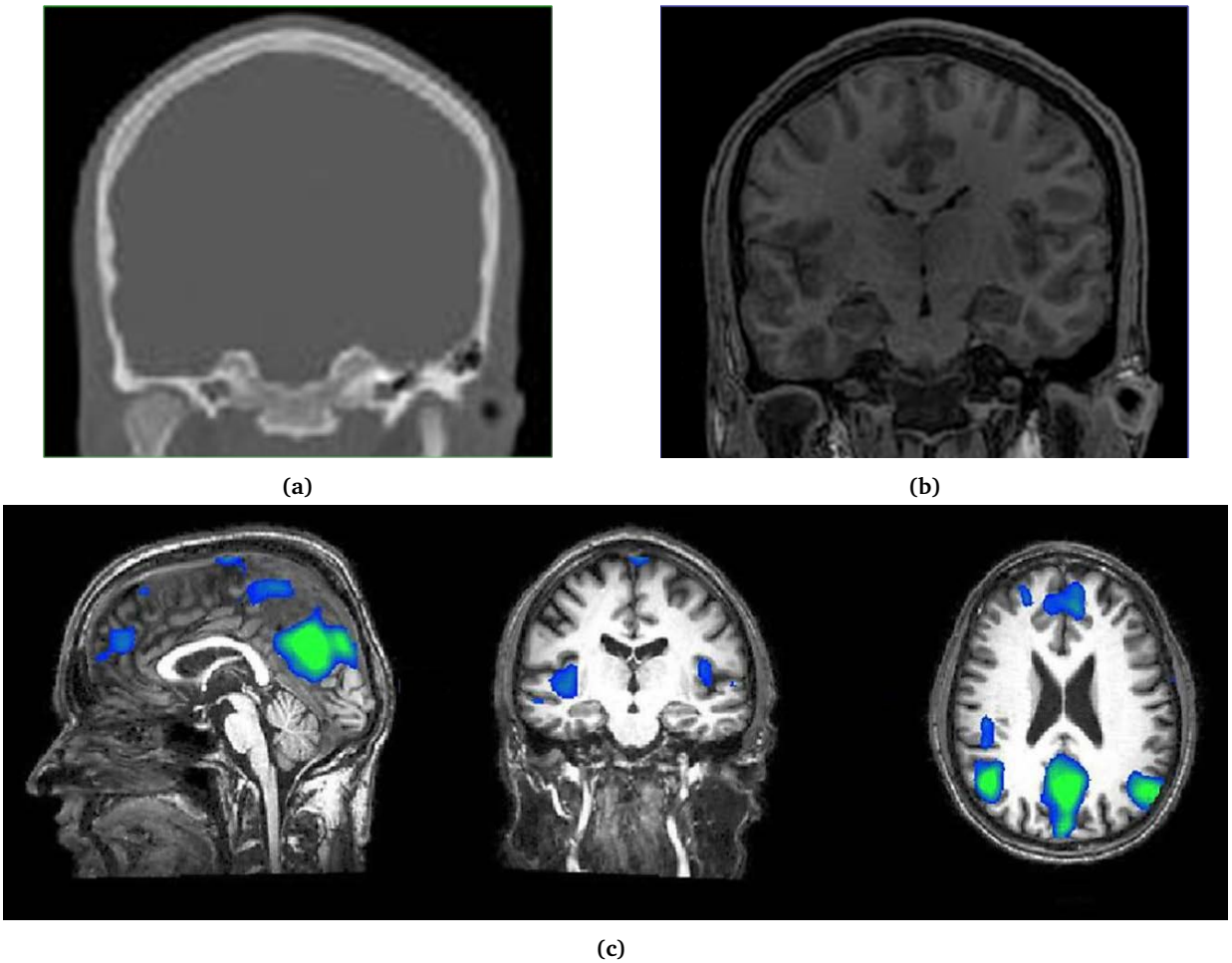

(a) **(b)**

(c)

Figure 1.8: Data acquisition results for investigation modalities yielding results in the form of images – CT (a), MRI (b) and fMRI (c)

1.3.1.2 Magnetic Resonance Imaging (MRI)

MRI, based on the science of Nuclear Magnetic Resonance, produces images of the anatomy and the physiological processes taking place in the brain structures. Placed under a strong magnetic field, the hydrogen atoms of the brain

can absorb and emit radio-frequency, and MRI can map these atoms in the brain volume to reconstruct an image (see Figure 1.8b). The response of the atoms varies with the tissues, enabling the identification of the grey and white matter. MRI produces higher resolution images than a CT scan and is useful for the identification of brain lesions. As an example, it can reach an accuracy of 80% in the detection of lesions of temporal lobe epilepsy [Swartz et al. 1992].

1.3.1.3 Functional MRI (fMRI)

Functional MRI can tract the flux of hydrogen atoms circulating in the blood vessels of the brain (hemodynamic response), thus bringing an indirect view of the functional processes (activation of neuronal populations) happening within the cortex and the sub-cortical structures by capturing the Blood Oxygenation Level Dependent (BOLD) signal (see Figure 1.8c). The changes in these activations can be observed with a time resolution of about one second. These modalities are more and more involved in clinical evaluation, generally carried out for refractory brain epilepsy to bring further decision on the treatment to be adopted. It is indeed possible to relate the BOLD signal with the activation of neuronal populations at the origin of epileptic spikes [Kobayashi et al. 2006]. This modality has motivated a wide range of neuroimaging research. In particular, it is often used jointly with the EEG to study the dynamic of the epileptic network, using classical statistical tools to identify causality in time-series [Friston et al. 1995, Gotman 2008, Vulliemoz et al. 2009].

1.3.2 Magnetoencephalography (MEG)

The Magnetoencephalography (MEG) is a relatively recent recording setup discovered by David Cohen in 1963 [Cohen et al. 1968]. Its principle is based on the law of Bio-Savart, stating that each elementary stream from the activity of nerve cells produces a perpendicular magnetic field. It is therefore possible to measure, on the scalp surface, the global magnetic field variations, which is the sum of the fields generated by all the currents. MEG thus essentially records the contribution of intra- and extracellular currents due to post-synaptic potentials (seen in Figure 1.9a).

The main advantage of this technique over the surface EEG is that the collected signals are significantly less deformed by the successive layers through which the signal propagates. Other advantages of the MEG are that they can be calculated without reference, or that they produce a better localization of the epileptic focus when compared to EEG [Barkley and Baumgartner 2003]. This technique is however not widespread yet due to its prohibitive cost. Thus, it does not replace EEG technology but is rather used as a complementary diagnostic tool in difficult cases.

1.3.3 Electroencephalography (EEG)

The electric activity of the brain can be recorded using Electroencephalography (EEG), consisting of a multi-channel recording setup using scalp sensors, usually placed at specific positions (see Figure 1.10 for an example). It measures the difference of the electric potential between each sensor and a reference electrode, or with an artificial reference obtained by subtracting the time signal averaged over all sensors from the data of each channel (common reference montage). Like the MEG and contrary to CT or (f)MRI, the EEG provides a direct recording of the neuronal activity (though at a macroscopic scale) with a time resolution of about a millisecond. This temporal scale is in a comparable order of magnitude with the dynamic of the neuronal processes (cognitive or pathological), making the EEG the most popular modality for investigating the brain.

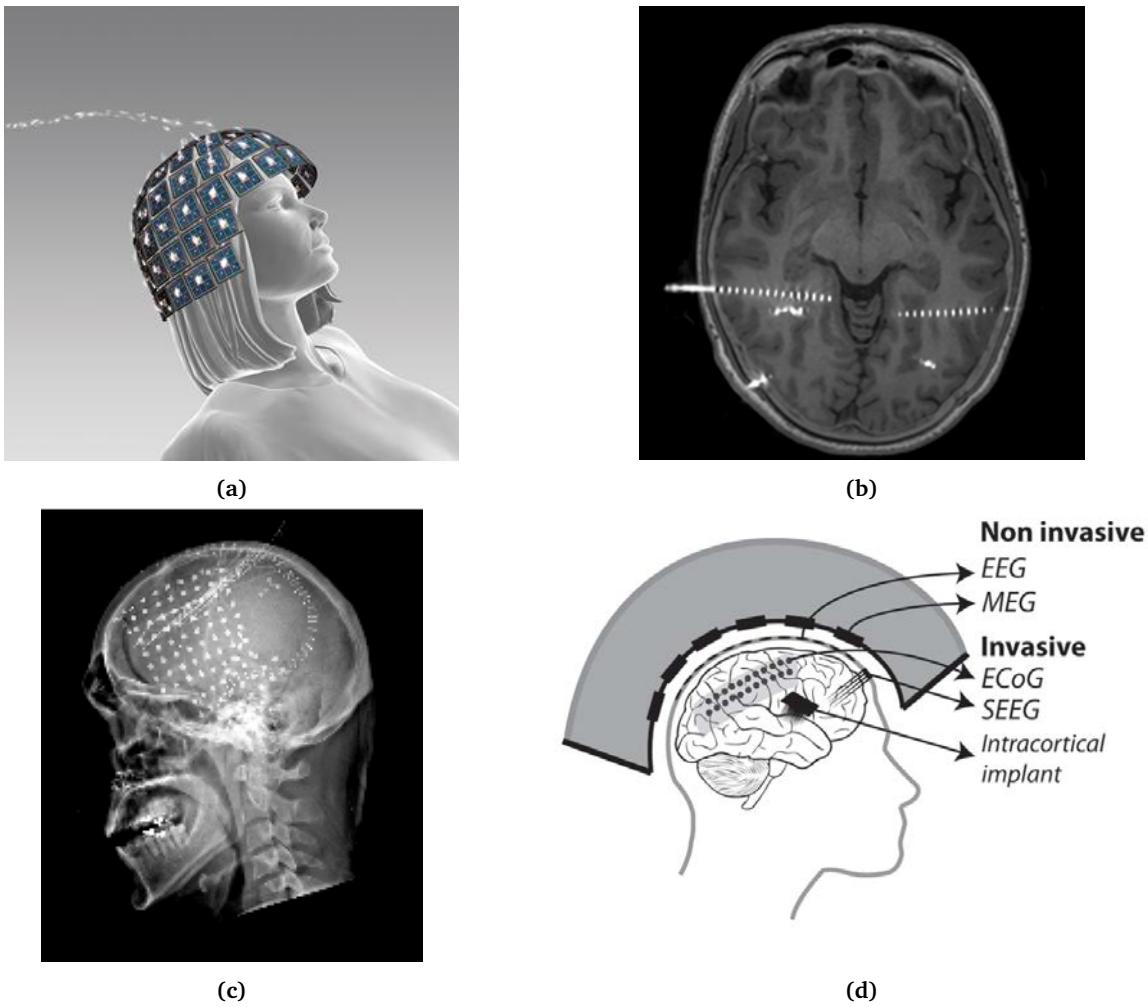

Figure 1.9: Illustrative examples for different sensors – MEG (a), SEEG (b), ECoG (c) and overall illustration for different techniques (d) [Astrand et al. 2014]

EEG commonly refers to a surface measurements setup, where the electrodes are placed on the scalp of the patient. Its ease of installation, portability and relative low cost makes this recording setup even more convenient. In particular, it has been extensively used to solve the brain source localization problem. In this thesis, however, we will rather focus on an invasive EEG recording setup: the Stereo-electroencephalography (SEEG), consisting of needle electrodes of aligned contacts directly implanted in the brain volume. In addition, to complete the picture of the invasive EEG modalities, we can also cite the Electrocorticography (ECoG) developed by Wilder Penfield and Herbert Jasper in the 50s [Palmini 2006], which consists of (grid of) electrodes directly placed on the surface of the cortex, usually organized in patches (as shown in Figure 1.9c). While some investigation has already been carried out to localize brain sources from ECoG, there are very few studies on this topic on the SEEG side, apart of the work done in our research team.

1.3.3.1 Scalp EEG

Huge progress has been made since the first EEG recordings by Hans Berger in 1920. Recent setups are able to record up to 256 channels, thus covering the head surface with high spatial resolution (EEG-HR). The frequency sampling rate can reach several kilo Hertz, providing high temporal resolution data for investigating the brain mechanisms.

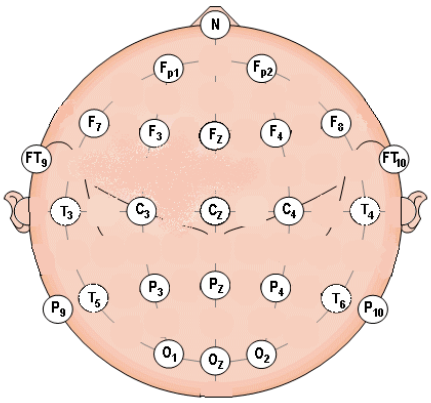

Figure 1.10: Schematic example of surface EEG electrode placement (current montage at the Nancy CHRU).

Apart from such an advanced setup dedicated to research, standard medical scalp EEG systems involve between 19 and 32 electrodes. The electrodes are positioned on the scalp according to standardized placement systems predefined by the International Federation of Societies for Electroencephalography and Clinical Neurophysiology. The conventional electrode setting (the 10-20 system) includes 21 electrodes, separated by distances based on specific anatomic landmarks. These landmarks define the area within which the electrical activity should be recorded, and using 10 or 20% of the distance between these landmarks provide the electrode intervals. When the number of sensors is increased, extensions of this system (*e.g.*, 10-10 and 10-5 systems) are adopted [Chatrian et al. 1985, Oostenveld and Praamstra 2001]. Variants of these standard systems exist also (see Figure 1.10 for an example of EEG montage used at the Nancy hospital).

It is worth noting that beyond the use of EEG for medical and research application, the entertainment industry has begun developing EEG systems at destination of the general public, with applications in augmented reality, video games and for the so-called "Internet of Things" [Debener et al. 2012, Renard et al. 2010, Swan 2012].

1.3.3.2 Stereo EEG (SEEG)

Stereoelectroencephalography (SEEG) was developed in France by Bancaud and Talairach in the late 50s [Talairach et al. 1958]. It consists of electrode shafts directly implanted within the brain volume, thus requiring surgical intervention (see Figure 1.9b). During this operation the head is maintained by a stereo-taxic frame to prevent any head movements, explaining the name of Stereo-EEG. About fifteen to twenty electrode shafts are usually implanted, each containing up to twenty recording contacts.

The main asset of SEEG when compared to scalp EEG is to record the electrical activity of neurons in the direct vicinity of the generators. Very punctual signals of weak amplitude can then be collected, and the seat of pathologies or cognitive functions are reachable with a high signal to noise ratio. In addition, SEEG recordings have the advantage of being far less affected than the surface measurements by artifact muscular activities.

Intracerebral explorations are usually carried out for presurgical evaluations in case of drug-resistant partial epilepsy. Only the patients whose anatomical (MRI) and EEG analysis did not result in a precise location of the epileptogenic zone are undergoing exploration in SEEG. Indeed, even if this method of exploration is currently well controlled by neurosurgeons, risks of morbidity remain. In addition, to maximize the effectiveness of SEEG, strong

hypotheses on the area suspected to hold the epileptogenic zone are needed. These hypotheses are usually obtained from the surface measurements (first electrodes involved in the crisis, rapid spread of the signal, ...), MRI, as well as the semiological evolution of the ictal event.

As the number of implanted contacts is limited by the obvious reason of limiting medical risk, all regions of the brain cannot be covered (at least when signals are observed on a bipolar montage). The clinicians target a region of interest where most of the electrodes are implanted, as they are trying to circumscribe the region thought to be responsible for the epileptic events. A dozen electrodes are implanted within the hemisphere of the suspicious region (the ipsi hemisphere), whereas only about three electrodes are implanted within the opposite (contra) hemisphere.

In clinical context, the measurements is usually observed on a bipolar montage, *i.e.*, the difference 2 by 2 between neighboring contacts is computed, providing a local vision of the brain activity surrounding each pair of successive electrode contacts. The location of the generators of interest can then be directly assessed by visual interpretation of the signal, confirming or infirming the clinical hypothesis before proceeding to the surgical operation. This focal visibility of the setup also represents a drawback. A mis-implantation of the electrodes in the brain volume might make the targeted activity invisible with respect to the recording setup, as its projections on each contact are likely to be hidden by the surrounding activities close to the contacts. This is particularly the case when the bipolar montage is used.

1.4 Problematic and progression of the thesis

In the literature, the wide majority of the studies are solving the brain source imaging problem from the EEG/MEG measurements, with the aim of mapping the electromagnetic brain activity based on non invasive tools. Up to now, the SEEG has been limited to a role of validation, by assessing the performance of the localization methods based on non-invasive measurements [Bénar et al. 2006, Koessler et al. 2010a]. In particular, such localization is of great interest in epilepsy and is currently used in clinical routines (on bipolar montage) for confirming the clinician's hypothesis on the location of the irritative zone before the patient is implanted with SEEG. In this context, the objective is, ultimately, to obtain a method reliable enough to reduce the need of the SEEG step and to directly proceed to the resection of the brain region responsible for the pathology.

The aim of this thesis is to reconsider the use of the SEEG from its current status of control tool toward a reliable modality for solving the brain source inverse problem. Exploited in common reference (*i.e.*, using a reference electrode placed on the head surface of the patient), it is indeed possible to collect the propagation of brain sources distant from the electrode contacts. The goal is to establish this modality as a complement to routine visual interpretations, by identifying the localization of sources that are invisible when the signals are observed on bipolar montage. Due to the high quality signal this modality provides, it is also a promising tool for reconstructing, with high precision, the locations and time-courses of the sources, thus providing precise information for studying the inner mechanism of a given pathology (focal epilepsy in the first place) or of cognitive functions such as visual or auditory processing networks of the brain.

As far as brain source localization from invasive measurement is concerned, very few up to date studies can be found in the literature. We can cite few works based on ECoG [Cho et al. 2011, Dümpelmann et al. 2009, Dümpelmann et al. 2012, Gharib et al. 1995, Ramantani et al. 2013, Zhang et al. 2008], and also a couple of studies using SEEG measurements [Chang et al. 2005, von Ellenrieder et al. 2012a], exclusively carried out in simulated

environments. Beyond the inherent advantages of the SEEG setup (proximity with the sources, high signal to noise ratio when compared with surface EEG), brain source localization from this invasive modality involves several drawbacks. The main one is related to the implantation of the SEEG shaft electrodes, implanted in clusters in the region of interests, almost parallel one from the other, and not homogeneously covering the whole brain volume.

Several questions about the reliability of brain source imaging from the SEEG then arise, and are tackled in the **Chapter 3** of this thesis. In particular, we address the needed level of head modeling in the SEEG context. The opportunity of using analytical models with low computational cost is evaluated. Under a realistic SEEG setup, we analyze the required SEEG sensor subset (number of sensors, source to sensor distance) to reach reliable localization performance, in particular in context of noisy environment where the projection of simultaneously active dipoles are corrupting the recordings of the activity of interest.

Following this preliminary study identifying the good practices for reaching reliable localization results, we propose in **Chapter 4** a standardized local approach for SEEG brain source imaging. Indeed, one of the main conclusions of **Chapter 4** is that selecting a minimum number of spatially well conditioned electrode contacts leads to better localization accuracies in median. We thus propose an iterative approach accumulating the neighboring electrode contacts around an initial guess for the source position. This approach proves to enhance the reliability of the localization results within realistic configurations of noise levels and allow to define identifiable zones of the brain with respect to a specific electrode implantation. Localizations are studied in a simulation setup, stimulated signal case and on real epileptic spikes.

Chapter 2

Forward modeling and source localization

2.1 Introduction

This chapter will introduce the most common practices to solve the source localization problem. EEG source localization has been an active field of research since the 1950s and relies on several important steps, beginning with the modeling of the sources and the resolution of the forward problem, linking source activities to the potentials measured on the sensors. In this objective, the choice of a physical propagation model is decisive, greatly conditioning the success of the localization process. The first part of this chapter discusses different propagation models, analyzing their advantages and shortcomings.

Since we are dealing with spatially-dependent information, besides the geometry of the model (head, skull, brain more or less precise shapes), the precise acquisition of the sensors' spatial positions is also required. Different commercial solutions exist for scalp EEG sensor position determination. In our case, as we are dealing with depth SEEG recordings, the sensor positions are not directly accessible and they need to be determined from the imaging (CT-Scan) exams of the patient. We briefly review here the registration procedure developed previously by our team [Hofmanis et al. 2011].

Based on these modeling prerequisites, the resolution of the source localization inverse problem is described in Section 2.3. An overview of different approaches to solve this problem is given, as well as details on commonly used optimization algorithms. SEEG electrical potential measurements being the focus of this study, a part of this chapter is dedicated to a discussion on the specificity of this modality when it comes to brain source localization. The few advances in localization based on SEEG are analyzed in Subsection 2.3.3, and several open questions motivating this work are explicitly formulated. Since the aim of this study is to develop the method in clinical use afterwards, the tools should provide diagnostic information for clinicians: neurologists, neurosurgeons ... To use real patient EEG/SEEG data for localization, data pre-processing specific to EEG/SEEG must be carried out. This is explained in detail in Section 2.4, which describes the important pre-processing steps necessary when dealing with real recordings, including the re-referencing step, the denoising of the signal, as well as the selection of the epochs of interest and of their averaging.

2.2 Forward modeling

The brain is an extremely complex organ. The studies that contribute to its understanding can be based on very different fields according to the spatial scale considered: biology, chemistry, physics, electrical, applied mathematics,

signal processing ... As in many fields to reduce the number of parameters, the model design depends on the question asked. Indeed, the objective of the study, the type of measurement and the performance to be achieved are factors to be taken into account initially for the model. SEEG and EEG forward modeling consists in calculating the electrical potential observed on a given sensor when the configuration of the underlying electrical sources and the biophysical properties and geometry of the propagation environment are known. Efficiency and accuracy of the forward model and solvers based on partial differential equations (PDE), in particular, the Poisson equations, describing the electrical potential distribution depend also on the highly heterogeneous and anisotropic human head tissues. To reduce the complexity of hypotheses such as: homogeneity of structures, propagation isotropy, linear model by part can be bases for the definition of the model. SEEG measurements are cerebral potentials of means fields, which makes it possible to define the spatial scale of the study. The SEEG measurement represents the sum of electrical activities propagating from different cortical sources to the EEG electrodes through various brain tissues with different conductivities.

2.2.1 Linear Mixing Model

Consider N_s sources responsible for the electrical potential on N_c electrodes. The propagation of the source activities through the brain volume is commonly considered as linear and instantaneous, *i.e.*, the brain volume is supposed to be purely resistive for the frequency range of interest [Ranta et al. 2017].

The theoretical electrical potential measurements $\boldsymbol{\phi}_0 \in \mathbb{R}^{N_c \times N_t}$ can then be described as a linear system:

$$\boldsymbol{\phi}_0 = \mathbf{KJ} \tag{2.1}$$

where the Lead-field $\mathbf{K} \in \mathbb{R}^{N_c \times 3N_s}$ contains the information about the propagation medium and the relative positions of the dipoles and electrodes, while current density matrix $\mathbf{J} \in \mathbb{R}^{3N_s \times N_t}$ contains information about the momentum and amplitudes of the N_s dipole sources through N_t time points.

Lead-field matrix K. The Lead-field matrix $\mathbf{K}$ consists of $N_c \times N_s$ blocks $\mathbf{k}_{mn} \in \mathbb{R}^{1\times 3}$, each representing the n-th source gain on the m-th sensor on each Cartesian axis (x, y, z), with fixed source and sensor positions:

$$\mathbf{K} = \begin{bmatrix} \mathbf{k}_{11} & \cdots & \mathbf{k}_{1N_s} \\ \vdots & \ddots & \vdots \\ \mathbf{k}_{N_c 1} & \cdots & \mathbf{k}_{N_c N_s} \end{bmatrix}$$

Several levels of modeling precision can be derived, depending on the application. The most popular methods for the construction of $\mathbf{K}$ will be described in Subsection 2.2.2).

Current density matrix J. We use the widely accepted dipolar model for the source, as explained in Subsection 1.2.1. A dipole is characterized by 6 parameters (3 for position and 3 for the elementary moment components) as illustrated in Figure 2.1. The vector projections of the dipole to Cartesian axis (x, y, z), representing the source orientation and amplitude, are encoded in the dipole current density matrix $\mathbf{J}$, composed of columns corresponding to each time instant $i \in 1...N_t$:

$$\mathbf{J} = \begin{bmatrix} \mathbf{j}^1 & \mathbf{j}^2 & \cdots & \mathbf{j}^{N_t} \end{bmatrix};$$

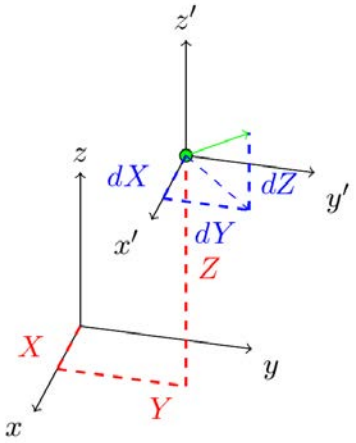

Figure 2.1: Dipole characterized by (x, y, z) projections

each $\mathbf{j}^i \in \mathbb{R}^{3N_s \times 1}$ vector contains current densities for each source $n \in 1...N_s$:

$$\mathbf{j}^i = \begin{bmatrix} \mathbf{j}_1^i \\ \mathbf{j}_2^i \\ \vdots \\ \mathbf{j}_{N_s}^i \end{bmatrix}$$

$\mathbf{j}_n^i \in \mathbb{R}^{3\times 1}$ being the current density vector of n-th source in i-th time point and $j_{n_x}^i, j_{n_y}^i, j_{n_z}^i$ – its respective vector projections:

$$\mathbf{j}_n^i = \begin{bmatrix} j_{n_x}^i \\ j_{n_y}^i \\ j_{n_z}^i \end{bmatrix}$$

Fixed dipole formalization. Another formalization can also be adopted, used in situations when source direction is supposed to be fixed and only the amplitude varies. The number of parameters thus is reduced to 4, and the Equation (2.1) becomes:

$$\boldsymbol{\phi}_0 = \mathbf{AS} \tag{2.2}$$

where the lead-field $\mathbf{A} \in \mathbb{R}^{N_c \times N_s}$ encodes the fixed positions and orientations of the dipoles, and the current amplitude matrix $\mathbf{S} \in \mathbb{R}^{N_s \times N_t}$ contains only the source amplitudes. The current amplitude matrix is formed in a similar way compared to the current density matrix $\mathbf{J}$, containing columns corresponding to each time instant $i \in 1...N_t$:

$$\mathbf{S} = \begin{bmatrix} \mathbf{s}^1 & \mathbf{s}^2 & \cdots & \mathbf{s}^{N_t} \end{bmatrix};$$

for each time instant i the vector $\mathbf{s}^i$ contains the amplitudes of all N_s sources:

$$\mathbf{s}^i = \begin{bmatrix} s_1^i \\ s_2^i \\ \vdots \\ s_{N_s}^i \end{bmatrix}$$

Both formalisms ((2.1) and (2.2)) are equivalent in fixed-oriented dipole context. Each current amplitude of n-th source can be calculated as Frobenius norm of current density vector $\mathbf{j}_n^i$:

$$s_n^i = \left|\left|\mathbf{j}_n^i\right|\right|$$

and the momentum information about each source is included in the **A** matrix:

$$\mathbf{a}_{mn} = \frac{\langle \mathbf{k}_{mn}, \mathbf{j}_n \rangle}{||\mathbf{j}_n||}$$

where $\langle \mathbf{k}_{mn}, \mathbf{j}_n \rangle$ denotes the inner product of vectors.

Both approaches presented above are commonly used for solving the brain source imaging problem. Anatomical information can help in determining the orientation of the dipoles (often taken orthogonal to the grey matter mesh), thus simplifying the inversion problem.

2.2.2 Propagation models

Given a position for a dipolar source, a propagation medium model has to be chosen in order to compute the lead-field gain k_{mn}. Various approaches to propagation modeling are discussed in this section of the chapter, starting with simple analytical models (such as the Infinite Homogeneous Medium model (IHM) or One Sphere Medium model (OSM) up to more precise numerical models (such as Boundary Element Method model and Finite Element Method model) that are obtained using patients' CT and MRI images. Regardless of the choice of the model, the conductivity values are crucial parameters on which the precision of the forward model relies, thus preconditioning the accuracy of the source localization task.

2.2.2.1 Analytical models

Analytical models offer direct analytically calculable solutions for the forward model. The main advantage of analytical models is their fast calculation time, which is an important feature since this calculation must be carried out numerous times during the dipole fitting procedure. Furthermore, only few parameters have to be introduced – conductivity of the medium for Infinite Homogeneous Medium (IHM), and the conductivity, center and radius of the sphere for the One Sphere Medium model (OSM), reducing and controlling thus the possible causes of modeling errors or uncertainties.

Infinite Homogeneous Medium (IHM). The simplest theoretical propagation model is the Infinite Homogeneous Medium (IHM), uniquely defined by a constant conductivity $\sigma \in \mathbb{R}$. In this context, the solution to Poisson's equation is given in [Sarvas 1987], giving the potential at a point $\boldsymbol{r}$ caused by an extended source $\mathbf{J}^i$ in region Ω:

$$\Phi(\boldsymbol{r}) = \frac{1}{4\pi\sigma} \int_\Omega \frac{\nabla \cdot \mathbf{J}^i(\boldsymbol{r}')}{\|\boldsymbol{r} - \boldsymbol{r}'\|} \mathrm{d}\boldsymbol{r}' \tag{2.3}$$

with $\nabla \cdot \mathbf{J}^i(\boldsymbol{r}')$ the divergence of the current density $\mathbf{J}^i$ at point source $\boldsymbol{r}'$. When reducing the source to a point at position $\boldsymbol{r}_0$ (see [Sarvas 1987] for more details), we obtain the approximation:

$$\Phi(\boldsymbol{r}) \approx \frac{1}{4\pi\sigma} \frac{\boldsymbol{r} - \boldsymbol{r}_0}{\|\boldsymbol{r} - \boldsymbol{r}_0\|^3} \mathbf{j} \tag{2.4}$$

Equation (2.4) lets us define the lead-field matrix elements for the **IHM** case as:

$$\mathbf{k}_{mn} = \frac{1}{4\pi\sigma} \frac{\boldsymbol{r}_{\phi_m} - \boldsymbol{r}_{j_n}}{\|\boldsymbol{r}_{\phi_m} - \boldsymbol{r}_{j_n}\|^3} \tag{2.5}$$

with $\boldsymbol{r}_{\phi_m} \in \mathbb{R}^{1\times 3}$ as the position of the m-th sensor and $\boldsymbol{r}_{j_n} \in \mathbb{R}^{1\times 3}$ as the position of the n-th source. The potential varies with the angle of the dipole and decreases with the square of the distance to the source. The conductivity

parameter σ is crucial, and multiple studies have been carried out to determine the best approximations for the conductivities of different matters of the human head (more on the subject in 2.2.2.3).

When dealing with EEG measurements, such modeling seems too simplistic. Indeed, the electrical field is propagating through inhomogeneous head tissues (brain, skull, scalp) and the sensors are placed on the border between a conductor and a non conductor (*i.e.*, respectively head tissue and air). This introduces high errors between the actual electrical potential propagation and the one suggested by the IHM model. In the context of SEEG, the propagated field does not cross severe propagation barriers such as the skull bone, as it offers potential measurements deeper inside the brain volume. The forward model errors caused by the volume inhomogeneity are likely to be less significant and an IHM model might be eligible. The validity of such hypothesis will be evaluated in the next chapter.

One Sphere Medium model (OSM). To adapt the model and take into account the fact that the head is finite and the air is not conducting, the One Sphere Medium model (OSM) has been proposed, roughly modeling the shape of the head. Several solutions have been proposed to compute the propagation within a sphere. Originally, an initial solution to the problem was provided by [Wilson and Bayley 1950], and then mathematically simplified for potential on the surface of the sphere by [Frank 1952]. However, both of these solutions are undetermined for some particular points. The solution given by [Brody et al. 1973] is free of indeterminations, but can only calculate the potential on the surface of the sphere. In this work we are therefore using the formulation proposed by [Yao 2000], free of indetermination and able to compute the potential everywhere inside the sphere. For a sphere with the radius r_{sp}, the potentials can be calculated in any point $\boldsymbol{r}$ in the sphere [Yao 2000]:

$$\Phi(\boldsymbol{r}) = \frac{1}{4\pi\sigma}\left[\frac{\boldsymbol{r}-\boldsymbol{r}_0}{\|\boldsymbol{r}-\boldsymbol{r}_0\|^3} + \frac{(\boldsymbol{r}-\chi\boldsymbol{r}_0)}{r_{sp}^3 r_{pi}^3} + \frac{1}{r_{sp}^3 r_{pi}}\left(\boldsymbol{r} + \frac{\boldsymbol{r}\frac{\|\boldsymbol{r}_0\|\|\boldsymbol{r}\|}{r_{sp}^2}cos\alpha - \chi\boldsymbol{r}_0}{r_{pi}+1-\frac{\|\boldsymbol{r}_0\|\cdot\|\boldsymbol{r}\|}{r_{sp}^2}cos\alpha}\right)\right]\mathbf{j} \tag{2.6}$$

with $\chi = \frac{\|\boldsymbol{r}\|^2}{r_{sp}^2}$, the center of the sphere being taken from the origin of the coordinates. $r_{pi} = \frac{\|\boldsymbol{r}-\boldsymbol{r}_0\|}{\|\boldsymbol{r}\|}$ is the ratio between the source to sensor distance and the sensor distance to the center of the sphere. α is the angle between vectors $\boldsymbol{r}$ and $\boldsymbol{r}_0$. These parameters are illustrated in Figure 2.2.

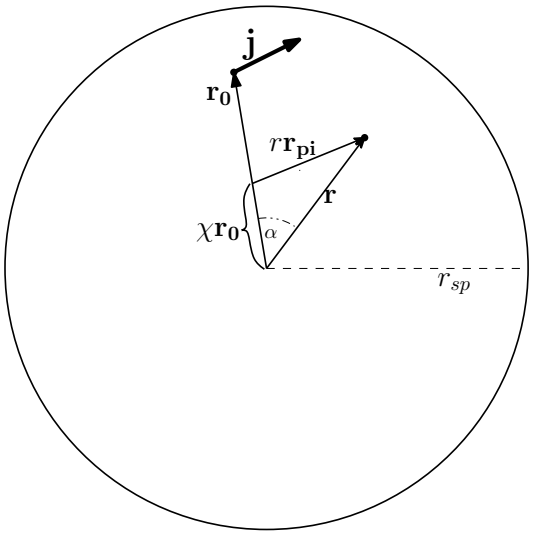

Figure 2.2: Dipole in a homogeneously conducting sphere.

The OSM lead-field matrix elements are then calculated as :

$$\mathbf{k}_{mn} = \frac{1}{4\pi\sigma}\left[\frac{\boldsymbol{r}_{\phi_m} - \boldsymbol{r}_{j_n}}{\|\boldsymbol{r}_{\phi_m} - \boldsymbol{r}_{j_n}\|^3} + \frac{\left(\boldsymbol{r}_{\phi_m} - \frac{\|\boldsymbol{r}_{\phi_m}\|^2}{r_{sp}^2}\boldsymbol{r}_{j_n}\right)}{r_{sp}^3 r_{pi}^3} + \frac{1}{r_{sp}^3 r_{pi}}\left(\boldsymbol{r}_{\phi_m} + \frac{\boldsymbol{r}_{\phi_m}\frac{\|\boldsymbol{r}_{j_n}\|\|\boldsymbol{r}_{\phi_m}\|}{r_{sp}^2}cos\alpha - \frac{\|\boldsymbol{r}_{\phi_m}\|^2}{r_{sp}^2}\boldsymbol{r}_{j_n}}{r_{pi} + 1 - \frac{\|\boldsymbol{r}_{j_n}\|\|\boldsymbol{r}_{\phi_m}\|}{r_{sp}^2}cos\alpha}\right)\right] \tag{2.7}$$

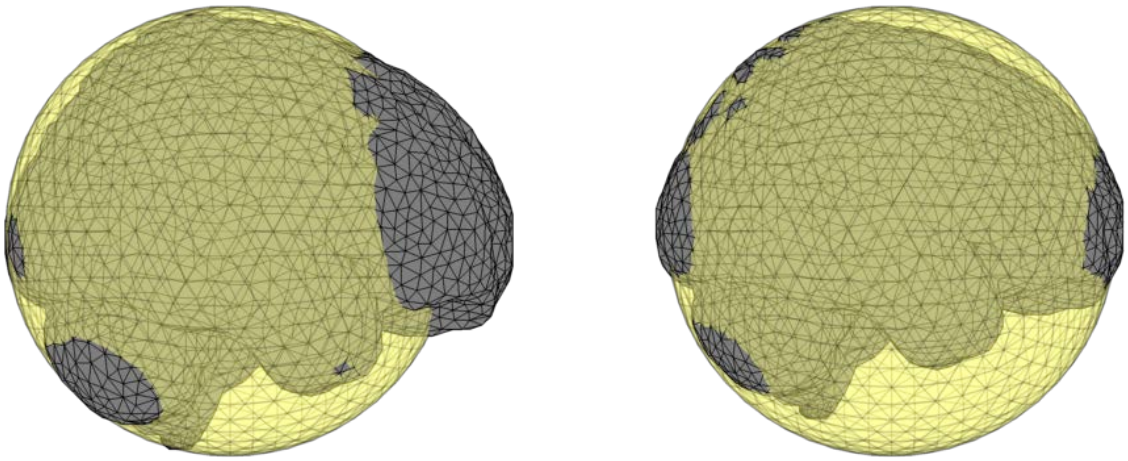

(a) **(b)**

Figure 2.3: Example of sphere fitted manually (a) and automatically (b)

It should be noted that when the radius of the sphere is increased to infinity, Equations (2.6) and (2.7) become the equations describing the IHM model (Equations (2.4) and (2.5) respectively). The terms in Equations (2.6) and (2.7) containing the radius parameter r_{sp} can then be seen as correction terms of the IHM approximation. Modeling skull as a non-conductive sphere shell is expected to provide a more precise forward problem calculation, therefore more precise localization when dealing with the sources or the electrodes situated close to the frontier. An important issue to address when using One Sphere Medium model is the method to estimate the parameters (center and radius) of the sphere, usually carried out by fitting a sphere on the inner skull mesh. The localization results are sensitive to the quality of this sphere fitting step, especially for the sensors close to the skull for which the potential reflection on the skull bone is significant. Fitting can be done manually or with automated algorithms. As illustrated in Figure 2.3, the fitting results can vary greatly from one estimation to another (a third solution, not shown here but used further in the manuscript, includes all the mesh points inside the sphere in order to be able to compute forward problems for all potential brain sources). Depending on the brain's region of interest, a more elaborate solution proposes to fit the sphere locally in order to better model the skull bone conductivity barrier near this area.

Multiple optimizations and derived works on OSM have been developed, some of them including Legendre series [Munck and Peters 1993], involving the evaluation of many terms of polynomials and yielding considerably expensive calculation costs. Also, a range of more sophisticated models derived from OSM have been proposed, such as multiple spheres to model the inner and outer border of the skull as well as the scalp [Roth et al. 1993], eccentric spheres [Cuffin 1991] or multiple overlapping spheres [Huang et al. 1999].

2.2.2.2 Realistic head models

As medical imaging (such as CT and MRI) becomes more and more accessible, realistic individual head models can be built to produce more precise forward lead-field. Realistic head models are obtained using medical imaging modalities in order to construct precise geometry of the head for each individual patient. The 3D volume (from a

combination of CT and MRI images) is segmented for identifying the boundaries of each brain's tissues, providing a mesh of each head's compartments. Different conductivity values are attributed to each of these different tissues, and the anisotropy of the tissues can also be taken into account for more elaborated models. A discretized version of Poisson's equation is used to calculate the potentials in each node and for each sensor (see [Vallaghé 2008] for more details). The two most common realistic head models used are Boundary Element Method model (BEM) and Finite Element Method model (FEM).

One of the realistic head models is based on the Finite Element Method (FEM). FEM divides the whole volume in discrete volumetric elements and assigns a scalar conductivity for each of them (Figure 2.4). Note that FEM can also treat realistic anisotropic tissue models [Bangera et al. 2010, Dannhauer et al. 2011], in which case one should consider a conductivity tensor. Generally, as is the case in the scope of this thesis, five isotropic compartments are considered, as illustrated in Figure 2.4: gray matter, white matter, cerebrospinal fluid (CSL), bone and scalp. The main inconvenient of this model is its high number of user parameters (such as the number of nodes and the conductivities of each compartment). It might also be greatly influenced by the outcomes of the segmentation algorithms used to delimit the compartments.

Nowadays BEM is becoming one of the standard methodologies. It can take into account the individual geometry of the brain, skull (inner and outer) and scalp, creating a mesh for each boundary. Afterward, for each domain, homogeneous isotropic conductivities are assigned and solved for all mesh points. While BEM is restricted to homogeneous isotropic conductivities, it is widely used because of reduced computational costs compared to FEM. BEM provides the potential values only at the interfaces and the boundary of the volume. However, using a boundary problem in differential equations, the potential can be evaluated at any given point in the volume (see *e.g.*, [Hofmanis 2013]).

Figure 2.4: FEM head model with 5 different volumes

2.2.2.3 Conductivity of the propagation medium

Conductivity of the propagation medium plays a crucial role in the precision of the localization and the forward problem, especially in realistic head models. A number of researches have been carried out to determine the best approximations for the conductivities of different matters of the human head [Ferree et al. 2000, Haueisen et al. 2002, Hoekema et al. 2003, Oostendorp et al. 2000, Rush and Driscoll 1968]. Reports range from 0.12 to 0.48 S/m for the brain [B. Ranck Jr. 1963, Nicholson 1965, Van Harreveld et al. 1963], the value usually chosen being $0.3S/m$

[Cosandier-Rimélé et al. 2007]. Conductivities in the range from 0.006 to 0.013 S/m are attributed to the human bone [Geddes and Baker 1967, Kosterich et al. 1983], whereas scalp conductivity is estimated to be around 0.43 S/m [Burger and van Milaan 1943]. This field of research for conductivity estimation is still active. For example, a combined in-vitro and in-vivo study by [Oostendorp et al. 2000] suggests using skull conductivity at 0.015 with a brain : skull : scalp ratio of $1 : 1/15 : 1$. Intracerebral stimulations are also used in order to adjust the conductivity parameters since the stimulation signal and its amplitude is known [Altakroury et al. 2016, Koessler et al. 2017].

2.2.3 Sensor positions

With a chosen source and propagation model in mind, sensor positions must be extracted in order to get the positions where the potential measurements have to be calculated. Mislocalization of the measuring sensors has a considerable impact on the precision of the localization, more or less comparable to the effect of measurement noise depending on the study [Khosla et al. 1999, Van Hoey et al. 2000, Wang and Gotman 2001]. The noise is supposed to be rather weak in the context of SEEG measurements, making the sensor position estimation an important step toward reliable SEEG source localization. Nowadays, in the case of EEG, the most practical option is measuring the exact 3D electrode positions with a digitizer [Koessler et al. 2011, Towle et al. 1993].

This approach being impossible when it comes to SEEG, a method for localization of the sensors using magnetic resonance imaging (MRI) combined with computed tomography (CT) has been developed in the team (presented in [Hofmanis et al. 2011]). It uses image processing and object recognition from the combination of MRI and CT to improve the localization in different matters of the head (bone, scalp, white matter, gray matter, cerebral fluid).

In both cases (scalp EEG and SEEG), the sensors are assumed to be 0-dimensional (i.e. they are modeled as points in space, situated, in principle, in the middle of the actual sensor). While this approximation seems natural for scalp electrodes (situated far from the brain sources), one might question the influence of electrode size on the source models in the SEEG case, when electrodes and sources might be close. Indeed, this influence exists, but it has been proven that the error of the ideal electrode approximation is restricted to the vicinity of the electrode and seems negligible when more than 2 mm away from it [von Ellenrieder et al. 2012b].

2.3 Brain Source localization

Electric brain source localization consists in determining the positions, orientations and strength of neural sources using the electrical potential measurements. This has a large spectrum of applications including cognitive research (functional cartography of the human brain) and clinical use (epileptic source localization). It can be used to map functional areas prior to cortical resections considered to cure pharmaco-resistant epilepsies, and prior to epilepsy surgery to help identify epileptogenic foci and preserve functional cortical areas.

The reliability of the localization methods is based on the *a priori* information that we can supply to the localization method.

Localization of the sources could be categorized in two main groups: distributed source methods and equivalent current dipole (ECD) approaches. The distributed source model supposes that the number of dipoles is far bigger than the number of measurements. The problem is underdetermined and there is no unique solution, therefore different methods are used to regularize the problem and decrease the degrees of freedom of the variables to be estimated. Inversely, ECD model relies on the assumptions that the electrical field is produced by a small number of dominant

dipoles. Since there are more measurements than parameters, the problem is overdetermined. However, due to the non-linearity of the problem and the uncertainties introduced by the different steps of the forward modeling as well as the measurement noise, the resolution of this problem is not straightforward.

2.3.1 Distributed source models

When the exact number of sources to be localized is not known or cannot be reduced to a limited set of one or two, the distribution of activity over the entire head's volume is estimated based on a distributed source model. Distributed source models cover the source space using a grid and by placing dipoles on each grid point, each of these points being a possible source. The number of these elementary sources is of the order of several thousands, while the number of measurements is near one hundred, making this problem severely underdetermined, *i.e.*, an infinite number current source distributions can produce the same measurements, and constraints are needed to reduce the ambiguity of the solution. The main constraint is of an anatomical order. Using information extracted from MR images, segmentation can be applied to detect geometry of different matters (2.2.2.2). Since primary sources are widely believed to be restricted to the cortex, segmented geometry information is used and dipoles are placed on the cortex mesh points. Since the apical dendrites that produce the measured fields are oriented normally on the surface, we can further constrain each of these dipoles to be normal to the surface of cortex. The number of elementary dipoles is reduced and for each dipole the unknowns are reduced: position and direction of each dipole is considered to be fixed and only amplitude can change with time. According to this hypothesis, the used forward model takes the following form (2.2):

$$\boldsymbol{\phi}_0 = \mathbf{AS}$$

The solution space is highly reduced but still remains far larger than the measurements space. Additional restrictions can be mathematically formulated based on priors on the temporal and spatial distributions of the source activities.

Let us define a measurement (or montage) matrix as $\mathbf{M}$ (more details in Subsection 2.4.2) in order to deal with different measurement montages, *e.g.*, the classical common reference montage often used in scalp measurements but it is possible to work with other montages. The gain matrix $\mathbf{G}$ is then redefined by

$$\mathbf{G} = \mathbf{MA}$$

and the forward Equation (2.2) becomes

$$\boldsymbol{\phi} = \mathbf{GS} \tag{2.8}$$

Regularization constraints are formalized by the introduction of a regularization operator $\mathbf{R}(.)$. This operator provides stability to the solution so that small variations in data will not lead to large variations in the estimated source configuration.

In practical situations, one does not have access neither to theoretical signals $\boldsymbol{\phi}$ nor to $\boldsymbol{\phi}_0$, because real signals are contaminated by noise and artifacts. These real noisy measurements will be noted as $\boldsymbol{\phi}_n$ (see more about signal pre-processing in Section 2.4). To estimate the amplitudes of sources $\mathbf{S}$, the argument to minimize will then be written as:

$$\hat{\mathbf{S}} = argmin_S(||\boldsymbol{\phi}_n - \mathbf{GS}||^2 + \lambda \mathbf{R}(\mathbf{S})) \tag{2.9}$$

where the first minimization term is the reconstruction error, scalar λ is the regularization parameter (accounting for the noise) and $\mathbf{R}$ is the regularization operator.

Any instantaneous, 3D, discrete linear solution for the EEG inverse problem can be written as:

$$\hat{\mathbf{S}} = \mathbf{T}\boldsymbol{\phi}_n \tag{2.10}$$

where matrix $\mathbf{T} \in \mathbb{R}^{N_s \times N_c}$ differs given the choice of the constraints in $\mathbf{R}$.

In the following, we shortly describe the main methods for solving the distributed source problem (more detailed reviews in [Baillet et al. 2001, Michel et al. 2004b]). The inverse solutions that have been proposed through the years in literature differ in the choice of the constraints applied to regularize the problem. All of these methods use the same solving schema, but different assumptions are applied to construct the matrix $\mathbf{T}$ and therefore to identify an optimal or realistic source strength configuration. They range from purely mathematical (*i.e.*, smallest L-2 Norm) to the incorporation of information from alternate modalities like imaging techniques or even biophysical and physiological knowledge [Michel et al. 2004b]. Therefore, even though the basis of the method does not demand *a priori* information, the model is constrained to the validity of *prior* information used to regularize the problem.

Minimum norm (MN) The basic assumption underlying this inversion is that the current distribution should have minimum overall energy (smallest L-2 Norm). This method gives a unique solution (lowest overall intensity and exact fit of the data at the same time), but it has no physiological basis. The algorithm punishes solutions with strong activity on a large number of potential source points. That is to say, it favors weak and localized activity patterns. Therefore, a minimum norm algorithm favors superficial sources (a smaller amplitude is necessary to generate the same level of measurements compared to deep sources). Minimum norm solution [Hämäläinen and Ilmoniemi 1994] corresponds to (2.10) with $\mathbf{T} = \mathbf{G}^+$ and $\lambda = 0$, and its regularized counterpart [Okada 1985] when

$$\mathbf{T} = \mathbf{G}^T(\mathbf{G}\mathbf{G}^T + \lambda \mathbf{I}_{N_s})^{-1} \tag{2.11}$$

and λ estimated using cross-validation methods or the L-curve [Hansen 1999].

Weighted minimum norm The main problem with the general minimum norm solution is that it has a tendency to favor superficial sources, therefore different weighting strategies are proposed in literature. By introducing the inverse of source covariance $\mathbf{C}_s^{-1}$ factorized as $\mathbf{C}_s^{-1} = \mathbf{W}\mathbf{W}^T$ [Baillet et al. 2001], matrix $\mathbf{T}$ can be rewritten as

$$\mathbf{T} = \mathbf{W}\mathbf{W}^T\mathbf{G}^T(\mathbf{G}\mathbf{W}\mathbf{W}^T\mathbf{G}^T + \lambda \mathbf{I}_{N_s})^{-1} \tag{2.12}$$

This form of stating the problem was chosen to illustrate the variety of different EEG imaging applications that have been proposed, which are different between themselves mainly in the way of defining matrix $\mathbf{W}$. Different methods such as using the norm of the columns of the lead field matrix [Lawson and Hanson 1974], averaging kernels [de Peralta Menendez et al. 1997] and more, drawn from different other areas or inverse problems. Different mathematical approaches were applied like constructing the weighting function in source space [Greenblatt 1993] or iteratively changing weight according to the solutions estimated in the previous step [Gorodnitsky et al. 1995]. Lately, more methods have been developed that take into account the actual head structure and constraints on radial components when sources approach the surface of the brain [Peralta-Menendez et al. 1998]. Furthermore, the assumption

that the activities of neighboring neuronal sources are correlated and synchronized can be used (LORETA) [Pascual-Marqui et al. 1994]. The Laplacian operator is used in the implementation of constraints to favor smooth spatial distribution of source amplitudes. This can cause the problem of providing rather blurred (or "over-smoothed") solutions [Korats 2016, 3rd chapter]. Nevertheless, derivatives from this method have been proposed to exclude bias in the presence of measurements and structured biological noise (sLORETA and eLORETA [Pascual-Marqui 2007]). Biological laws have also been introduced as constraints in solving the localization problem [de Peralta Menendez et al. 2001]. This is by no means an extensive research on these methods but rather a sum-up of the most frequently used ones in this field of study.

It is worth noticing that the methods described above can be formulated in a Bayesian framework, using adequate probabilistic modeling [Wipf and Nagarajan 2009] of the source and noise distributions. Additional constraints and priors can be added under this formulation, providing extensions to the classical weighted minimum norm approaches. Different types of *a priori* information have been introduced, including information on neural currents, the sparse focal nature of the sources, combined spatial and temporal constraints, introduction of anatomical *priors* from imaging modalities, as well as strategies to penalize ghost sources [Michel et al. 2004b].

Scanning methods. Since different mathematical principles are used in multiple methods, it is hard to draw a clear line to categorize different methods of solving the inverse problem. However, another strategy that should be mentioned is the so-called **scanning methods**. They are mainly used when there is an *a priori* about strong clustering or dominance of sources.

EPIFOCUS is developed for the analysis of focal epileptic activity when a single dominant source is assumed to be present [Michel et al. 2004a]. It is a linear inverse method that scans all the solution points and calculates the current density vector, that can then be interpreted as a relative probability of finding a single source at each specific point. This method is prone to fail in situations when multiple dominant sources are present. However, this method has some notable advantages, such as the fact that in contrast with ECD methods, it avoids the non-linear non-convex optimization, as well as its remarkable robustness against noise [de Peralta Menendez et al. 2001].

Another example is the beamformer approach – it performs spatial filtering on data from a sensor array in order to discriminate between signals arriving from the investigated location and those from different locations. The basis of beamforming comes from radar and sonar signal processing, but the technique has been since applied in a large range of different fields of study including biological signal processing (mainly MEG) [Sekihara et al. 2001].

One of the most widely used scanning methods was proposed by Mosher *et. al* [Mosher et al. 1992] – they adapted a scanning technique used in radars to isolate signals from noise. This method, called MUltiple SIgnal Classification (MUSIC) is based on an eigenvalue decomposition of the measurement data in order to identify the underlying components (the signal space). Afterward, the whole brain volume is scanned for source localizations that contribute to the signal space. For each source found, the time courses of their moments are determined. An improved algorithm called RAP-MUSIC (Recursively Applied and Projected MUSIC) was proposed for dealing with the shortcomings of the original MUSIC algorithm concerning correlated sources in the presence of noise and the application to the realistic head models [Mosher and Leahy 1998].

Figure 2.5: Dipolar models

2.3.2 Overdetermined models (Dipole fitting)

A possible assumption about the brain activity is that it can be explained by a limited number of sources [Scherg 1990] and that the volume of activity is small (compared to the distance to the sensors). This assumption is at the core of ECD methods. Dipole fitting methods are known to provide accurate localization in situations of highly focal activations, for example during somatosensory stimulation or epileptic discharges [Fuchs et al. 2004, Michel et al. 2004b]. These models were first used in 1975 and are still the most commonly used ones in clinical routines. They are useful because they can produce a link between the topography of the head and a small number of parameters.

In case of dipolar model, we are searching for dipoles in the brain volume, each characterized by six parameters. The search is done by minimizing the error of reconstruction or, more precisely, the squared error between the measured signals and the result of the forward problem for the estimated sources. This approach is called the least-squares dipole fitting. The simplest approach of dipolar models is to find the dipole parameters for a given time instant ($N_t = 1$), which is often used for evoked activity or pre-epileptic seizure spikes. When multiple consecutive time instants are considered, the dipoles might be moving with time and the approach used is then called *moving dipole model*. Inversely, if the position is considered to be fixed for the whole time window, only the dipole moment and amplitude are evaluated at each time sample, and then the corresponding inversion method is called *rotating dipole model*. Finally, if both position and moment are fixed for a given time window, only the amplitude is free to vary over time, the *fixed dipole model* is used. Applying the *fixed dipole model* at each instant of a time window independently is equivalent to applying the *moving dipole model* on this time window.

2.3.2.1 Optimization for ECD methods

Assumption of focal and sparse sources brings us to the overdetermined optimization problem, having more equations than unknowns. In this section more details about how the dipole fitting is done are presented. The forward problem and therefore also the optimization is linearly dependent of the direction and amplitude, however, it is non-linearly dependent on the position of the dipole. The common practice is to separate the problem in multiple parts. Different approaches might be used.

Rotating dipole The problem is as stated in Equation (2.1). Let us suppose, that we have a initial supposition about the source position. In a perfect situation (no noise, already the right position) if we would have as many non-collinear measurements as parameters to optimize, inversing the lead field matrix would yield the solution.

$$\mathbf{j} = \mathbf{K}^{-1}\boldsymbol{\phi}$$

However, neither the position is implicitly the right one, nor is our lead-field matrix square. We have an overdetermined system and therefore the inverse matrix is replaced by a pseudo-inverse matrix of K (K^+). Therefore, we can calculate the estimation of the dipole direction $\hat{\mathbf{j}}$:

$$\hat{\mathbf{j}} = K^+ \boldsymbol{\phi}$$

Once we have an estimation of the direction of the dipole, we can fix this direction and use some non-linear optimization algorithms (such as Simplex or SQP, more details below) to find the position that corresponds to the minimal measurement reconstruction error.

This approach is called *rotating dipole* because, when taking a time window, the position will be fixed (the one found by non-linear optimization) but the projections of the amplitude (meaning the amplitude and the direction) will be free to have varying values across different time samples.

Fixed dipole The approach here is quite similar as in the case of the *rotating dipole*, but we are using the problem statement as in Equation (2.8). Therefore, only the amplitude is separated from the other parameters. For a given initial position and direction, the amplitude is estimated:

$$\hat{s} = G^+ \boldsymbol{\phi}$$

Afterwards, considering this estimated amplitude, all the other parameters are estimated with a non-linear optimization. This approach is called *fixed dipole*, because when taking a time window, the position and the direction will be fixed, amplitude being the only parameter that is able to change over time.

Moving dipole In the case of a freely moving dipole over the time window, two possible approaches exist:

- using *fixed dipole* for every time sample from the time window separately – therefore the dipole will be free to vary in position, direction and amplitude over the time window.
- optimizing all parameters of the dipole with the non-linear solver altogether for every time sample from the time window. This is different from the first approach, since no pseudo-inverse matrix calculation is done.

Non linear optimization is a considerable part of finding the most plausible dipole parameters in all of the cases mentioned above. Problematics related to this optimization will be discussed further in this section.

To find a minimum of a function based on optimization, objective function and possibly constraints should be defined. In our case, the function to optimize $f(\mathbf{x})$ is the accuracy of the forward problem against the given data:

$$f(x) = \frac{\|\boldsymbol{\phi} - \boldsymbol{\phi}_0(\mathbf{x})\|}{\|\boldsymbol{\phi}\|} \tag{2.13}$$

where $\boldsymbol{\phi}$ is the electrical potential data used and $\boldsymbol{\phi}_0$ is the data calculated by the forward model for current iteration $\mathbf{x}$ (containing the parameters of the dipole to be optimized with the method).

The modern era of optimization was marked by the development of the simplex method in 1947 by George Dantzig. It was initially a method to solve only linear problems, but has since been revised and refined multiple times [Nocedal and Wright 2006]. The most common on the fly solution used to solve non-linear optimization

problems is the Nelder-Mead **simplex algorithm** [Nelder and Mead 1965]. This is a derivative-free optimization (DFO) algorithm. It uses a simplex of $n+1$ points for n-dimensional vectors x. The algorithm first makes a simplex around the initial guess x_0 by adding 5% of each component $x_0(i)$ to x_0, and using these n vectors as elements of the simplex in addition to x_0. (It uses 0.00025 as component i if $x_0(i) = 0$.) Then, the algorithm modifies the simplex repeatedly, according to a set of rules, and replaces the points of simplex systematically until no further change of the points yields better results [Lagarias et al. 1998]. This method is sensitive to the size of the initially chosen simplex and this needs to be addressed when starting the numerical calculations.

However, this method lacks an essential part of problem definition that we need in the source localization problem – constraints function definition. This is crucial in order to constrain the localization inside the brain volume (or in the sphere that is chosen to model the head).

Another alternative to solve the non-linear problem is to use **sequential quadratic programming method** (SQP)[Boggs and Tolle 1996]. SQP finds the minimum of a problem specified by

$$\min_x f(x) \text{ such that } c(x) \leq 0 \tag{2.14}$$

where $f(x)$ if the same objective function defined in Equation (2.13) and $c(x)$ defines the constrained solution space.

The SQP approach is one of the most effective methods of nonlinearly constrained optimization – it generates steps by solving quadratic subproblems. This approach can be used for different optimization frameworks and is appropriate for both small and large problems. SQP is especially advantageous when solving problems with significant nonlinearities in the constraints. Depending on the scale of the problem (number of variables to optimize), different algorithms can be applied. Large-scale algorithms with sparse problems need to use an efficient way of computing matrices – they do not need to store nor operate on full matrices. Medium-scale methods internally create full matrices and use dense linear algebra. Boundary satisfaction is of high importance and in source localization these constraints can be of a different nature and fiercity – we can be searching the sources in the whole brain or only in some part of the brain *i.e.*, gray matter, hippocampus etc.

For numerical optimization, different parameters should be refined for the specific optimization problem, most importantly *tolerance on function value* to define the smallest change of objective function between iterations, *tolerance to x* to define the smallest argument change between iterations, *tolerance to constraint violation* to define how strictly the constraints should be respected, *maximum number of function evaluations* and *maximum number of iterations*. These parameters are defined by the user by considering the particularities of the problem. This is usually done with an iterative approach by analyzing the optimization results and bottlenecks during the numerical calculations.

Initialization In the case of dipole fitting, the problem is non linear. Multiple local minima exist, and strategies have to be adopted to avoid finding local minima instead of the global one. Empirical guesses of the initialization might be extracted from the data by *e.g.*, interpolating the measurements, finding maxima and minima and initializing in the middle of a focal couple of maximum and minimum. However, such methods are not general enough and are very sensitive to noise, especially when the localization is performed on a single instant. A multi-start approach is generally adopted, where multiple starting points are given to the optimization function, and each one might lead to a different local minimum [Glover and Kochenberger 2003]. The best solution can be chosen afterwards based on

a given criterion, most commonly the Goodness of fit (GOF), which can be calculated from the minimized objective function $f(x)$ (from (2.13)) as

$$GOF = 1 - f(x)^2 \tag{2.15}$$

2.3.3 Source localization with SEEG

Few studies have been carried out on the problem of SEEG brain source imaging. The dipole fitting approach has been studied in [Chang et al. 2005] based on a simulated SEEG setup. Beamforming and RAP-MUSIC algorithms were tested with three parallel electrodes in a semi-infinite medium using white and correlated noise (modeled as another dipolar source), and the orientation of the dipoles were parallel to the sensors. The results showed that RAP-MUSIC performed better in the tested setups (distinguishing sources with non-overlapping time-courses as close as 0.4—0.6mm while Beamformer's limit was 1.2 cm). The localization errors remained below 1cm even with the highest noise samples simulated. The main take-away was that it is possible to use source localization methods that are traditionally applied to EEG for source detection from intra-cerebral measurements. However, further investigation, using more realistic models, was not carried out to verify the performances and usefulness in a clinical setting.

Later on, a study by [Yvert et al. 2005] was carried out using real patient's SEEG measurements dealing with auditory evoked potentials. Distributed source models were used for source localization and proved to be robust to increasing levels of noise. In particular, the authors demonstrated that the solution remained robust even after removing the sensors with maximum potential, meaning that the source configuration might be reliably estimated by a limited set of distant sensors.

As sensor configuration in the SEEG setup is different, so are the conditions for their analysis. Since in the case of SEEG the sensor is actually in the medium, doubts could exist about the size and geometry of the sensor's influence on the forward problem. However, studies of simulated SEEG measurements in [von Ellenrieder et al. 2012b] showed that the sensor's size influence on the measured electrical potential is negligible, if the electric source activity is located more than $\approx 2mm$ away from the contact. Furthermore, bigger sensors could be used (leading to lower impedance) without compromising the quality of inverse problem results. The main result of [von Ellenrieder et al. 2012b] is that an ideal electrode model (sensor represented as one point) is a good approximation of a detailed electrode model - this relaxes constraints for many localizations methods. The study used BEM to compute the perturbation on the electrical potential distribution caused by the presence of the measuring electrode and FEM to simulate measurements in a heterogeneous anisotropic brain model. They also showed that there is a notable influence of modeling the heterogeneity and anisotropy of the brain. The topic of sensor position errors has been studied in EEG [Van Hoey et al. 2000] but this problem also applies to SEEG. Fortunately, the position of SEEG electrodes is more obvious because during stereotaxic positioning of SEEG electrodes, a control CT scan is also carried out. Since the localization result errors vary depending on the sensor positions, each patient's case has to be studied separately.

The different specificities of the SEEG-based localization problem will be discussed in more details in the next chapter (3), which presents our main contributions for solving the ECD problem in SEEG.

2.4 Data pre-processing

To increase the reliability of the localization results and to help in regularizing the solution, multiple pre-processing steps have to be carried out. This section briefly addresses them separately. Because of the presence of the measuring equipment, reference and measurement noise must be considered in the model. Other activities might disturb the localization, so this problem also needs to be addressed.

2.4.1 Signal denoising

When recording EEG/SEEG, the signal is virtually always contaminated by different sources of noise and artifacts. The difference we make between the two types of perturbation consists in their nature: noise is supposed to be random, while artifacts are signals issued from other sources than the sources of interest, in our cases the cerebral dipoles to be localized.

Artifact sources are often present on the surface EEG recordings (see *e.g.*, [Vázquez et al. 2012]) and they can be issued by different sources, physiological or not. The most common are ocular artifacts (eye movements, eye blinking), cardiac artifacts, muscle artifacts, as well as classical 50/60 Hz electrical contamination. Artifact detection and removal are in general critical before EEG/SEEG signal analysis. One of the most widely employed techniques is the Independent Component Analysis (ICA) based Blind Source Separation [Albera et al. 2012, Vázquez et al. 2012]. The main advantages of ICA are optimal resolution both in time and frequency domains, and the lack of requirement for signal stationarity [Hyvärinen and Oja 2000]. However, this approach needs to be completed by a source selection procedure which can be either user driven, using different thresholding rules and thresholding values determined from empirical experiments, or automatic, by some classification procedure [Vázquez et al. 2012].

Unlike surface, the SEEG signals are almost artifact-free, except for one thing: they are often measured with respect to a reference electrode that is usually placed on the surface of the scalp [Menon 2012, Ranta and Madhu 2012]. Because of this electrode, common surface artifacts might appear on the (common reference) raw SEEG recordings. Their nature partially depends on the position of the reference electrode. For example, at the CHRU Nancy Hospital, this electrode is often placed in the FPz position of the classical 10-20 montage (see Figure 1.10), close to the eyes and thus potentially affected by eye artifacts. Besides, regardless of the reference electrode position, 50 Hz electrical artifact can also contaminate the measurements. In our study, a notch filter for 50 Hz is applied, as well as reference canceling (more details in Subsection 2.4.2).

Concerning the random noise, two types can be distinguished: instrumental noise and environmental noise. When considering the particular case of SEEG measurements, instrumental noise is practically absent because the amplifiers are of excellent quality and their rate of rejection in common mode is of $130dB$. Environmental noise is mainly due to background physiological sources located far from the measuring electrodes, modeled as random sequences also. The level of this type of (random) background noise can be variable and it needs to be considered with respect to the amplitude of the signals of interest, *i.e.*, with respect to a signal to noise ratio that will influence the localization results. Denoising can be done using different techniques. For example, if the noise characteristics are known, linear filters can be designed (low-pass filter, notch filter, as for the 50 Hz artifact). For noise with unknown or nonstationary characteristics, denoising by wavelet decomposition can be used with generally very good results[Chui 2014, Quiroga and Garcia 2003].

It is noteworthy that there exist techniques optimally combining both (BSS and classification based) artifact detection and (wavelet based) denoising [Vázquez et al. 2012].

2.4.2 Elimination of the reference

Just as a reminder, a model of linear instantaneous intra-cerebral potential propagation is given by Equation (2.2)

$$\boldsymbol{\phi}_0 = \mathbf{AS}$$

where $\boldsymbol{\phi}_0$ is a vector ($N_c \times 1$) containing the potentials at the electrode positions, $\mathbf{A}$ is the gain (lead-field) matrix ($N_c \times N_s$)and $\mathbf{S}$ is a vector of source amplitudes ($N_s \times 1$).

When the acquisition takes place in a common reference frame, all the potentials are actually measured as a difference against a common extra sensor called a reference sensor. This is the case for both surface and depth electroencephalographic signals, always recorded with respect to some unknown time varying signal called reference.

Depending on the measuring setup, the reference electrode can be one among the usual measuring electrodes or a particular one, in principle situated far from the sources of interest. The former situation is typical for surface EEG, while the latter can be a good approximation for the SEEG recordings, especially when the depth electrodes implantation sites are far from the (scalp placed) reference electrode.

The question about the most appropriate choice of reference electrode has been a point of debate. Geselowitz showed that if the model takes into account the positions of the sensors, the choice of a particular reference electrode does not in any way change the relation between source and potential, except for an additive constant of no physical significance [Geselowitz 1998].

On the other hand, the inverse solution algorithms used in source localization assume that the potentials used as a starting point for estimating the sources are zero-referenced. Since the reference adds the same potential to every sensor's measurement (for one instant moment in time), the localization problem becomes more complicated [Koessler et al. 2010b].

One of the solutions for removing this constant is to center the data matrix. In the case of EEG this mathematically corresponds to the subtraction of the average value of the surface potential from all measurements, so the problem is rather easily solved and the solution is implemented directly in the source localization software. Physically speaking, this solution is rather well justified for scalp EEG, especially for high density montages with high coverage of the head surface. Indeed, as there is no net influx or leakage of current from the head, the overall sum of potentials on the head surface should be 0, which is readily obtained by average subtraction.

However, for SEEG signals, measurements are not equi-distributed in the brain, so the reference does not necessarily correspond to the average potential, because the sensors are not placed quasi-homogeneously around the head (as in the case of EEG). On the other hand, unlike in EEG, the reference electrode is not one among the depth electrodes, but rather a surface electrode placed outside the head, far from the measuring sites. In this case, one can assume that this reference sensor measures only activity that is independent from activities found in $\mathbf{S}$.

The common reference montage (CRM) measurements can be formally written as:

$$\boldsymbol{\phi}_{CRM} = \mathbf{AS} - \begin{bmatrix} 1 \\ 1 \\ \vdots \\ 1 \end{bmatrix} \cdot \phi_r \tag{2.16}$$

where $\phi_r \in \mathbb{R}^{1\times N_t}$ is the potential on the reference sensor.

The aim of reference elimination in SEEG is to estimate $\boldsymbol{\phi}_0$ from the referenced potential $\boldsymbol{\phi}_{CRM}$ under the hypothesis that ϕ_r is independent of the activities $\mathbf{S}$.

An automatic detection and removal of the reference signal from SEEG was proposed by Hu *et al.* in the case when a reference signal is obtained from a sensor on the scalp [Hu et al. 2007; 2008]. The reference is estimated in two stages. In the first stage, the potentials measured in a common reference montage are transformed in a bipolar montage:

$$\boldsymbol{\phi}_{BM} = \mathbf{M}_{BM}\boldsymbol{\phi}_{CRM} \tag{2.17}$$

where matrix $\mathbf{M}_{BM}$ calculates the difference between the neighboring sensors, and in the general case it can be formed as follows:

$$\mathbf{M}_{BM} = \begin{bmatrix} 1 & -1 & 0 & \cdots & \cdots & 0 \\ 0 & 1 & -1 & \ddots & \cdots & 0 \\ \vdots & \ddots & \ddots & \ddots & \ddots & \vdots \\ \vdots & \cdots & \ddots & 1 & -1 & 0 \\ 0 & \cdots & \cdots & 0 & 1 & -1 \end{bmatrix} \tag{2.18}$$

Afterwards, potentials in the form of a bipolar montage are decomposed into $P \leq N_c - 1$ independent or principal components:

$$\bar{\mathbf{S}}_{XCA} = \mathbf{G}_{XCA}\boldsymbol{\phi}_{BM} = \mathbf{G}_{XCA}\mathbf{M}_{BM}\boldsymbol{\phi}_{CRM} \tag{2.19}$$

where $\mathbf{G}_{XCA}$ is the decomposition matrix given either by PCA or ICA methods, XCA being a subscript designating the chosen method. It is important to note here that the P "sources" given by PCA or ICA are not the actual physical brain sources, but rather a basis for the measured signal decomposition.

The obtained reference-free signals $\bar{\mathbf{S}}_{XCA}$ are then used to estimate the reference ϕ_r as:

$$\hat{\phi}_r = -\frac{1}{N_c}\sum_{m=1}^{N_c}\left(\phi_{CRM,m} - \sum_{l=1}^{P}\frac{E\{\phi_{CRM,m}\bar{s}_l\}}{E\{\bar{s}_l^2\}}\bar{s}_l\right) \tag{2.20}$$

where $\phi_{CRM,m}$ are the elements of $\boldsymbol{\phi}_{CRM}$ and $\bar{s}_l$ is the l-th source recovered by (2.19), *i.e.*, the l-th element of $\bar{\mathbf{S}}_{XCA}$.

This technique was later improved using a solution based on blind source separation (BSS) [Ranta et al. 2010]. An equivalent solution using the minimum power/variance distortionless response (MPDR/MVDR) beamformer was proposed in [Madhu et al. 2012], where it is shown that this solution also maximizes the signal-to-noise ratio (SNR). This solution directly estimates the reference r itself as:

$$\hat{\phi}_r = \mathbf{w}^T\boldsymbol{\phi}_{CRM}, \text{ with } \mathbf{w} = -\frac{\mathbf{R}_{\boldsymbol{\phi}_{CRM}}^{-1}}{\mathbf{1}^T\mathbf{R}_{\boldsymbol{\phi}_{CRM}}^{-1}\mathbf{1}}\mathbf{1} \tag{2.21}$$

where $\mathbf{R}_{\boldsymbol{\phi}_{CRM}}$ is the covariance matrix of the measured signals $\boldsymbol{\phi}_{CRM}$ and $\mathbf{1}$ is a vector of ones.

A theoretical equivalence between solutions in [Hu et al. 2008] and [Madhu et al. 2012] have been discussed in [Ranta and Madhu 2012], where it is also shown that the solution [Madhu et al. 2012] is more robust, especially in the presence of noise.

The reference signal in EEG can be eliminated by doing a spatial averaging due to its homogeneous repartition on the scalp of the patient. SEEG does not benefit from this property, and spatial averaging will not yield the desired result. Alternatively, the reference signal can be eliminated sensor-wise by averaging epochs containing the event

of interest (such as an evoked potential or an epileptic spike – more information in the Subsection 2.4.3). Under the hypothesis of independence between the reference and the signal of interest, the reference signal is theoretically eliminated. The reference can also be successfully attenuated by using statistical approaches such as recently developed in the ESPaCE team [Madhu et al. 2012, Salido-Ruiz 2012].

2.4.3 Detection and averaging of spikes

In order to use the equivalent current dipole (ECD) methods (see Subsection 2.3.2), a dominant source (or few dominant sources) hypothesis must be valid. A dominant source is a spatially focal source whose energy is more important than that of other sources, which will be seen as background noise. Classical examples of sources corresponding to this description are interictal spikes, although it strongly depends on the actual recordings (see Figure 2.6).

If the hypothesis of a unique dominant dipole is too strong, one might use ECD methods also for localizing several but few spatially distinct dipoles involved in a network of simultaneous activation. For example, spikes and ictal discharges are related to different activity patterns and most importantly – different activation area locations (more details on the comparison can be found in [de Curtis and Avanzini 2001]). Besides, it is also possible to have different sources generating interictal spikes and originating in different locations can impact the recordings.

Summarizing, because of the influence of other physiological sources activated simultaneously with the dominant dipole (spikes), the recorded signals are corrupted by either multiple other strong dipoles or by background activities, assimilated to noise. Consequently, even a very distinct source (clearly seen on one electrode) will be barely visible on distant sensors, especially when other activities are located closer to these sensors, thus having stronger direct impact on the measurements. This means that a direct application of the localization methods will seldom be possible without pre-processing for improving the SNR.

Before any further analysis can be carried out, the spike-like activities corresponding to a dominant dipole must be detected and clustered by corresponding epileptic sources. This detection and identification can be done by experts (generally using both common reference montage and bipolar montage). If the expert certifies that only one source is present, spikes can be detected with the help of a simple high-pass filter and a threshold detection. However, more elaborated automated methods can also be used for spike detection and clusterization [Wilson and Emerson 2002]. These methods may use one channel, as well as multi-channel measurements, and can be generally categorized by the signal features they use: morphological features (imitating experts) or time-frequency ones. In most cases, in order to better distinguish the spikes, some filtering methods are applied such as wavelet transform, matched filters or the Kalman filter. Thus, spike detection can be applied and the exact spike time instants estimated, followed by spike clustering (for complete reviews please refer to in [Sardouie et al. 2015, Wilson and Emerson 2002]).

Once we have a collection of spikes, we can average potential measurements from spike instants (corresponding to a particular epileptic activity) on each sensor separately. This amplifies the effect of the spike activity in question and attenuates the other activities if they are independent from the spiking activity. Different algorithms to enhance the signals of interest have been proposed using weighted averages, such as xDAWN [Rivet et al. 2009], however in this thesis we use the simpler averaging approach as described earlier, providing satisfactory pre-processing results.

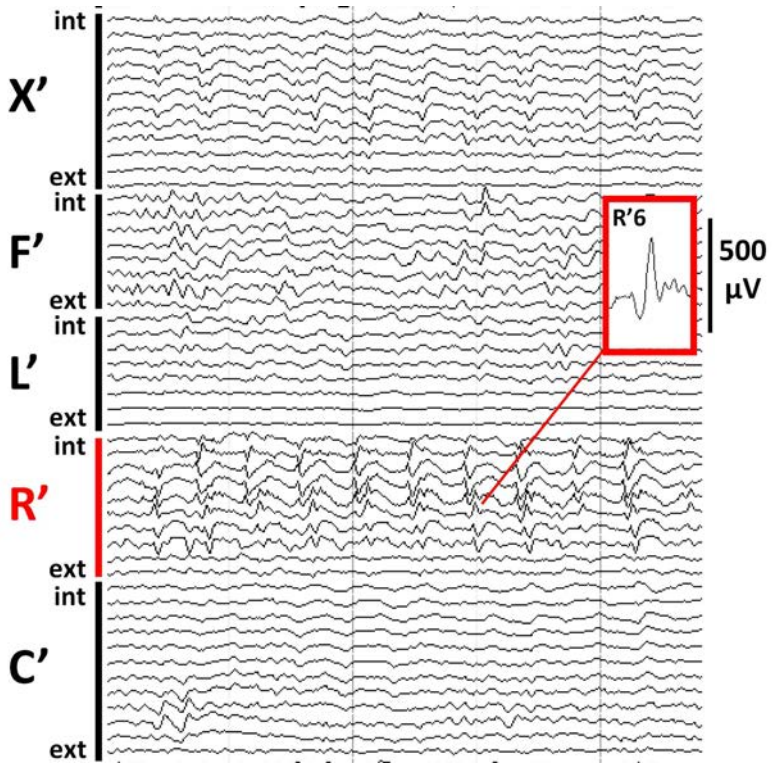

Figure 2.6: Real patient SEEG recordings during interictal spikes (different electrodes named with letters, multiple sensors per electrode)

2.5 Conclusions

In this chapter we have formalized the forward problem and introduced the classical methods to carry out its inversion for brain source localization. While most of the cited literature deals with MEG/EEG measurements, in the next chapter we will investigate the opportunity to localize the sources from SEEG recordings. We wanted to discuss the implementation of the methodological toolkit that is both effective and accurate in addressing the problem of localizing sources from SEEG intracerebral data. In this context, several of the opened questions will be addressed, such as the necessary level of propagation modeling, the adequation of the electrode's implantation usually met in clinical routine with the localization objective, the identifiability of the source depending on its position with respect to the brain volume and to the cloud of sensors, as well as the robustness to the level of white or spatially correlated noise. We restrict our analysis to the case of a dominant activity, *i.e.*, when a unique dipole stands out of the noise and needs to be identified. An ECD localization strategy is chosen and the method is tested under extensive simulations, as well as on real data of intracerebral stimulations and on real epileptic spikes recorded in the brain of a patient with temporal lobe epilepsy. The electrical stimulation is exogenous outside the evoked potentials that it can generate in the cortical surface, it is propagated in the different structures, it is dominant and its location is perfectly deterministic. The real epileptic spikes are generative in the epileptic zone, they are therefore partially localized and they are often dominant because enough expressed in the measurements. These two types of sources allow a validation of the tools and the parameters of source localization development.

Chapter 3

Localization in SEEG: feasibility study

The previous chapter describes the general methodology for dipolar source localization, widely studied using the surface potential recorded on the scalps of patients. As the invasive measurement setup in SEEG is different compared to the EEG setup, such methodologies need to be assessed in this particular context. We consider the case of a dominant dipole and we carry out the inversion based on a classical Sherg's ECD inversion. Several points that may influence the localization accuracy need to be discussed, beginning with the choice of the propagation model and the necessary sensor configuration for reliable localization results.

Regarding the propagation model, three levels of modeling will be investigated in this chapter (IHM, OSM and FEM). The SEEG measurements being collected inside the brain volume, we question the relevance of building multilayer realistic models such as FEM given the targeted localization precision of a few millimeters[1]. For this particular objective, a simpler model (IHM or OSM) might be sufficient to describe the electrical field propagation within the brain.

The spatial repartition of the sensors greatly differs between classical EEG and the Stereo-EEG setup. In scalp EEG, the sensors are homogeneously covering the scalp, providing a global vision of the brain volume, or at least of the surface of the cortex. Inversely, SEEG electrodes are concentrated within a few regions of interest and are collinear within each multi-sensor electrode. Geometrical considerations impacting the conditioning of the inverse problem are thus to be studied.

While no standard implantation exists for the SEEG setup, the electrodes are nevertheless implanted following a similar scheme from one epileptic patient to another. About ten electrodes are usually implanted in the hemisphere rumored to contain the epileptic zone (called the Ipsi hemisphere), circumscribing the involved structures. To identify possible co-occurring epileptic events in the opposite (Contra) hemisphere, about two to three electrodes are also implanted in this hemisphere. Considering this usual electrode implantation, we analyze, under extensive simulations, the localization performance when using different sets of electrodes and forward modeling. In parallel, the robustness to noise is also evaluated, considering spatially and temporally white noise, as well as spatially correlated noise simulated as dipoles of disturbance. Illustration of the localization performance on real data is presented at the end of the chapter.

[1] All along this thesis we consider a localization result as successful if it lies less than 1cm away from the true source location

3.1 SEEG specifics

The main advantages of SEEG over EEG is that this modality provides a higher signal to noise ratio (SNR). The sensors are inserted deep in the brain, avoiding the skull bone barrier, and are presumably close to the sources of interest. SEEG is also less affected by electromagnetic noise or extra-cerebral artifacts. However, SEEG is a very spatially focused modality and brings a rather local image of the brain, possibly missing some active regions far from the implanted sites. This might be one of the main reasons why SEEG is forsaken when it comes to source localization. However, using common reference montages instead of the usually considered bipolar montage can partially improve the visibility of SEEG.

Since the SEEG sensors are not homogeneously distributed within the head volume (see Figure 3.1), their particular spatial repartition has an impact on the conditioning of the inverse problem, on the identifiability of the source of interest, as well as on the re-referencing problem. We briefly discuss these points in the following paragraphs.

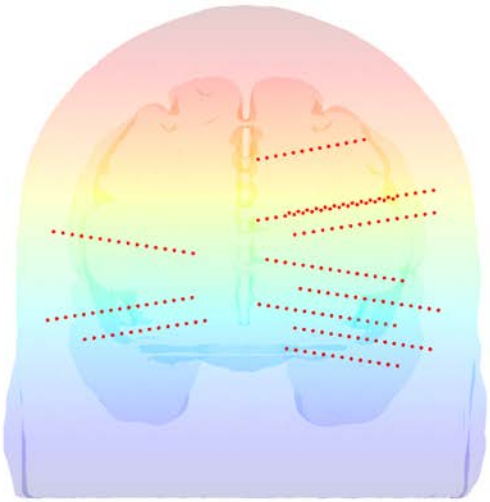

Figure 3.1: Sensor placement in the 3 dimensional head model. The sensors are represented as red dots.

3.1.1 Sensor conditioning

The simplest recording setup uses one multi-contact depth electrode (illustrated in Figure 3.2). The sensors are in this case collinear and the localization problem is undetermined, regardless of the number of available signals. Indeed, the tangential component of the dipole (*i.e.*, orthogonal to the plane determined by the needle and the origin of the dipole) cannot be seen by any of the sensors, thus both the position and amplitude of the dipoles are undetermined (see Figure 3.2). Consequently, at least two multi-contact electrodes are needed. Moreover, they have to be in different planes. Indeed, a symmetrically placed dipole (with respect to a plane) will produce the same potentials on coplanar sensors. Besides, dipoles having their origin in the plane are also undetermined (the orthogonal component is invisible to the sensors). Although this situation is hypothetical, as the electrodes are seldom inserted in the same plane, the noise (*i.e.*, the background activity) can mask the dipole of interest components on sensors situated in a sort of "‘slice"’ of brain tissue, a kind of thicker version of a plane. In simulations, as well as in real situations, we

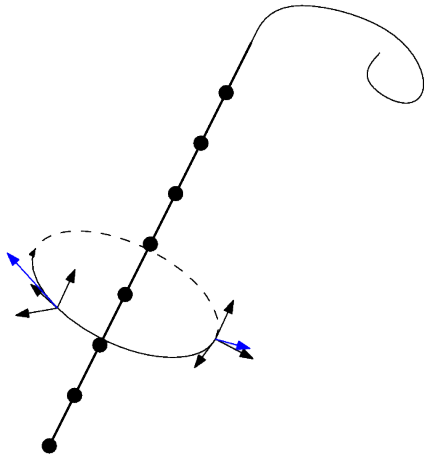

Figure 3.2: Illustrative example of collinear sensors. Two dipoles shown in blue (geometrically – the same vector rotated in different angles around the axis of electrode shaft) would produce identical measurements on the sensors (shown as black dots).

therefore considered a subset of sensors distributed on 3 or more electrodes. When it comes to dipole estimation, the number of unknowns is 6. For this reason, at least 6 sensors are to be considered in the localization process.

3.1.2 Relative source distance to sensors

The advantage of having sensors close to sources has its flaws. The activity of the dominant dipole of interest might be masked on some sensors by the activity of the closest co-occurring dipoles of a smaller amplitude. An illustrative example can be seen in Figure 3.3a. The dipolar source in the middle (numbered 1) has an amplitude 5 times bigger compared to the second weaker dipolar source (numbered 2). Figure 3.3b gives the amplitudes of the recorded potentials on all the sensors (here obtained with an IHM). Sensors have not been sorted in any particular way – they have been added to the plot electrode by electrode and serves for an illustrative purpose. The potentials for the dominant dipole (Φ_1) are given in red and the weaker one (Φ_2) in blue. Computing the global power of the measurements on the sensors caused by each source (as the sum of the squared potentials), the less active source has 1.8 times greater power. This illustrates the possible misinterpretations when analyzing SEEG signals, this drawback will be kept in mind in the following sections as well as in the chapter 4.

3.2 Head model

The construction of the forward problem is a key step toward reliable localization procedures. We propose to evaluate the most adequate propagation model that is to be used in this context of SEEG sensors. In this objective, we compared two analytical models (IHM and OSM) to a numerical model computed based on FEM, considered in this thesis as the ground truth.

3.2.1 Reference model: FEM

The most elaborate approach, considered here as an accurate approximation of the real electrical field propagation, is proposed by Finite Element Method model (FEM), which aims to model as close as possible to the real individual anatomy and the conductivity properties of the head tissues [Hofmanis 2013]. FEM are able to treat irregular shapes,

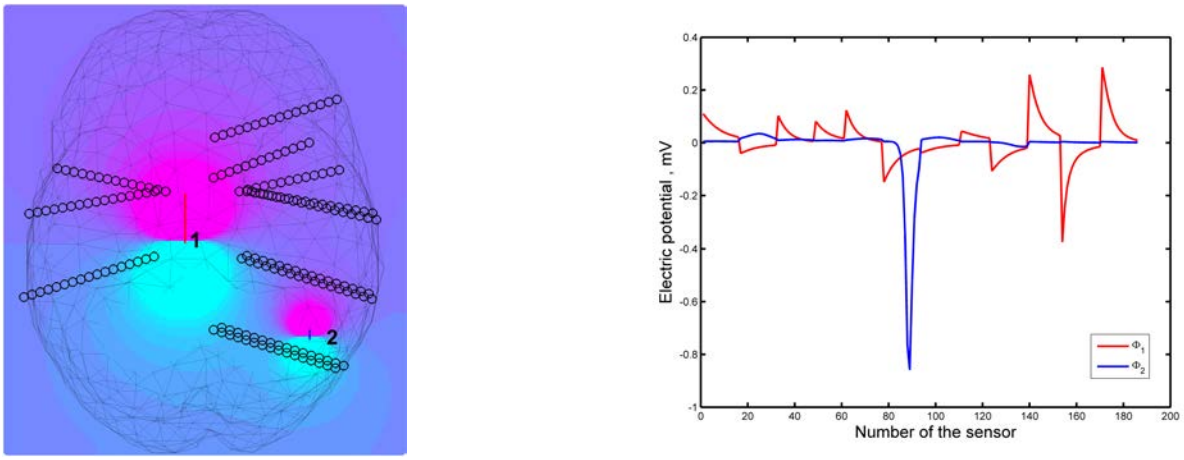

(a) **(b)**

Figure 3.3: Illustrative bad case of a perturbation source close to the sensors. a) Two sources with different distances to the closest enclosing sensors are shown. The leftmost has higher amplitude, but is situated further from sensors. The rightmost has lower amplitude but it is situated closer to the sensors. b) Potentials on different sensors (number of sensor on X axis) from dipoles shown in a.

extracted from imaging techniques, as well as inhomogeneous and anisotropic environments, by assigning different conductivity values to each matter (tissues), as well as for each direction in the anisotropic case.

For our simulations, in this thesis we use the non-linear MNI-ICBM152 atlas [Fonov et al. 2011], which is an MRI volume obtained by averaging 152 individuals (shown in Figure 3.4). This model comes with five segmented compartments: gray matter, white matter, cerebro-spinal fluid (CSL), bone and scalp. These segmented areas are meshed, providing a geometric discretization on which a finite element method can be applied. The shortest edge of the resulting mesh is 0.71 mm and the longest one is 6.32 mm [1]. The number of resulting tetrahedrons was 1272212, for a number of node points (DoF) of 218165.

The electrode implantation in the brain volume mimics the usual implantation scheme adopted at the CHRU of Nancy. It consists of 12 electrodes, 9 in the right hemisphere and 3 in the left hemisphere, each electrode containing from 12 up to 16 sensors ($N_c = 186$ sensors are inserted in total). Representation of this implantation is shown in Figure 3.5

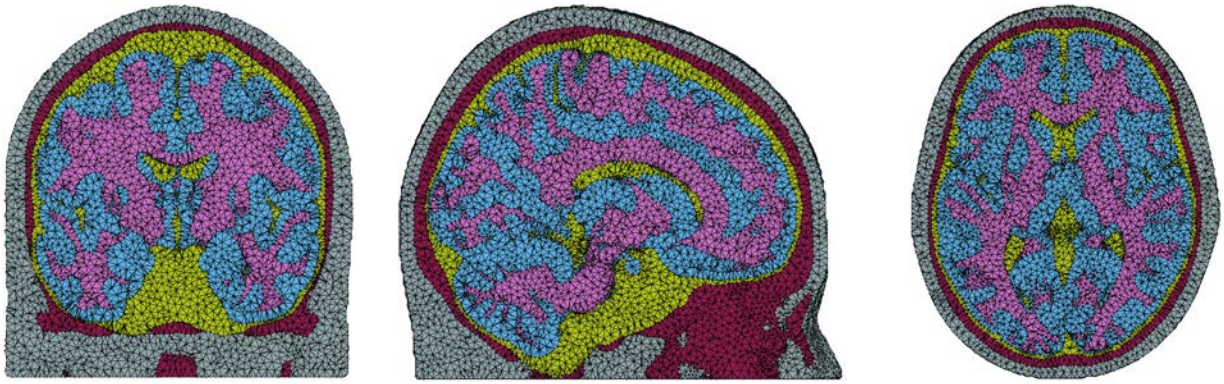

(a) Front view **(b)** Side view **(c)** Top view

Figure 3.4: MNI-ICBM152 atlas MRI image. Different tissue meshes marked in different colors.

[1] We have to mention that the mesh used in all the figures in this thesis is a coarse version of the mesh used in simulations.

In our study, constant conductivities were chosen for a given tissue, regardless of the orientation ($0.33S/m$ for the gray matter, $0.2S/m$ for the white matter, $0.33S/m$ for the scalp and $0.004S/m$ for the skull bones [Geddes and Baker 1967]). A discretized version of the Poisson equation was used to compute the potentials in every point of the mesh and/or for every electrode (see [Hofmanis 2013, Vallaghé 2008] for a detailed description). Following [von Ellenrieder et al. 2012b], we have chosen to approximate the SEEG contacts by their central points, as the influence of the electrode dimension on the localization was proven to be very limited.

To calculate potentials at exact SEEG sensor positions, two approaches can be used: 1) adding SEEG sensor central point coordinates to the mesh points; 2) interpolating the potential measurements at sensor positions using the potentials computed in the close surrounding points. Since the mesh is rather detailed in our case, we have retained the second approach.

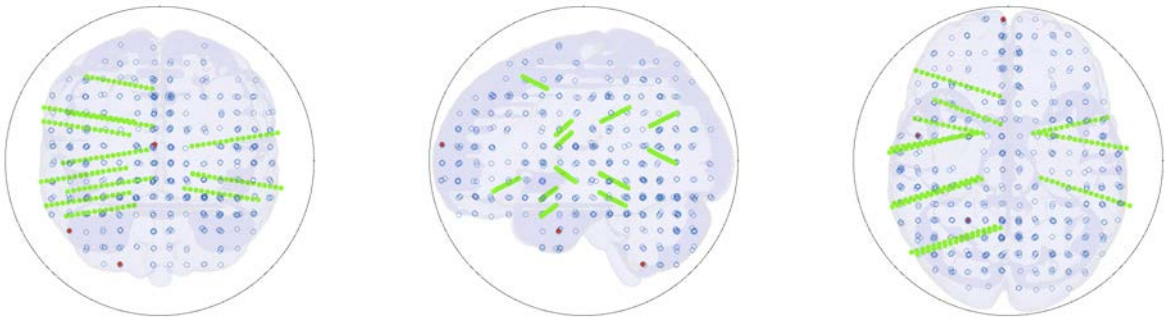

(a) **(b)** **(c)**

Figure 3.5: Simulation setup representation. 509 tested dipoles in blue and intra-cerebral EEG sensors in green. The sphere fitted to the brain mesh is shown in black.

On a modern PC, the complete FEM computation time in Matlab for one dipole is about 10s.

3.2.2 Analytical models

While the accuracy of the forward model has proven to be higher in numerical models compared to analytical ones, the choice of the forward model to be used for solving the inverse problem is not obvious. Numerical models require precise anatomical information obtained from medical imaging, and multiple steps of data registering and segmentation processes must be carried out. The optimization in the ECD localization approach implies repeated computation of the forward model at each iteration. Therefore, calculation time plays an important role.

Recent works of the ESPaCE team comparing multiple forward models based on recordings of Intra Cranial Stimulations (ICS) in [Hofmanis 2013] revealed that a spherical model shows a consistent performance compared to numeric models. Only in close to skull stimulations the performance is reported to be noticeably worse than when numerical models are used.

In a recent study by G. Birot *et al.* [Birot et al. 2014], the authors compared the localization accuracy when using a spherical model compared to BEM and FEM model. They found out that in clinical applications, the use of sophisticated numerical head models is not a crucial factor for an accurate localization. Very similar performances were found between these models. According to the authors, this is due to the uncertainties in the brain tissue

segmentation, in the conductivities affected to these tissues, as well as to the presence of noise. This conclusion may be even more relevant in the context of intracerebral measurements where the sensors are close to the sources.

Simplistic analytical models have very few parameters compared to numerical models, and are straightforward to compute. In IHM model, the conductivity σ is the sole parameter. The inverse problem being linear in this parameter, it will only influence the estimation of the source amplitude, but not its location. We are using the value of $0.3S/m$, as suggested in the literature [Cosandier-Rimélé et al. 2007].

OSM model requires to fit a sphere on the brain volume, as explained in Subsection 2.2.2.1. In our simulations, the sphere is fitted to enclose all the vertices of the inner skull mesh. The radius of the fitted sphere is $86.6mm$. Conductivity of the inner sphere medium is also fixed at $0.3S/m$.

3.2.3 Model comparisons

The comparisons of the forward solutions based on the two analytic models (IHM and OSM) with the one provided by the FEM model are carried out considering three examples of source placements: the source $S1$ is placed in the hippocampus, the source $S2$ is placed in a gyrus in the intermediary structures and the source $S3$ is located on the brain surface near the skull. For each of these three placements, the three orthogonal orientations (Ox, Oy, Oz) are considered in order to evaluate the influence of the tissue limits and of the skull border considering each possible orientation components. The electrical fields generated by these three dipoles (thus nine configurations) are computed on each vertex of the head volume mesh using the three considered propagation models. Maps of difference are then computed between IHM and FEM as well as between the OSM and FEM, using the following error measurement:

$$\Phi_e = |\Phi_{FEM} - \Phi_a| / \Phi_{FEM} \tag{3.1}$$

Φ_a being the potential values computed either using IHM or the OSM.

We compare the two analytical models with the realistic FEM using the error defined in (3.1). The propagation using the FEM model is given for the three dipoles on Figure 3.6. The colors (corresponding to potential values) on this figure are saturated at 10% of the potential computed by the IHM at a 5mm distance of the dipole origin, in the direction of the dipole. This value is very similar to the one given by the FEM (see Figure 3.7) and it was chosen in order to have a similar color code regardless of the position and of the orientation of the dipole. Saturating the image allows to highlight (in dark red/blue) the brain volumes where the potentials have important magnitudes and thus where the comparison with the analytical models is relevant (the error of the analytical models should be small). Outside this area, we can observe the decrease of the potential, roughly with the square of the distance [Zaveri et al. 2009], yielding small potential values (10% of the saturation value, *i.e.*, 100 times smaller than the potential at 5 mm from the dipole, green color) at about 5 cm from the origin of the dipole.

The error Φ_e is illustrated on brain slices in the dipole plane. The results for the three dipoles $S1$, $S2$, $S3$ are provided in the Figure 3.7. For the sake of visualization, the error value is saturated to 1: dark red areas indicate errors of more than 100% with respect to the FEM model.

From the error maps of the profound dipole $S1$, we can see that both the OSM and the IHM models provide satisfactory approximations of the realistic FEM model in the middle of the brain volume, at least near the dipole placement, with a not significant enough of an advantage for the OSM. In this area most of the SEEG sensors are

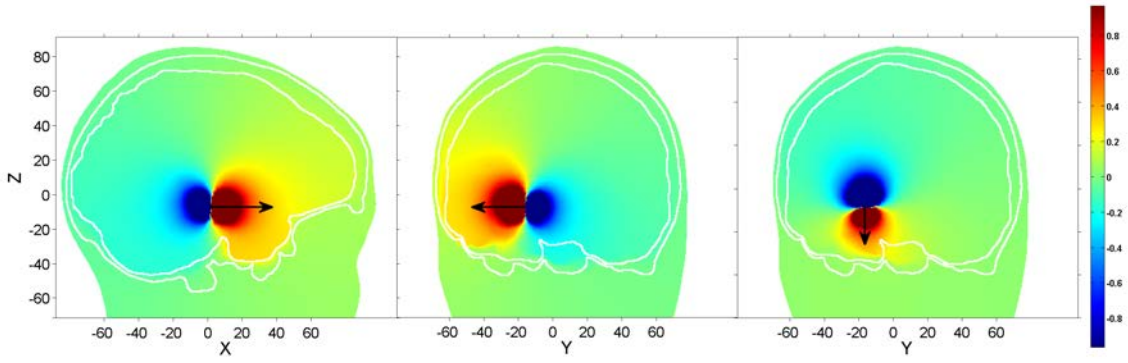

(a) Profound dipole $S1$

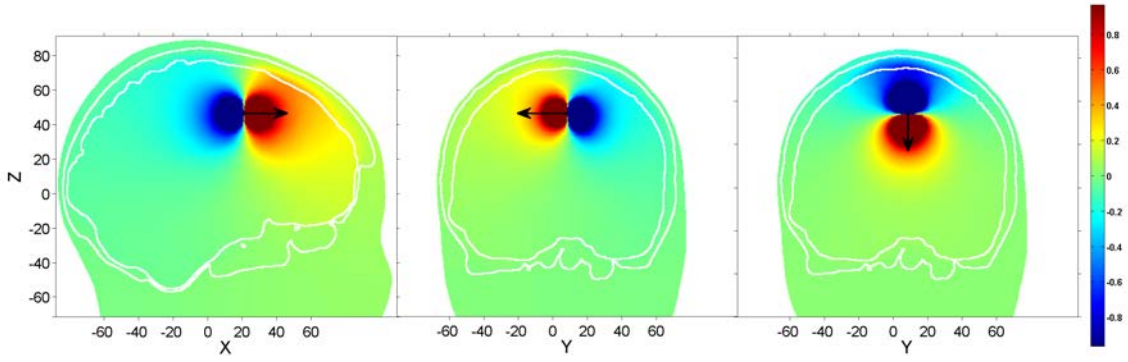

(b) Intermediary dipole $S2$

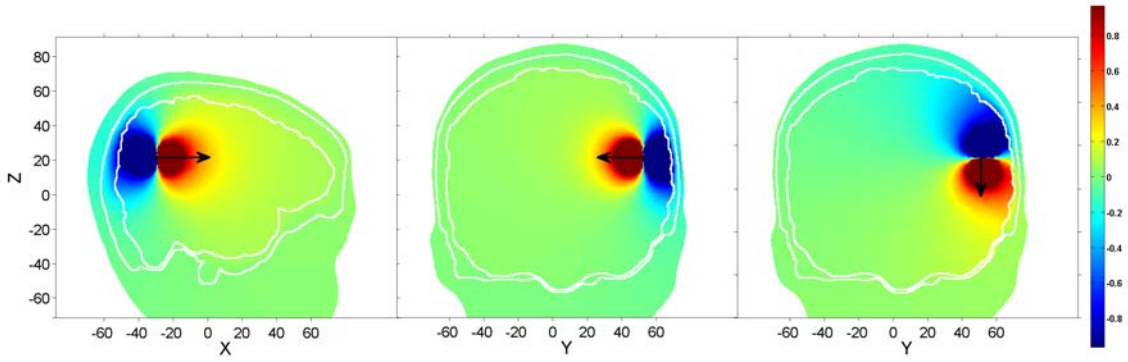

(c) Superficial dipole $S3$

Figure 3.6: Three tested dipoles for forward problem using FEM. All orientations (Ox, Oy, Oz, from left to right). The dipoles are represented as a thin black arrow. Axes units: mm. The planes to display the potentials were chosen in order to represent the situation as clearly as possible.

concentrated, thus being a first positive argument toward a localization procedure based on these simple models. It should be noted that high errors are encountered in the vicinity of the plane orthogonal to the dipoles, the electrical field values being very close to zero in this area, regardless of the model. Also, when interpreting these maps, one must have in mind that high relative errors encountered far from the dipole are rather irrelevant, because the electrical field is also very close to zero regardless of the model.

The results for the two other dipoles confirm the previous analysis, even if they show slightly less advantages for the OSM: for some positions and orientations, the IHM seems to provide better approximations of the electrical potentials in deep structures, while the OSM looks more accurate near the skull border, if the sphere is correctly fitted (see dipole $S3$, placed near the skull border). Globally, both models are similar enough not to eliminate either of

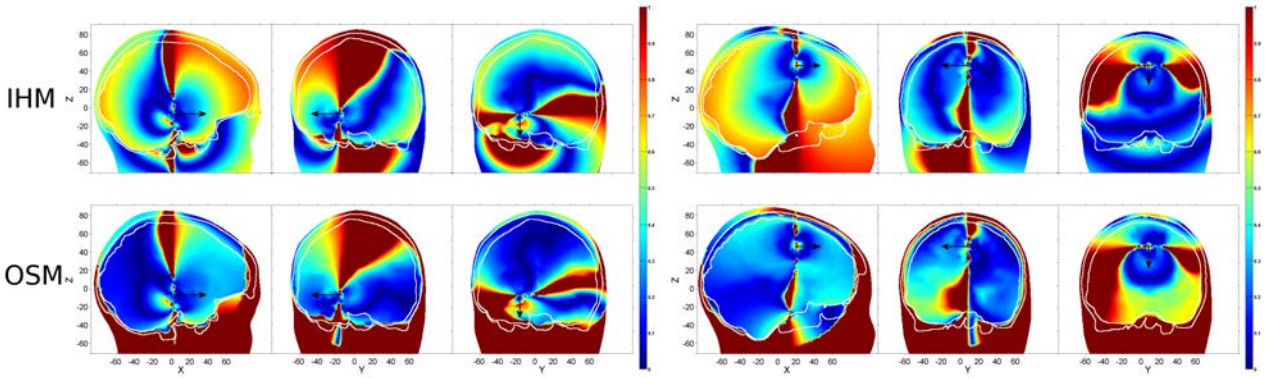

(a) Profound dipole $S1$ **(b)** Intermediary dipole $S2$

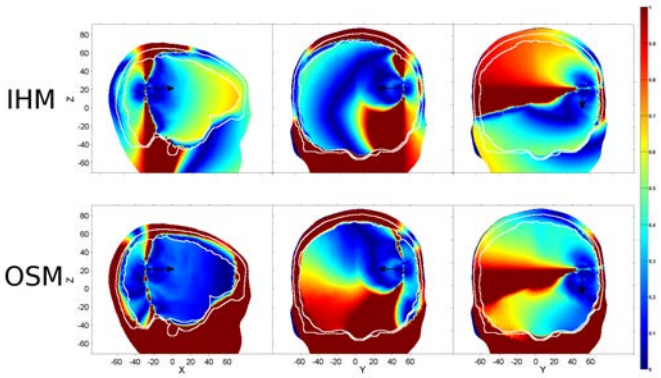

(c) Superficial dipole $S3$

Figure 3.7: Difference maps for the three dipoles $S1$, $S2$, $S3$. For each subfigure, the first row illustrates the difference IHM vs FEM, while the second one the difference OSM vs FEM. From left to right, the three standard orientations of the dipoles, represented as thin black arrows: Ox, Oy, Oz. Axes units: mm.

them at this stage of analysis.

From these observations, we expect reasonably good localization performances using these simple analytical models, in particular when considering deep and intermediate sources as well as sensor placements, the estimation of the potential near the skull border being the main weakness of these models. The preliminary conclusions made here have to be tempered by the fact that the references we used, namely the FEM model, still remain an approximation of the propagated field, and also include their own modeling errors. This evaluation simply points out that we can be as confident in analytical models as in FEM when considering particular areas in the middle and in deep brain volume, such areas coinciding with most of the SEEG sensor positions.

3.3 ECD approach and simulation setup

3.3.1 ECD approach

The ECD inversion is carried out using a moving dipole approach. A non-linear optimization algorithm is required to estimate the six parameters of the dipole. Two non-linear optimization methods have been tested, a Simplex method as well as SQP (Sequential Quadratic Programming) method. SQP was finally chosen due to the ease of constraints implementation and its ability to integrate different levels of sensitivity on the estimation of each parameter (*e.g.*, the objective function (eq. 2.13) is less sensitive to position shift than to orientation shift). The algorithm is constrained

to produce solutions in the sphere (for both IHM and OSM forward models).

To deal with multiple possible local minima, a **multistart** approach has been adopted (see Subsection 2.3.2.1). Each localization problem was solved using 20 different initialization points. In this chapter, the dipole among the 20 with the best goodness of fit was chosen as the final solution. The choice of an adequate starting point is a sensitive issue and depends on the specifics of the problem. The simplest approach would be to randomly choose 20 points in the volume and start the localization algorithm from these respective points. However, better results should be obtained when having the initial starting points homogeneously distributed in the brain volume, avoiding uncovered head regions.

Solving this homogeneous spatial distribution problem is by itself a non-trivial optimization task: where should the centers of N identical spheres be placed (regions *a priori* covered by every initialization point) *inside* a bigger sphere (the OSM fitted model) such as filling as much of its volume as possible? The solution we propose in this thesis is suboptimal but fast, and it is inspired by another related problem: how can we uniformly place a set of N points *on the surface* of a sphere. A solution of this last problem is obtained my minimizing the Riesz' s—energy:

$$E_R = \sum_{i=1}^{N} \sum_{j=i+1}^{N} \frac{1}{\|\boldsymbol{r}_i - \boldsymbol{r}_j\|^s} \tag{3.2}$$

where $\boldsymbol{r}_i$, $\boldsymbol{r}_j$ are the 3D positions of points i and j and $\frac{1}{\|\boldsymbol{r}_i - \boldsymbol{r}_j\|^s}$ can be interpreted as a potential energy of repulsion between electrically charged particles i and j. The exponent s parametrizes the influence that particles have one upon another (a small value accounts more for far away particles while a big value indicates a more local interaction between them. For example, for $s = 1$, one can recognize the Thompson problem of distributing electrical point charges (Coulomb model) (*e.g.*, [* 2016, Kuijlaars and Saff 1998]).

Still, inside a volume, the problem is much more difficult[1] and we propose a simple heuristic:

1. choose the number N of initialization points inside the OSM sphere of radius R, fitted on the brain mesh
2. compute the radius of a sphere having a volume N times smaller than the OSM sphere, $R_p = R/\sqrt[3]{N}$
3. define a smaller sphere, included in the OSM one, with a radius $R_1 = R - R_p$ and randomly generate N positions $\boldsymbol{r}_i$ inside
4. compute the positions $\boldsymbol{r}_i$ minimizing the Riesz' s—energy (3.2) of the N points, under the constraint $\|\boldsymbol{r}_i\| < R_1$

The results of this procedure are illustrated in Figure 3.8a for $N = 20$ and $s = 4$. For smaller s and the same $N = 20$, the points simply distribute on the surface of the sphere of radius R_1; for bigger N on the other hand, they also place themselves inside the sphere volume, as, for example, illustrated by $N = 40$ and $s = 2$ Figure 3.8b. For $N = 40$ similar results are obtained for larger s values.

3.3.2 Simulation setup and parametrization

Our simulations are based on the MNI-ICBM152 averaged MRI and the SEEG sensor implantation introduced in Section 3.2. We wish to analyze the identifiability of any possible source placement in the whole head volume, more

[1] This problem can be traced back to Kepler, who conjectured over the optimal positioning of a set of identical spheres inside a volume and to the kissing spheres problem of Newton (how many spheres can we place tangent to another given identical sphere). The two problems were solved respectively by Hales (1998) and by Schüte and van der Waerden (1953) [* 2016, Hayes 2013].

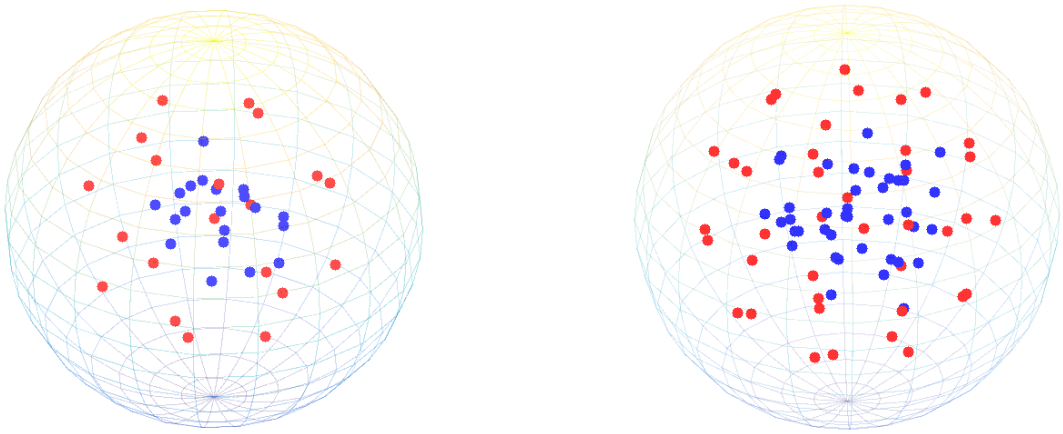

(a) $N = 20$ **(b)** $N = 40$

Figure 3.8: Illustration of initialization point optimization. Random starting points on the grid in blue; points found by minimizing Riesz s—energy in red. N is the number of points.

precisely, in the gray matter volume which is the seat of the brain activities. We sample source positions over the mesh of the gray matter with a resolution of $9mm$, yielding 509 source positions. For each position, the three Cartesian orientations $(0x, 0y, 0z)$ are considered. Each dipole with a unitary amplitude is projected separately on the sensors using the FEM model described in Section 3.2.1, and localized using the method described in Section 3.3.1 using either the IHM or the OSM for the forward model computation. In the no noise case, we then have $3 \times 509 = 1527$ localization problems to solve. The resulting localization performance, measured as the Euclidean norm between the actual source position and the position of the estimated dipole (localization error) will help us in evaluating the ability of a simple analytical model to invert a realistic FEM model, and to validate the hypothesis that such modeling might be sufficient to localize brain sources from SEEG.

We also evaluate the robustness to noise. Two types of noise are added to the data, to begin with, spatially and temporally white noise, simulating the presence of background noise on the sensors. For a more realistic setup, simulating the presence of co-occurring brain activities of more significant amplitudes (nevertheless leaving the source to localize as the dominant dipole), the projection of 5 dipoles of disturbance, randomly picked among the 509 dipole positions, and added to the measurements (eliminating the sources that are closer than 4 mm to any of sensors to avoid a strong masking effect). For both types of noise, 100 realizations with four different noise levels (as defined later in this thesis – see Subsection 3.4.2) are simulated and added to the projections of the 3×509 dominant dipole configurations separately, yielding the $3 \times 509 \times 4 \times 100 = 610800$ inverse problems to be solved for each type of noise.

Given the realistic SEEG implantation described earlier, we evaluate the localization performance when using four different sets of sensors. The first set is composed of the six biggest absolute potentials among the $N_c = 186$ recorded potentials (considering the constraints of a sensor repartition over at least 3 electrodes, see Subsection 3.1.1). We would like to evaluate if such a limited subset of sensors might be sufficient for estimating the 6 unknowns of the dipole to localize. We then evaluate the localization accuracy considering the set of electrodes either in the left or in the right hemisphere. Depending on the location of the localizable source, each subset can stand either as the ipsi-lateral set of sensors or the contra-lateral set of sensors. The objective of this analysis is to evaluate if a dipole can still be identified even if the electrodes have been mis-implanted (in the contra-hemisphere), and if the number of

used sensors has an influence on the localization accuracy (the left hemisphere contains 47 sensors over 3 electrodes while the right hemisphere contains 139 sensors over 9 electrodes). Finally, we also evaluate the localization accuracy when using the whole set of sensors, addressing the question of whether using as many measurements as possible always provides better localization results.

3.4 Simulation results

3.4.1 No noise scenario

To evaluate the feasibility of the localization in an ideal environment, we analyze the results when no noise is added to the measurements. Localization errors will mainly be due to two factors in this situation. The first factor of error is the approximation in the forward model, *i.e.*, to the difference between the FEM model with, respectively, the IHM and the OSM model. This will help us in validating the relevancy of using an analytical model in the context of SEEG. The second factor of error is the sensor setup used for the localization, giving the first clue on the ideal subset of sensors that should be used for reliable source localization. It is worth noticing that these two factors are obviously not independent, as the localization result depends on the accurate reconstruction of the potential at the positions of the recruited sensors, *i.e.*, on the quality of the forward model.

In Figure 3.9, boxplots of localization errors when using either IHM (Figure 3.9a) or OSM (Figure 3.9b) to compute the forward model are given for each of the four sets of sensors introduced in Subsection 3.3.2. The right and left hemispheres have an unbalanced number of implanted sensors (139 vs 47 sensors), the localization results of the dipoles positioned in these respective hemispheres are analyzed separately. $6L$ (respectively $6R$) then designates the localization errors of the dipoles positioned in the left hemisphere (respectively the right hemisphere) when the 6 sensors with the biggest potentials are recruited (6-sensors configuration). IL and IR designates the localization errors when using the sensors in the hemisphere of the localizable dipole (the Ipsi hemisphere, left and right respectively). The same for CL and CR, where C stands for contra-hemisphere. Finally AL and AR designate the All configuration in which the whole set of 186 sensors are used, when the dipole to localize is, thus, in the left and right hemisphere. The medians of the localization errors are reported in the Table 3.1, also showing the results for the three Cartesian orientations separately, in order to evaluate the disparity of the localization performance depending on the dipole orientation.

The first immediate conclusion is that the OSM outperforms the IHM in every of the eight studied sub-configurations, with comfortable margins visible with bare eyes. In particular, the OSM is consistently about two times more accurate in median than the IHM over the all and ipsi-lateral configurations. It means that considering the effect of the skull bone conductivity barrier is of first importance. This aspect is illustrated in Figure 3.10. As can be seen, almost all of the 509 dipole positions can be localized using one of the sensor configurations when using the OSM, while only about 70% are in the same situation for IHM inversions. Besides, in both cases, the well localized dipoles (left extremity of each figure) are also close to the center, but the OSM only badly localized the dipoles situated very close to the brain frontier, while the IHM errors also appear for dipoles much closer to the center, at intermediate depths.

In the case of the **6-sensors configuration**, the medians of the localization errors (see Table 3.1) are high, close to or over 3cm in all cases of dipole orientations, hemisphere location, and for both IHM and OSM. We might conclude that given the inherent imprecision of the propagation model used to build the forward model, restricting the number

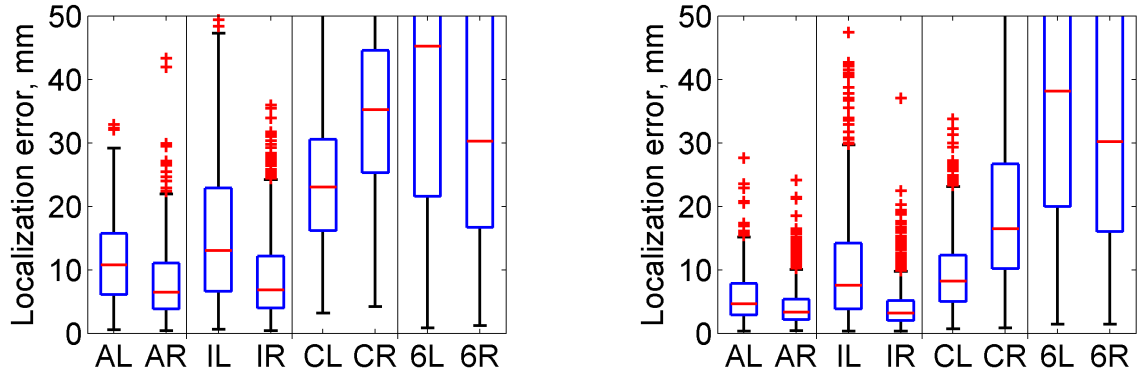

(a) IHM **(b)** OSM

Figure 3.9: Position errors (in mm) for the 509 dipoles as a function of the employed model (IHM and OSM), sensor configuration and hemisphere (the indexes l and r indicate median errors computed over the left and right hemisphere respectively), all three orientations considered, no noise added.

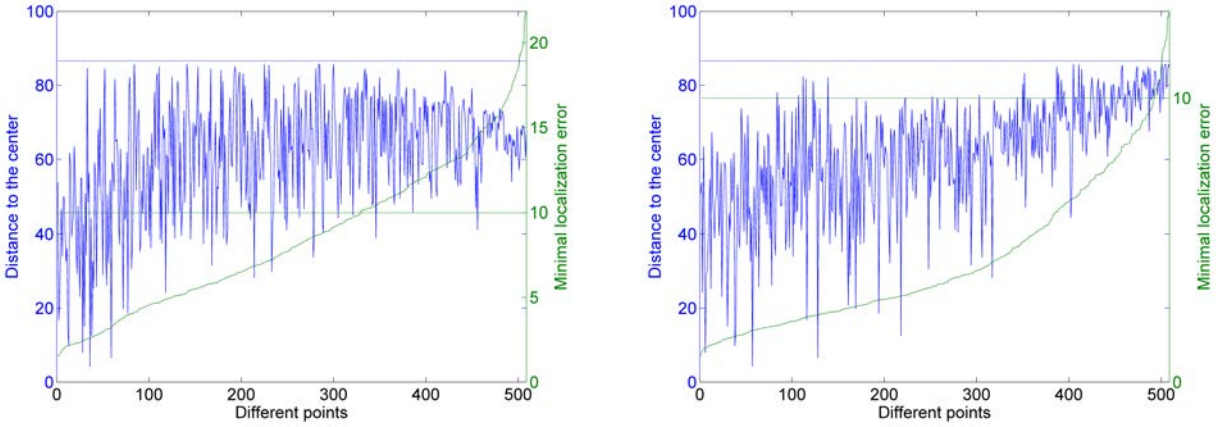

(a) IHM **(b)** OSM

Figure 3.10: All 509 dipoles sorted ascending by their minimal localization error (in green) and their respective position from the center of the sphere (in blue) in the case of an IHM model (a) and an OSM model (b). Sphere radius is indicated in a horizontal blue line and the accepted error for localization is indicated in a horizontal green line.

of used sensors to six cannot provide reliable results. The boxplots in Figure 3.9 show that a high localization disparity is obtained for this sensor configuration, which suggests that the relative position of the chosen sensors with respect to the dipole to be localized might be very critical. It raises the question of a wiser sensor subset selection.

The localization performances for the **ipsilateral** sensor's configuration are confident when using the OSM inversion, clearly better than the IHM. The dipoles situated in the right hemisphere, containing 9 electrodes (*i.e.* 139 sensors), are better localized than those in the left hemisphere, implanted with 3 electrodes only (47 sensors). Indeed, the mean localization errors are under 3.5mm at the right, and over 6mm at the left, all orientations considered. However, the results are still satisfactory for both hemispheres (with respect to the clinical precision rule of $1cm$ adopted in this thesis), suggesting that a limited number of sensors might be sufficient.

The results obtained using the **contralateral** sensor configuration clearly point out that, in this ideal no noise case, satisfactory localization performance of a contralateral dipole can be obtained when enough electrodes are implanted in the opposite hemisphere. Indeed, when an OSM model is considered, the mean error over the three directions is

under 10mm for the dipoles located in the left part of the brain, thus localized using the 9 electrodes implanted in the right hemisphere. On the other hand, when a limited number of electrodes is available, the localization performance decreases quickly: the mean error value is over 20mm when the dipoles of the right hemisphere are localized using the three electrodes of the left hemisphere, and a high disparity can be observed on the boxplots of Figure 3.9. Ipsi-lateral configurations clearly provide better localization results than contra-lateral configurations. This confirms the observations drawn in Subsection 3.2.3 pointing out the adequacy of the analytical model with the realistic FEM in the vicinity of the dipole, up to about $3cm$ away from the dipole. When far sensors are used, errors in the model highly impact the localization precision.

As expected in this ideal case, the **all** sensors configuration gives very confident results. From the Table 3.1, it can be observed that the localization error is around 4mm on average for the one sphere model, while it goes from 6 to 8mm for the IHM. This confirms the superior modeling power of OSM over IHM. It has to be noted that the results are better for the dipoles that are placed in the more implanted (right) hemisphere (median errors below 4mm, and consistently over this value at the left, whatever the orientation). From the boxplots (Figure 3.9), it can be seen that the error disparity is rather small, a few number of outliers being over the 1cm threshold for the right hemisphere, and the third quartile being below 1cm error in the left hemisphere. Also, it is important to notice that these right hemisphere dipoles are slightly better localized using the ipsilateral-sensors configuration in every one of the three orientations. This observation seems to indicate that using a sufficient amount of close sensors is better than using all available sensors, even when no noise is present.

	All			**Ipsi**			**Contra**			**6**		
	ϵ_p	$\epsilon_{p,left}$	$\epsilon_{p,right}$	ϵ_p	$\epsilon_{p,left}$	$\epsilon_{p,right}$	ϵ_p	$\epsilon_{p,left}$	$\epsilon_{p,right}$	ϵ_p	$\epsilon_{p,left}$	$\epsilon_{p,right}$
IHM Ox	8.0	11.1	6.3	9.2	15.4	6.7	28.1	22.7	35	36.2	45.2	32.3
IHM Oy	7.5	11.2	5.8	8.5	11.7	6.1	27.9	23.1	35.4	37.5	44.9	28.6
IHM Oz	8.9	10.1	7.9	10.2	13.3	8.2	29.5	23.7	35.8	36.1	45.9	28.6
OSM Ox	4.5	5.3	3.3	4.8	7.6	3.3	9.1	7.7	10.5	33.1	37.5	30.74
OSM Oy	3.7	4.1	3.2	4.5	8.0	3.2	12.7	7.8	20.1	33.4	39	30.2
OSM Oz	3.8	4.6	3.4	4.1	7.2	2.9	15.2	9.1	23.7	34	38.4	27.5

Table 3.1: Median position errors (in mm) for the 509 dipoles equally distributed in the gray matter as a function of the employed model, dipole orientation, sensor configuration and hemisphere (the indices l and r indicate median errors computed over the left, respectively right hemisphere

It is interesting to briefly analyze the obtained goodness-of-fit's for the different evaluated sensor configurations, dipole orientation and head model. Indeed, as mentioned previously, the localization results are obtained by maximizing the GOF (see chapter 2, equations 2.13 and 2.15) and using a multi-start procedure. We will not detail here all the median GOFs for all possible situations, but we will 'shrink' table 3.1 by averaging the associated GOFs between the 3 directions Ox, Oy, Oz before computing the medians over the 509 dipoles. The results are given table 3.2.

As it can be seen, all values are very high, which is somehow expected for the no-noise situation (only few dipoles are affected by model errors, more for IHM than for OSM, see also the discussion above). But, if one would have to choose between the results based on the GOF only, the most performant solutions should be given by the **6** sensors configuration, which has the highest GOFs among all. This is not completely surprising, as it is obviously easier to fit a model on less data. Indeed, when looking at the values, one can observe that the **all** configuration has the lowest GOFs, although in principle the best localization errors, while the **ipsilateral** configuration, sometimes superior to

	OSM			IHM		
	GOF	GOF_l	GOF_r	GOF	GOF_l	GOF_r
All	0.995	0.995	0.994	0.987	0.988	0.985
Ipsi	0.997	0.998	0.996	0.994	0.997	0.989
Contra	0.998	0.998	0.999	0.993	0.991	0.995
6	0.999	0.999	0.999	0.999	0.999	0.999

Table 3.2: Median GOFs for the 509 dipoles equally distributed in the gray matter as a function of the employed model, sensor configuration and hemisphere (the indices l and r indicate values computed over the left, respectively right hemisphere. For each dipole, the GOFs of the 3 orientations were averaged before computing the medians

all and always using less sensors, has higher GOFs (but lower than the **6** sensors configuration). These observations raise the question of the reliability of the GOF maximization for the source localization problem, especially when only some subsets of sensors are used in the optimization process. This issue will be largely discussed in the next chapter.

Figure 3.11 illustrates the mean OSM-based localization errors (over the orientations Ox,Oy,Oz) for each sensor configuration, for 8 brain slices (transversal planes yOz). The position errors for the dipoles are given using a discrete color code (see legend). Cold (dark blue) color corresponds to a good localization, while warmer (light blue, yellow and red) colors correspond to imprecise ones (see legend in the caption of the figure). Inaccurate localization maps are produced in the contra-lateral configurations (3^{rd} column), while red points are dominating the 6-sensor maps (last column). We then definitively put aside these two sensor configurations. The vast majority of the badly localized dipoles under the all-sensors configuration (left column) are located very near to the brain's outer limits. This fact is further illustrated in Figure 3.12 in 3D transparency. The encircled points are the source positions yielding localization error over $10mm$ no matter the orientation of the dipole and the used set of sensors. This remark is concordant with the considerations given in Subsection 3.2.3 on the limitations of a rough sphere to shape such irregular skull borders. The maps for the right hemisphere in the Ipsi case (second column) are very similar to that of the all-sensors configuration, but worsening in the left one with more light blue ($[1-2)$cm errors) and yellow $[2-3)$cm errors) points constellating the border of the head.

The contra-lateral configurations coupled with the OSM, indeed do yield reasonably good localization results under the centimeter for the dipoles lying in the left hemisphere, *i.e.*, using the well implanted hemisphere for the localization (139 sensors). However, such performances are obtained in the context of ideal measurements with no added noise. Such configurations do not seem reliable enough in more realistic, noisy, situations, a fact that was indeed observed from our simulations. We have thus decided to discard such configurations from our analysis, and we might already conclude that a confident localization of a dominant brain source is not feasible if the hemisphere containing this source is not implanted with electrodes. The 6-sensors configuration brings bad results and cannot be considered. We then restrain further analysis in this chapter to the ipsi-lateral and all configurations and we address the robustness of ECD localization in a noisy context.

3.4.2 Robustness to noise

Two kinds of noises are simulated. First, spatially and temporally Gaussian white noise is added to the data, simulating inherent background brain activities recorded by the sensors in their close vicinity. A second noisy environment is proposed to create a more realistic simulation setup, in which coherent (spatially colored) noise is added to the data by projecting dipoles of disturbance on the sensors. These dipoles have a lower amplitude than this of the dipole

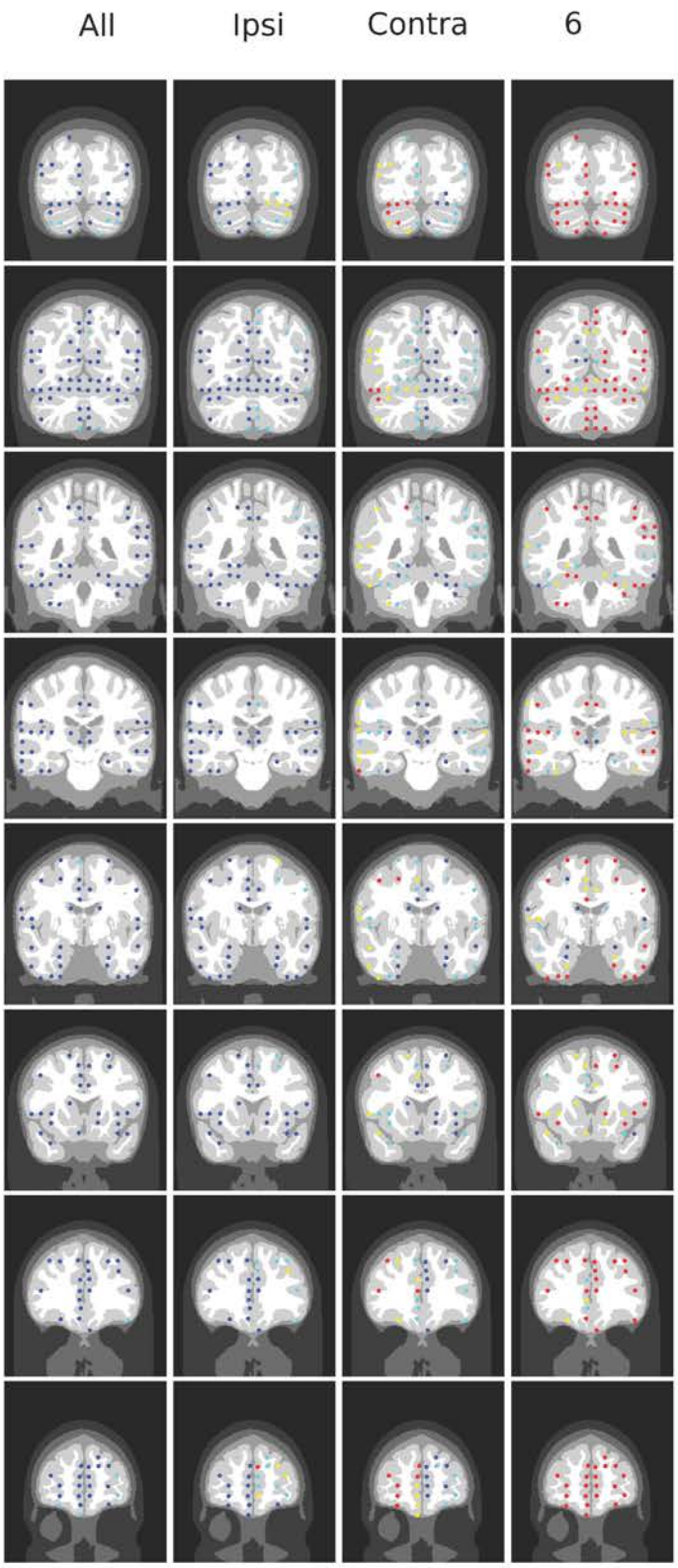

Figure 3.11: Comparison between localization results using different sensor subsets (all sensors, ipsi-lateral sensors, contra-lateral, six biggest absolute values in respective columns from left to right). Simulations used an analytical OSM model for 509 different dipoles (8 out of 17 slices are shown) averaged for each point along three orthogonal directions (no noise case). Error levels for every dipole are coded by colors: • $\varepsilon_p \in [0,1]$ cm, • $\varepsilon_p \in (1,2]$ cm, • $\varepsilon_p \in (2,3]$ cm, • $\varepsilon_p > 3$ cm

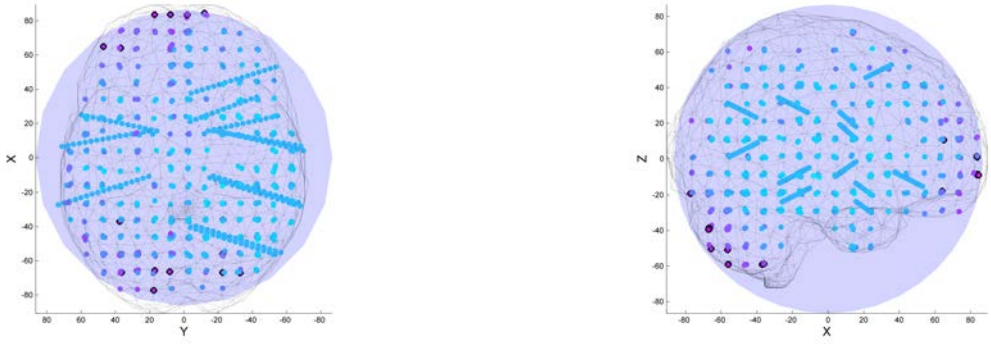

(a) **(b)**

Figure 3.12: Always badly localized source positions, top (a) and side(b) view. Encircled points are always localized with at least 10 mm position error.

of interest, satisfying the hypothesis of a dominant dipole adopted in this thesis. If such requirements seem too optimistic indeed when facing raw SEEG data, it must be noted that efficient pre-processing steps are to be applied before addressing the localization problem, enhancing the Signal to Noise Ratio (SNR) of the activity of interest.

With the objective of performance evaluation as realistic as possible, we adopt a definition of noise level configurations based on a unique noise level reference, whatever the position of the localizable dipole, and of its projection power on the electrodes. This reference is given as the average power of 3×509 unitary dipole projections on the sensors, positioned in the 509 positions defined above and considering all 3 Cartesian orientations:

$$P_{avg} = \frac{1}{3N_sN_c} \sum_i \sum_l \sum_m \phi(j_i^l)_m^2 \tag{3.3}$$

where $\phi(j_i^l)_m$ is the potential on the sensor $m \in 1...N_c$ caused by the source $i \in 1...N_s$ with orientation $l \in \{0x, 0y, 0z\}$).

The noise power is defined based on this average power reference. Considering the addition of white i.i.d Gaussian noise to the data, its standard-deviation is then determined as follows:

$$\sigma_n^2 = \frac{P_{avg}}{10^{L_{SNR}/10}} \tag{3.4}$$

with L_{SNR} the desired SNR in dB, taking values in the set $\{20dB, 10dB, 3dB, 0dB\}$. $0dB$ means that the averaged noise power on the electrodes is the same than this of the averaged projection power of all the unitary dipoles on the electrodes. While this might be a favorable context for few dipoles surrounded by close sensors, this noise level is likely to be very severe for most of the dipoles. On the other hand the $20dB$ SNR models a level of noise where the dipole of interest is dominant, presumably obtained from a successful preliminary denoising step. However, keeping in mind the rapid decrease of the dipole projection roughly proportional to the inverse square of the source-to-sensor distance, this might already represent a strong noise level for dipoles far from any electrodes. These dipoles being typically those near the skull borders where the uncertainties on the forward model are the most important, we expect to lose the identifiability of some dipoles in these areas even for such a seemingly favorable noise level.

The modus operandi is quite different when considering the addition of colored noise on the data. The addition of 5 dipoles of disturbance is simulated, their positions being randomly picked among the 509 positions sampling the gray matter, with random orientations. An example of one such instance can be seen in Figure 3.13. Considering

unitary amplitudes for these dipoles, the noise power projections on the electrodes are computed as follows, similarly as for equation 3.3:

$$P_{noise} = \frac{1}{5N_c} \sum_i \sum_m \phi(j_{n_i})_m^2 \tag{3.5}$$

The squared amplitude a^2 of these five dipoles (of equal amplitude) is then adjusted as follows to reach the desired averaged SNR L_{SNR}:

$$a^2 = \frac{P_{avg}}{10^{L_{SNR}/10} * P_{noise}} \tag{3.6}$$

we also consider the set $\{20dB, 10dB, 3dB, 0dB\}$ for L_{SNR} in this context of noise.

For each kind of noise and noise level, 100 different realizations of noise are added to the data, keeping the same set of 100 realizations for each of the 509×3 dipoles in order to ensure equal treatment for each different source position and orientation.

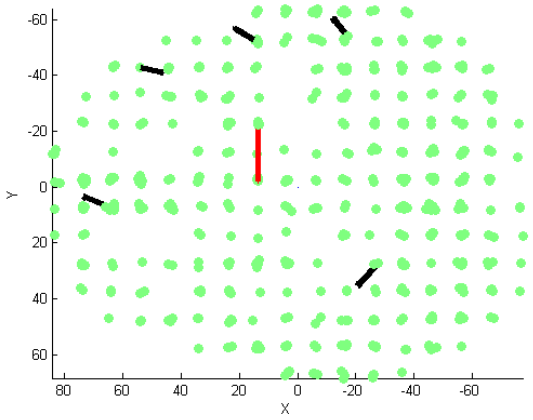

Figure 3.13: Example of 5 dipoles used to create one instance of the correlated noise. Source in red and perturbation sources in black. In green all the 509 dipole coordinates.

	All			**Ipsi**		
	ε_p	$\varepsilon_{p,left}$	$\varepsilon_{p,right}$	ε_p	$\varepsilon_{p,left}$	$\varepsilon_{p,right}$
SNR (dB)	*White noise*					
∞	3.87	4.65	3.32	4.43	7.52	3.17
20	6	7.03	5.04	14.64	24.63	5.29
10	11.31	14.42	8.41	24.61	40.95	9.33
3	23.99	32.57	15.96	32.64	48.84	17.48
0	31.91	42.61	21.90	36.68	51.80	22.54
	Correlated noise					
∞	3.87	4.65	3.32	4.43	7.52	3.17
20	10.12	12.87	7.54	16.9	26.99	7.47
10	32.51	43.8	21.96	30.05	40.63	20.16
3	55.36	68.4	43.16	42.01	48.01	36.39
0	63.5	74.91	52.82	47.65	50.97	44.55

Table 3.3: Median of localization errors (in mm), after averaging the three direction errors $(0x, 0y, 0z)$ in case of white and correlated noise. In the first line are recalled the results in the no noise case (∞ dB).

Boxplots of localization errors for both noise contexts are given in Figure 3.14. This data is summed up as localization errors median in the Table 3.3. The errors are first averaged over the three Cartesian directions for each

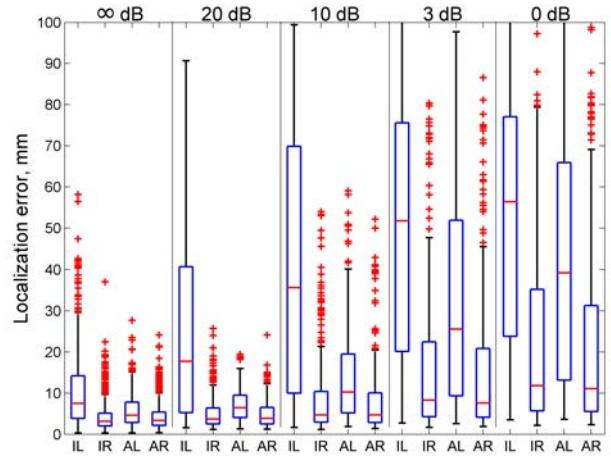

(a) White noise

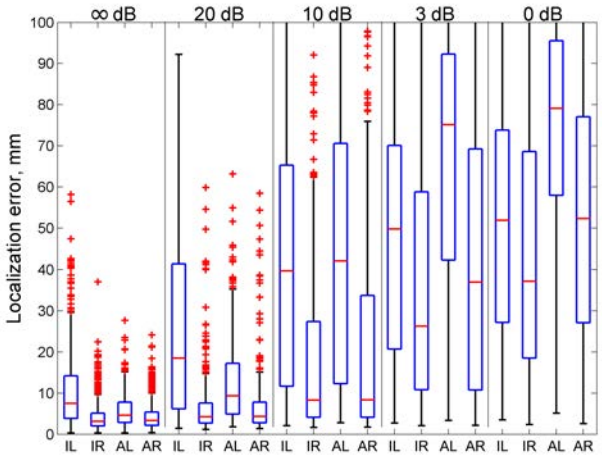

(b) Coherent noise

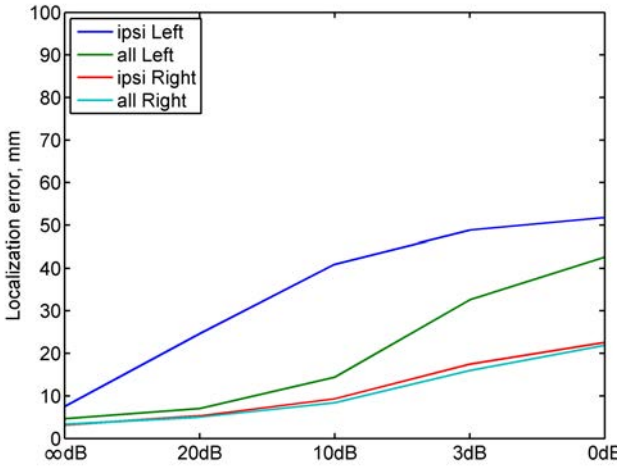

(c) White noise

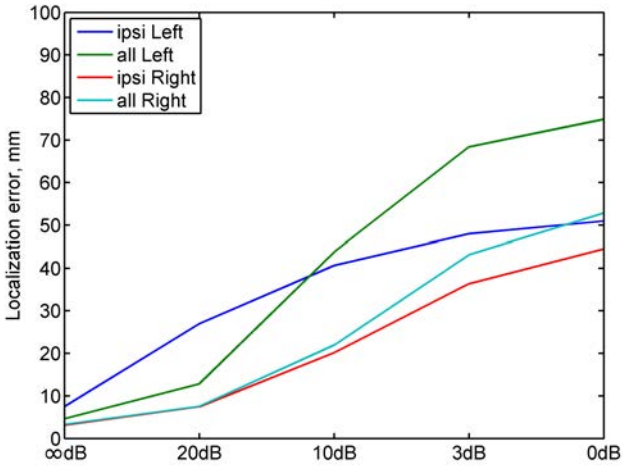

(d) Coherent noise

Figure 3.14: Boxplots of localization errors for both types of noise: (a) white noise and (b) coherent noise and their respective medians in (c) and (d). All localization was done using OSM model. In the first column, the results in absence of noise (∞ dB) are reminded for comparison purposes. In the remaining four columns, from left to right, are boxplots for $20dB$, $10dB$, $3dB$ and $0dB$ levels of noise respectively. Within each column, ipsi-lateral and all configurations are considered, for dipoles lying in the left and right hemispheres separately.

single position and noise realization. We also provide the median of minimum and maximum error over the three directions to get an idea of the error range between best and worst case of source orientation.

Considering the white noise context, the ECD localization shows interesting robustness to noise up to $10dB$, the accuracy drops from about $3mm$ to $11mm$ in the All configurations. The errors are significantly lower for the dipoles lying in the well implanted right hemisphere, confirming the intuitive idea that a sufficient number of close sensors is necessary for accurate source localization in a noisy context. Such observations are confirmed by the results obtained with lateral sensors configurations, the right ipsi-lateral configuration being much more robust than the left one, due to the low number of electrodes implanted in the left hemisphere. In this context of white noise, however, the All configuration brings consistently lower median errors than the right ipsi-lateral one (8.4mm vs 9.3mm in the 10dB case). Additive white noise does not correlate with the projection pattern of a dipole on the sensors. By spatial regression effect, the addition of sensors with low SNR (*e.g.*, from the contra-lateral hemisphere) still brings

additional information for localizing the dominant dipole of interest.

This is obviously not the case when correlated noise simulating the projection of disturbance dipoles is added. In this case, far dipoles with low SNR are likely to be impacted by dipolar projection patterns. In this noise context, better localization results might be expected when restricting the localization to close sensors, *e.g.*, to the sensors of the ipsi-lateral hemisphere. This is indeed the case over all the configurations of noise level and source positions (left or right hemisphere). However, the localization is satisfactory (under $1cm$ error in median) only with a favorable noise level (20dB case) for the dipoles of the right hemisphere (both for All and ipsi configurations). The medians quickly increase over $2cm$.

Analyzing in more depth the well localized dipoles case by case, it turns out that the well localized dipoles in the $10dB$ case mostly lie within a 30mm distance from the closest sensor. Inversely, the most superficial dipoles, situated near the skull border and not surrounded by sensors, are badly localized in most cases, even in the no noise case. These results urge us to study the best configuration of sensors that must be used for reliable SEEG ECD source localization. From our observations, the selection of a sufficient number of sensors close to the source might be a conclusive strategy, as illustrated by the performance of the right ipsi-lateral configuration. We deepen this direction in the last chapter of the thesis, by proposing a local approach for dipole localization.

3.5 Localization results on real signals

The localization method is applied and evaluated on real SEEG recordings. Two types of signals are presented: SEEG recorded during Intracerebral stimulations (ICS), thus in the case of a known generator, and SEEG recorded during a sequence of epileptic spikes.

3.5.1 ICS localization

This study includes one 40-year-old man with presumed bitemporal lobe epilepsy. Usual seizures started with bilateral auditive hallucinations (wind sound). No anatomical lesion was found in MR images. The patient gave his informed consent prior to participation. According to the electroclinical hypothesis, he was implanted with ten depth electrodes in the right temporal lobe and insular cortex and four in the left temporal lobe. After eliminating sensors too close to skull or having defective connections, this left us with 94 sensors on the left and 32 sensors on the right hemisphere. The reference was FPz surface electrode from the classical 10-20 system. The depth sensors coordinates were automatically determined using the procedure described in [Hofmanis et al. 2011].

Before applying the localization procedure on the ICS signals, some basic pre-processing steps need to be performed. A window of 2.5 seconds was chosen during the stabilized stimulation period[1]. A simple high-pass filter followed by thresholding was applied to detect the peaks of the stimulation patterns. Between 60 and 90 peaks were detected during the 2.5 seconds (below the maximum value of 132 peaks corresponding to a stimulation frequency of 53 Hz). Their amplitudes were averaged electrode by electrode to obtain the amplitudes of an averaged ICS pattern, used further in the localization procedure.

Despite this preprocessing, we must underline that there is no guarantee that the physiological activity recorded by other sensors will be eliminated by averaging (although white noise will be substantially reduced). Although the

[1] It has to be noted that the contacts used for stimulation were used, before and after the stimulation period, as recording contacts. Therefore, an electrical commutation artefact lasting up to 2 seconds might appear at the beginning of the ICS period (see also [Hofmanis et al. 2013] for more details).

		TB'2-TB'3			TB'5-TB'6			TB'8-TB'9		
Cfg	Model	ε_p	ε_a	GOF	ε_p	ε_a	GOF	ε_p	ε_a	GOF
Ipsi	IHM	2.5	8.1	99.4	4.9	19.2	99.4	1.9	22.4	99.9
	OSM	1.0	9.0	99.6	1.3	7.4	99.8	8.9	19.5	98.6
Contra	IHM	41.1	53.3	85.9	225.6	75.8	95.3	153.3	100.3	92.7
	OSM	40.1	74.7	88.4	105.4	115.8	95.3	88.3	93.4	92.4
All	IHM	2.3	9.0	98.1	8.9	21.4	94.8	200.8	92.5	72.4
	OSM	0.4	9.1	97.8	3.0	14.1	97.6	92.1	86.1	73.8

Table 3.4: Localization results for the three tested ICS dipoles, for all-sensors configurations and for both simple propagation models (IHM and OSM). The position error ε_p is given in mm, the orientation error ε_a in degrees and the goodness of fit (GOF) in percent.

ICS source is strong, it cannot strictly be considered as dominant with respect to the physiological activity recorded by distant sensors. Indeed, the amplitudes of the potentials generated by the ICS decrease very rapidly with the distance and thus the SNR in far electrodes rapidly becomes negative, the potentials at more than $20mm$ having roughly the same magnitude as the background activity (see figure 3.15).

Finally, the contacts belonging to the electrode generating the ICS have been discarded from the localization procedure, the contacts close from the stimulation site being saturated by the strong electrical field. Also, we would like to assess if such strong dipole could be localized using only far measurements.

Having these general considerations in mind, we have tested our localization procedure for three electrical stimulation sites, from respectively deep to superficial brain localizations: TB'2-3 situated in the entorhinal cortex, TB'5-6 in the perirhinal cortex and TB'8-9 in the inferior temporal gyrus (see Figure 3.15). All of them were in the left hemisphere, less implanted than the right one. As for the simulated signals, we used the four spatial sensors configuration described above (subsection 3.1.1).

The localization was performed with the 3 same sensor configurations as described before: all available contacts (except those situated on the same electrode shaft as the ICS, namely TB'), all contacts in the ipsilateral hemisphere (again except TB') and all contacts in the contralateral hemisphere. Both IHM and OSM models were used in the inversion procedure. The localization results, in terms of position errors, orientation errors and GOF are given in Table 3.4, and Figure 3.16 provides a visualization of the localization results.

In general, we can conclude that the ipsilateral configuration offers the best localization performances, with position errors below 9mm and orientation errors below 22.4° regardless of the ICS source position and on the model used for the inversion (IHM or OSM). It confirms the robustness obtained in simulation. If we focus on the profound and intermediate dipoles, the all-sensors configuration also provides good results (below 10 mm), but this sensor configuration shows its limits when considering the outermost ICS source. This result is not necessarily unexpected and it also confirms the simulation results: in real situations, other (unknown) sources are active in the brain, superimposing to the propagation of interest a colored nuisance on the measurements. Thus, the initial hypothesis of one dominant source might not be valid anymore, especially when the ICS dipole is far from the center of the head and is therefore hardly visible to the electrodes situated in the opposite hemisphere. Finally, and for the same reasons, the contra-lateral configuration is particularly unreliable. Although rather high GOF values are still obtained under this configuration, emphasizing that this criterion has to be analyzed with care.

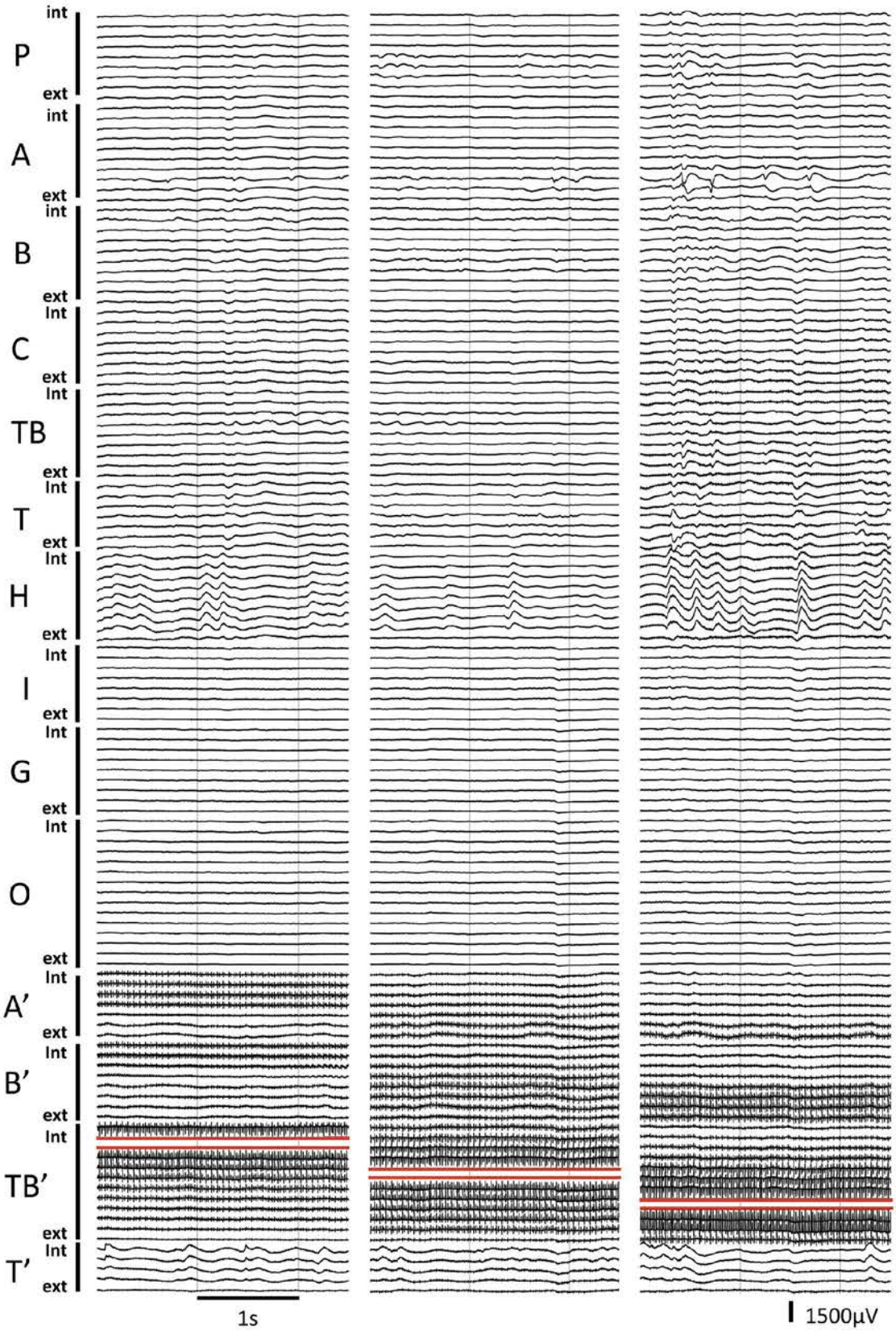

Figure 3.15: Two and a half seconds of SEEG signals recorded during three ICS sessions. From left to right, the ICS was applied between the TB'2-3, TB'5-6 and TB'8-9 contacts (profound, intermediate, superficial). The stimulation contacts are figured in red

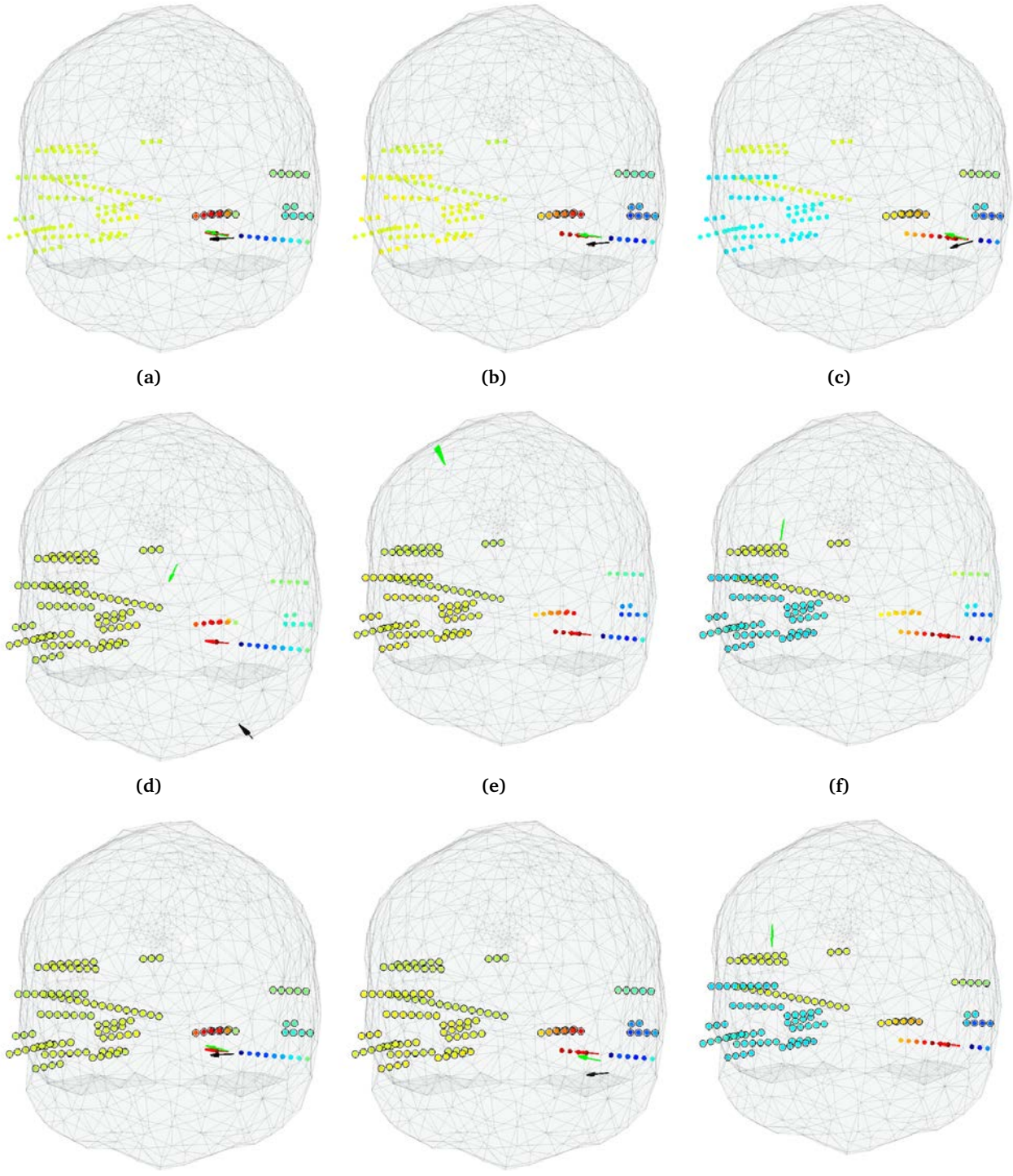

Figure 3.16: Localization results for the ICS dipoles situated between TB'2-3 (first column), TB'5-6 (second column) and TB'8-9 (third column) : (a,b,c) using all contacts in the ipsilateral hemisphere, except those of the stimulation electrode; (d,e,f) using all contacts in the contralateral hemisphere; (g,h,i) using all contacts, except those belonging to the stimulation electrode. The color scale on each contact represents the time-averaged value of the recorded potential (from dark red for highest values to dark blue for lowest values). The used contacts are circled in black on all figures. The red arrow indicates the ICS dipole position and orientation, the black arrow indicates the results of the localization procedure using the IHM and the green arrow the dipole estimated using the OSM. The IHM results (black arrow) is missing in figures (e,f,i) as the estimated dipoles converged outside the head volume. The actual values of the errors and the corresponding *GOF* are given in the Table 3.4

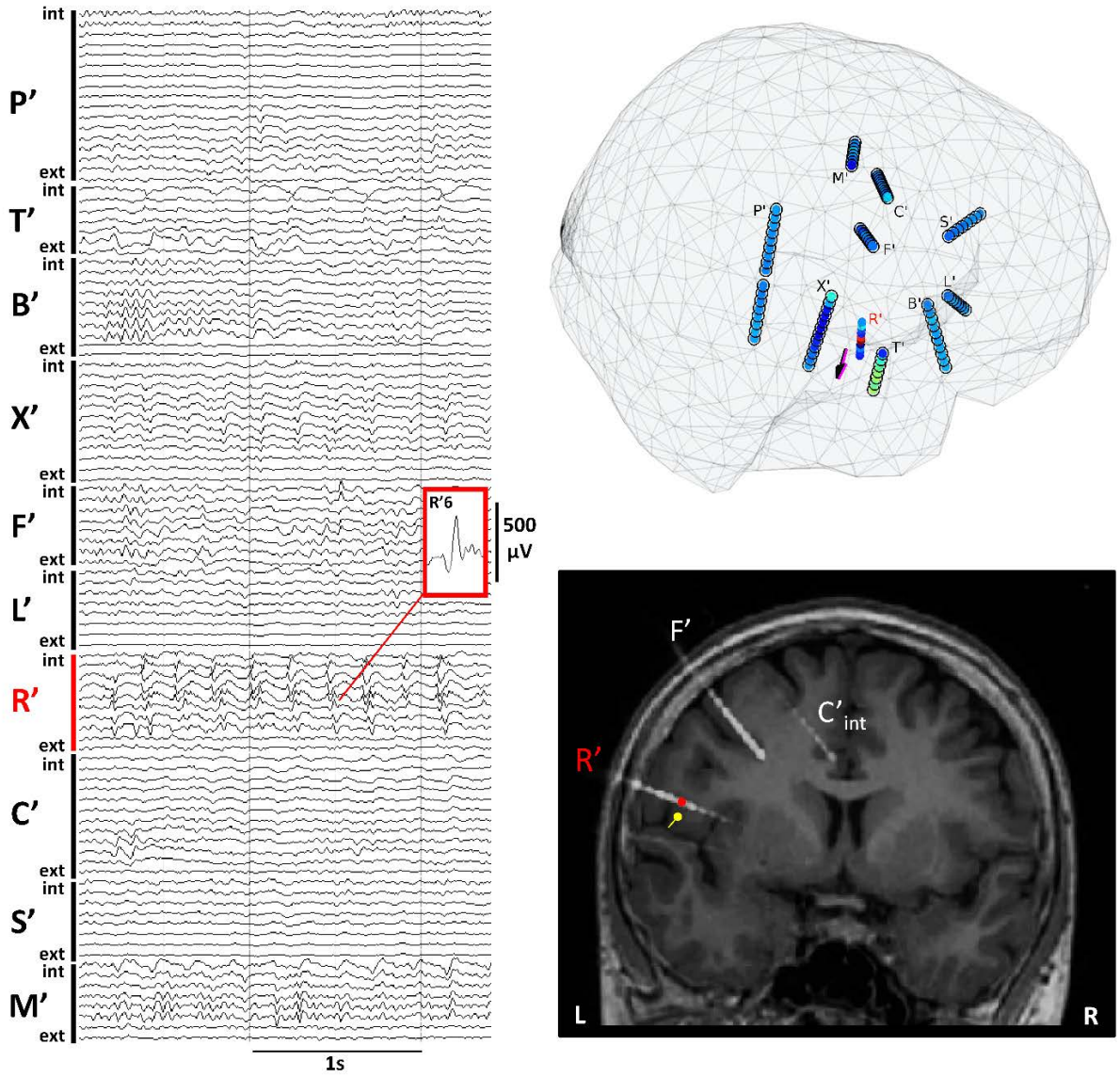

Figure 3.17: Source localization of interictal epileptic spikes: case of a 28 year-old woman with drug-resistant epilepsy. Left side: SEEG signals in common reference montage (FPz scalp electrode) during interictal period. Epileptic spikes were recorded in the middle contacts of R' depth electrode (left central operculum). Top right: 3D view of all depth electrodes in a realistic brain mesh. The sensors used for localization are circled in black. The localized dipoles, almost superimposed, are figured in black (IHM) and in magenta (OSM) (coordinates of the origin at x: −50.1 mm; y: −4.8 mm; z: 27.2 mm). Bottom right: frontal slice of CT-MR co-registration that shows trajectories of depth electrodes R', F' and a part of C'. Red dot indicates the position (x: −47.5 mm; y: −6.3 mm; z: 30.7 mm) of R'6 contact where epileptic spikes were recorded with the highest amplitude. The dipole source (OSM inversion in yellow) was localized in the left central operculum at 4.6 mm distance from R'6.

3.5.2 Epileptic spikes localization

A 28 year-old woman with drug-resistant insulo-opercular epilepsy was included in this study. She gave her informed consent prior to participation. Epileptic seizures started with a left-side head deviation and a right upper limb tonic elevation. After presurgical evaluation, depth EEG recording was performed using ten depth electrodes implanted in the insulo-opercular regions as follows (internal and lateral contacts): P', cingulum/parietal operculum ; T', infero-anterior insula/ superior temporal gyrus ; B', anterior insula/pre-motor cortex; X', posterior insula/post-central gyrus; F', and L', anterior and posterior part of the inferior frontal sulcus/middle frontal gyrus; R', middle insula/central operculum; C', cingulum/middle frontal gyrus; S', superior frontal sulcus; M', supplementary motor area/superior frontal gyrus. During SEEG investigation, interictal epileptic spikes were recorded by the R' depth electrode. These spikes were selected for this study due to (i) their relatively high signal to noise ratio and (ii) their focal localization, *i.e.*, the absence of other co-activated epileptic sources (Figure 3.17, left side).

Time averaging was performed using the following procedure: the signal from the R'6 contact (presenting highest amplitude spikes, thus assumed to be the position of the source) was high-pass filtered. Twenty spikes were then selected by thresholding and confirmed by a trained electrophysiologist. One hundred time samples belonging to these 20 spikes overpassed the chosen threshold (set at one half of the amplitude of the highest spike) and thus averaged. The localization is further performed using these averaged potentials.

The results in this example are very convincing (see Figure 3.17): after eliminating the electrode on which the spikes present a maximum amplitude (R'), the localization was made using both analytical models (IHM and OSM), after having selected and averaged over 20 spikes. The results are very similar and very precise: the source is localized at less than 5mm from the contact presenting the highest amplitude (R'6), in the same anatomical structure (left central operculum). The obtained *GOF* is correct (72% for IHM and 74% for OSM), knowing that other sources might be present in the distant explored structures. The results above are confirmed when localizing using all available sensors, including those from the R' electrode. In this case, the distance between R'6 and the origin of the dipole diminishes to 1.2mm for the OSM based inversion and to 1.4mm for the IHM, with almost similar *GOF*s of 77% for the IHM and 78% for the OSM. Interestingly enough, the number of electrodes used for localization can be drastically reduced. Obviously, the results depend on the chosen spatial configuration. For example, when preserving only 3 electrodes (B', T' and X') having 29 contacts, the OSM still provides a localization at 7.5mm from R'6, while the IHM converges at 6.3mm, with *GOF*s equal to 82% for both models. Last but not least, these good results are coherent among themselves, with a maximal distance between the solutions of below 7mm regardless of the forward model and the chosen sensor configuration (among the 3 configurations discussed above).

Finally, we also perform the localization on each of the twenty epileptic spikes separately, using either all available contacts or only the 3 selected electrodes B', T' and X'. For each spike, the time samples above the threshold are retained in the localization process. As expected, the results are less accurate than in the averaged case, illustrating the importance of the averaging. For the first sensor configuration (all contacts in the hemisphere, except those on R'), the mean position of these twenty estimated dipoles is placed at 13.2mm from R'6, with standard deviations of 18.7, 18.0 and 23.0mm in x, y and z directions respectively. For the second configuration (29 sensors only, on 3 electrodes), the mean position is at 9.2mm, with standard deviations of 14.1, 6.5 and 5.9mm respectively. It is important to notice that using only the sensors having a rather high SNR (close to the presumed origin of the spike) improves the quality of individual spikes localization, as the time averaging becomes less critical. This shows us that

increasing the number of spikes in the averaging indeed enhances the SNR, and thus the localization accuracy. But when the number of available spikes is low for averaging, an adequate sensor configuration close to the source has to be chosen.

3.6 Conclusion

The feasibility of dipole source localization from SEEG measurements has been studied in this chapter, based on the hypothesis of a dominant dipole to localize under a common clinical SEEG implantation scheme. We demonstrate, under a realistic simulation setup, the theoretical feasibility of ECD localization from SEEG based on analytical propagation modeling, up to a centimeter's localization error, an accepted margin in this clinical context. While the IHM shows limitations in accurately reconstructing the source projection more than 2cm away from the position of the source, the OSM provides better modeling power up to 3cm. First results in an ideal no noise environment confirm these observations, the localization accuracy being significantly better when carried out using an OSM model.

However, due to inherent model errors of such rough spherical modeling, some dipoles were found not to be identifiable. This set of 50 dipoles is found to lie near to the skull border, predominantly in the frontal and occipital regions, where the sphere does not closely model the particular skull shape (see Figures 3.12 and 3.10). These areas are both far from any sensor placement and close to the brain frontier, increasing the uncertainties in the forward model accuracy. Nevertheless, as our 509 dipole positions homogeneously sample the gray matter volume, it means that about 90% of the brain source area is theoretically identifiable under this specific SEEG setup.

Considering the used sensor configuration, we found that a sufficient number of close sensors are needed for accurate brain source localization, as shown by the weak performance obtained when using only 6 sensors, or contralateral sensors to the source. On the other hand, to some degree the addition of more sensors to the setup does not guarantee a better localization performance, as shown by comparing results when using the Ipsi-lateral sensors for the right (well implanted) hemisphere, versus results when considering all the available sensors. The addition of far sensors is even likely to worsen the results, due to the uncertainties in the propagation modeling from the source to such distant measurement points.

These observations are confirmed by our simulations under a noisy environment. While the addition of a fair level of white Gaussian noise (up to 10dB) does not strongly affect the localization performance when the number of surrounding sensors is sufficient (right hemisphere dipoles), the decrease in performance is spectacular in the presence of more realistic colored noise. Under such perturbations, the medians in the right ipsi-lateral case are consistently slightly lower than this when using the whole set of sensors, although globally unsatisfactory in both cases. Mainly, it underlines the importance of the pre-processing step to increase the SNR of the activity of interest. Besides, this calls for a deeper analysis of the set of sensors to be recruited in the localization process toward reliable SEEG source localization. This issue is addressed in the next chapter.

Chapter 4

Local approach for SEEG dipole fitting

In this chapter we further investigate the influence of the sensor configuration on the SEEG dipole fitting problem. From the experiments driven in the previous chapter, we can extract several observations about the adequate set of sensors to be chosen. First, using the whole set of available sensors does not guarantee to provide the best localization results. While in the absence of noise as well as in the case of additive white noise, the All configuration consistently outperformed the Ipsi configuration, we emphasized the superiority of this last configuration in the more realistic context of correlated noise, *i.e.*, when co-occurring physiological activities also impact the measurements (nuisance dipoles/ background noise). This indicates that a careful choice of sensors might significantly impact the localization accuracy and robustness. Indeed, the use of close sensors to the source ensures the highest signal to noise ratio and avoids far measurements that are likely to be corrupted by other co-occurring activities.

On the other hand, in the previous chapters it has also been stressed that a minimum number of sensors is needed to reach satisfactory localization results, with increased accuracy when the dipole is surrounded by a cloud of sensors. A compromise is thus to be found between closeness of the sensors, number of sensors as well as their spatial repartition.

Starting from the 509 dipole positions as defined in the previous chapter, and considering the three Cartesian directions for the sources, we explore increasing subsets of surrounding sensors to be used in the localization process, and we extract a criterion of sensor repartition yielding the highest ratio of localized sources (within the 1 cm error margin rule adopted in this thesis). Based on this criterion, in the second part of the chapter we propose a local approach for solving the ECD localization problem, and we compare its performance with the global strategy where all of the available sensors are used (All configuration). In the third part we analyze the SEEG dipole fitting problem in terms of zones of confidence, splitting the brain volume in several areas with respect to their distance to the set of sensors (defined by the distance to the closest sensor). We extract quantitative facts about the confidence we can have in a ECD fitting output with respect to the area in which the solution is lying.

Another objective of this chapter is to provide practical guidelines for SEEG dipole fitting at the direction of the clinician, helping him perform a critical analysis of the outcome of the localization result. In particular, we put into question the relevancy of the Goodness Of Fit (GOF) as the unique criterion to evaluate the accuracy of a solution. In this SEEG context, we show that the GOF might be misleading when choosing the source localization and we instead propose a strategy combining some plausibility criteria (closeness to the gray matter), confidence criteria (closeness to the sensors) and clinical choice among a set of possible/ plausible/ confident solutions.

4.1 Local approach: study of necessary conditions

We consider the 509 source positions sampling the gray matter (see Subsection 3.3.2). ECD localizations are performed on each of these 509 dipole positions (considering each of the three Cartesian orientations) using subsets of sensors of increasing size, starting from the closest sensors to the *a priori* known source position. From these simulations we intend to elaborate on a strategy to identify the optimal subset of sensors for confident source localizations with respect to the position of the sources. In this objective we pay particular attention to several key points which will help us in identifying quantifiable criteria for sensor selection.

Limiting the spatial extent of the used sensors guarantees that the sensors with the highest SNR are used in the localization. Thus it seems relevant to restrict the set of recruited sensors to the subset of closest sensors surrounding the source. However, the resolution of such a non-linear inverse problem requires a sufficient amount of sensors, while the addition of far sensors with low SNR is likely to worsen the localization results. A compromise is thus to be determined, though it cannot be determined solely by restricting the set of used sensors to those within a fixed distance to the source. This motivates the introduction of a sensor subset repartition criterion that is able to handle both of these aforementioned issues.

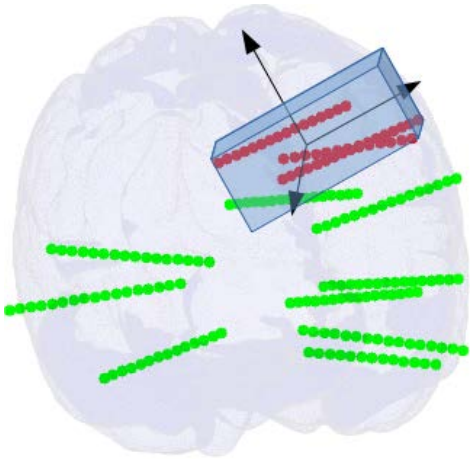

Figure 4.1: Illustration of rectangular parallelepiped that includes the subset of sensors used. Sensors used are shown in red while other sensors are shown in green. Three arrows represent the new set of orthogonal axes aligned to the axis of highest variance of spatial repartition.

An important aspect which has been discussed earlier is the spatial repartition of the sensors. During the analysis of the simulations presented in the chapter 3, we concluded that the dipoles well surrounded by sensors were the ones yielding the best localization accuracy. Inversely, using an unbalanced cloud of sensors might contribute to the under-determination of the inverse problem (such as discussed in the Subsection 3.1.1). This spatial balance of a chosen set of sensors can be quantified through a spatial *conditioning* factor, computed as the ratio between the longest and the shortest axis of the rectangular parallelepiped including the sensors of the subset (illustrated in Figure 4.1). In practice, this is computed as follows:

1. a Principal Component Analysis of the cloud of sensors determines a new orthogonal set of axes aligned to the axis of highest variance (in terms of sensor spatial repartition);

2. the actual positions of the sensors are transformed into this new Cartesian space;

3. the spatial conditioning factor is computed as the ratio between the biggest and the smallest range of projections on these 3 new axes.

To summarize, assume $\mathbf{X}$ as the spatial coordinates of a given sensor subset ($N_c \times 3$), centered. The eigendecomposition of $\mathbf{R_X} = \mathbf{X}^T\mathbf{X}$ writes:

$$\mathbf{R_X} = \mathbf{UDU}^T$$

and the projected spatial coordinates onto the PCA basis become:

$$\mathbf{X}_p = \mathbf{XU}$$

The spatial conditioning will be given by the ratio between the max and the min column ranges of $\mathbf{X}_p$:

$$r_c = \frac{\max_j(\max_i(x_{p,ij}) - \min_i(x_{p,ij}))}{\min_j(\max_i(x_{p,ij}) - \min_i(x_{p,ij}))} \tag{4.1}$$

where $x_{p,ij}$ is the (i,j) element of the matrix $\mathbf{X}_p$.

The lower this conditioning factor, the more balanced the cloud of sensors. A ratio of one is associated to a balanced repartition in each direction (sensors are included in a cube), while a high one is related to a cloud almost restricted to a 2-D plane. In the following we will further analyze the influence of this factor on the localization accuracy, and we will show that such a criterion also guarantees the inclusion of a sufficient number of sensors within a limited distance to the source.

4.1.1 Sensor subset repartition

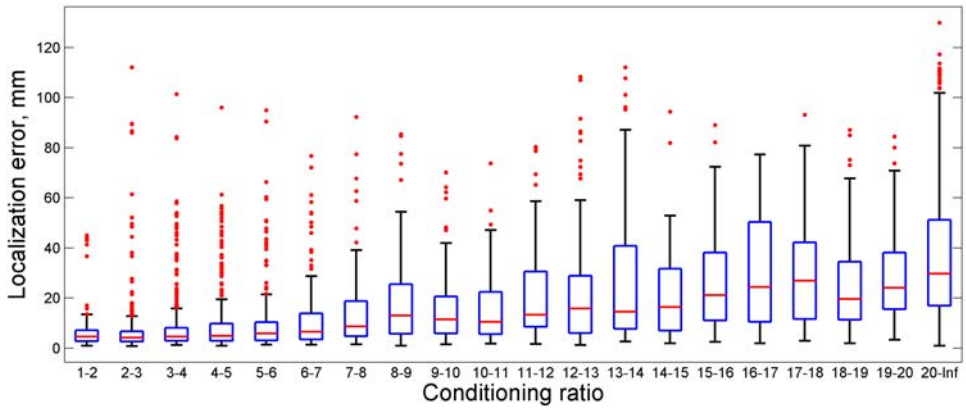

Figure 4.2: Boxplots of localization error per conditioning ratio bins of 1 cm in the no noise case.

Similarly, as in the previous chapter, we run simulations by projecting the dipoles on the sensors using a five compartment FEM. The inversion is carried out using an OSM, with the sphere fitted on the brain mesh. For each position, the localization is performed using several subsets of sensors of increasing size, by selecting the sensors included in a sphere of increasing radius centered on the current source position. The sphere is increased by 1 cm at each step, yielding about 15 subsets of sensors for each source position on average. For each sphere, the ECD fitting algorithm is initialized with $N = 20$ multi-start positions. Among the 20 final identified dipoles, the closest dipole to the source is selected as the final (best) solution (note that this is not necessarily the best goodness of fit).

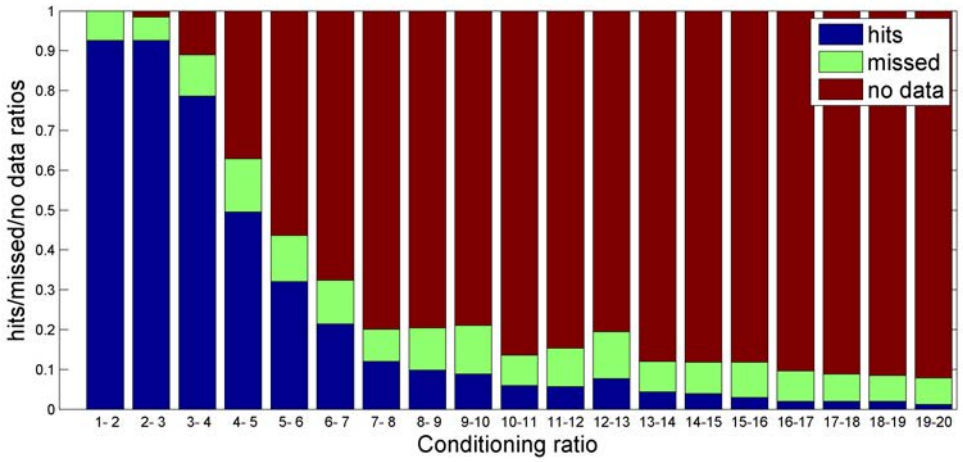

Figure 4.3: Ratios of hits and misses (and no data) for each dipole, grouped by conditioning ratio bins of width 1, in the no noise case. For each bin, a dipole is counted as (i) a hit if there exists a surrounding sensor subset satisfying this conditioning ratio yielding a localization error under 1 cm, (ii) a missed if none of the existing surrounding sensor subset with this conditioning ratio yields a localization error under 1 cm or (iii) no data if no surrounding sensor subset satisfies this conditioning ratio.

The three Cartesian directions are considered separately (thus $3x509 = 1527$ dipoles). For each position and subset configuration we compute the mean of the three localization errors.

Figure 4.2 presents boxplots of dipole localization errors in the no noise case (the best solution among the 20 initializations), in function of the conditioning ratio computed on each particular sensor subset (as described in the introduction of this section). As expected, the lower the conditioning value, the higher the localization accuracy. Up to a conditioning ratio of 6, the medians are under 5 mm and the third quartiles under 1 cm, while these values dramatically increase with higher ratios. It is worth noticing that the repartition of the data over the conditioning ratio bins is not homogeneous, 65% of the data lies in the first five boxplots (conditioning ratios under 6) while 90% lie in the 19 first boxplots (conditioning ratios under 20). The remaining 10% are grouped within the last boxplot (range ratio from 20 to infinity).

A complementary view on these simulation results is given in Figure 4.3. The bars correspond to hits/misses ratios obtained when localizing with subsets of sensors having a spatial conditioning within a given bin of width 1. By hits, we understand the number of localizable dipoles (*i.e.*, error less than or equal to 1 cm, in blue), using a given conditioning. The missed dipoles ratio indicates the proportion of dipoles (among the 509) for which *all* sensor subsets, having a conditioning within the given bin, yield localization errors over 1 cm (in green). If no sensor subset configuration lies in the given conditioning range for a particular dipole, it is counted as a no data (red).

Please note that the conditioning ratio of the whole set of sensors is equal to 1.9, thus lying in the first group $1-2$. Therefore, the ratio of no data for this bin logically equals 0 (the subset containing all the sensors always exists for any dipole position). On the other hand, the hits ratio equals ≈ 0.93 for this bin, and this value is lower than the proportion of good localization using all sensors (≈ 0.97)[1]. The difference (*i.e.*, the higher number of missed dipoles) is explained by the fact that, in this bin, included also are localization results obtained with a much smaller (but well conditioned) sensor subset.

[1]As explained previously, these errors are to be explained by model errors, due to dipoles or to sensors close to the brain frontier.

The relative ratio of hits over misses constantly decreases with the conditioning ratio, and passes over the 1 value (more misses than hits) for a conditioning ratio over 10. In addition, over this conditioning ratio, the number of data per bin drops under 100, making the statistics less relevant. For these reasons in the following noisy context situation, we will limit ourselves to analyzing the conditioning ratios in the range of 1 to 10.

Based on these preliminary observations, we now analyze the localization performance in the context of colored noise, *i.e.*, when sources of disturbance are added to the measurements. The noise level varies between 20 dB to 10 and 3 dB (computed as explained in the previous chapter, Subsection 3.4.2). The results (localization error vs conditioning ratio) are summarized in the boxplots presented in Figure 4.4.

A first rapid analysis can be done by considering the 3 dB case, when the median localization errors consistently have an over 1 cm error whatever the conditioning ratio. We may conclude that in such low SNR context, the localization is not reliable. Still, some of the dipoles can be localized, and this first conclusion can be refined, as it will be discussed in Section 4.3. Looking at the 20 and 10 dB case, the lower medians are obtained for conditioning ratios in the ranges $2-3$ and $3-4$, with median values around 5 mm for 20 dB and 8 mm for 10 dB.

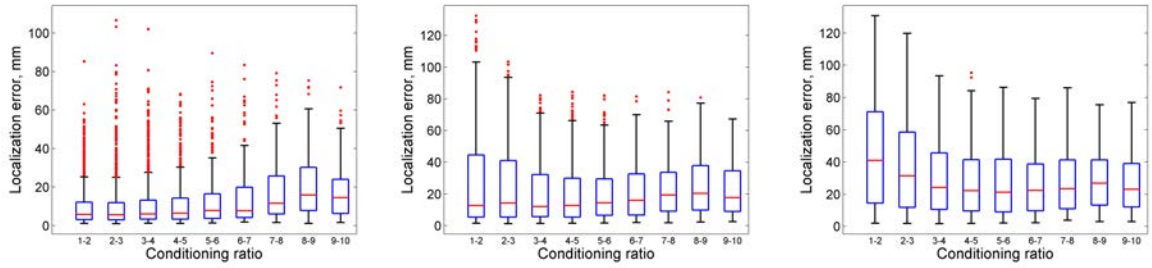

(a) 20 dB **(b)** 10 dB **(c)** 3 dB

Figure 4.4: Boxplots of localization error per conditioning ratio bins of size 1, with colored additive noise of 20, 10 and 3 dB.

It is not straightforward to extract a meaningful conditioning ratio rule from these figures. Thus, we present in Figure 4.5 localization ratios for each range of conditioning (similarly as in Figure 4.3 for the no noise case). In the case of a noise level related to a 3dB averaged SNR (see Subsection 3.4.2), the hit rates are consistently under 30%, confirming that in such a noise context an accurate localization is rarely achievable. For 20 and 10 dB however it appears that a conditioning between 2 and 3 is yielding the best localization hit rates (% of localization results under 1 cm). Such very low conditioning configurations are met when the repartition of the sensors subset is close to a sphere or a cube. To reach such a level of conditioning, it is clear that the sensors have to be placed on different SEEG shafts (most of the time at least 3) and that their numbers have to be rather high. Indeed, considering all the subsets having a conditioning between 2 and 3, the median number of sensors per subset is 89, with lower and upper quartiles of respectively 55 and 114. However it is important to note that the whole set of sensors (the *ALL* configuration) does not lie in this $2-3$ conditioning range (its spatial conditioning $r_c = 1.9$), confirming our hypothesis that a selection of a subset of sensors might indeed bring better localization results in a noisy context.

To conclude upon this first set of results, we can derive a heuristic rule stating that a maximum conditioning factor of 3 is needed for reliable localizations. Of course, this condition is neither sufficient nor necessary, but it seems to approximately quantify the need for a good conditioning of the inverse problem that we aim to solve.

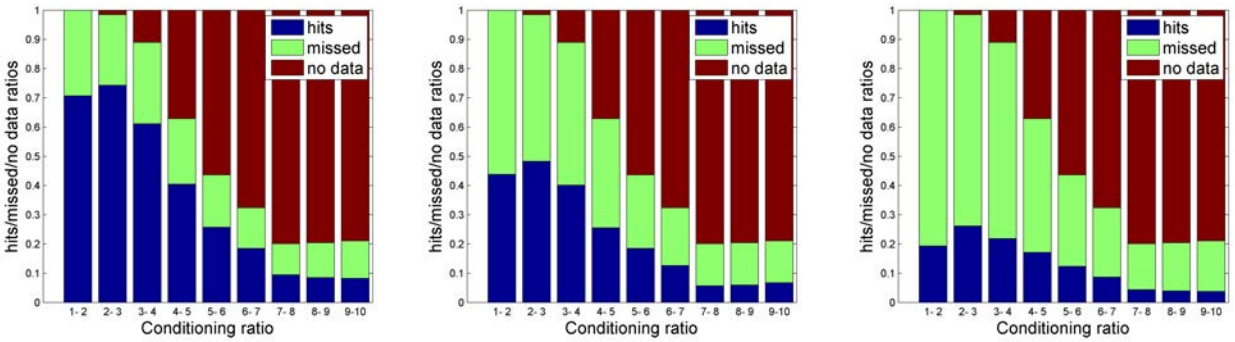

(a) 20 dB **(b)** 10 dB **(c)** 3 dB

Figure 4.5: Ratios of hits and missed (and no data) for each dipole within 1-width conditioning ratio bins (such as in Figure 4.3), with colored additive noise of 20, 10 and 3 dB.

With this range of conditioning factors in mind, we proceed to further analysis of the results, in order to strengthen our rule and optimize the sensor subset selection. An important observation is that, for each dipole, there often exist several sensor subsets around it, providing such a conditioning range below 3. The question is then - among the subsets with good conditioning, can we choose an optimal one?

A rather obvious idea is to take into account the volume occupied by these sensors. Indeed, assuming that the dipole that is to be localized is situated inside the cloud of sensors, the further the sensors are, the lower the signal to noise ratio will be. Therefore, a second heuristic rule would be to choose, among the well conditioned sensors, those situated at a minimum distance from the dipole that is to be localized. Of course, in real situations one does not know where this dipole is located, but the goal of the analysis presented in the first part of this chapter is to optimally determine the subset of sensors ensuring the best possible localization of a known dipole. The next subsection evaluates, therefore, the localization hit rates with respect to the radius of the sphere centered on the target dipole and including all the sensors of the selected subset (*i.e.*, the distance to farthest sensor from the source). We will only perform this analysis for well conditioned subsets, *i.e.*, with $r_c \leq 3$ (see Equation (4.1))).

4.1.2 Extent of used sensors

The results of the chapter 3 taught us that increasing the number of sensors does not guarantee to reach better localization accuracy in the presence of colored noise. Indeed, considering the decrease of the potential emitted by the source with the square of the distance to the source, the signal to noise ratio on far sensors can be dramatically low. Using such spurious information for localizing, the source inevitably leads to a decrease in performance. In this section we analyze the localization performance for well conditioned subsets of sensors with respect to their volume around the source to be localized, materialized by the radius of the sphere centered on the dipole. This analysis is carried out for the no noise case, as well as colored noise with different level of noise (averaged SNR of 20 dB, 10 dB, 3 dB).

The results are given as bar graphs (Figure 4.6) stacking the ratios of successful localizations (errors under 1 cm) with those of unsuccessful localizations (errors over 1 cm), with respect to the radius of the used subset of sensors (group by bins of 1 cm). In concordance with the previous results, we only consider, here, the subset of sensors with a conditioning of less than or equal to 3. As expected in the no noise case (∞ dB) the radius is not discriminant, the inclusion of far recordings still brings accurate information.

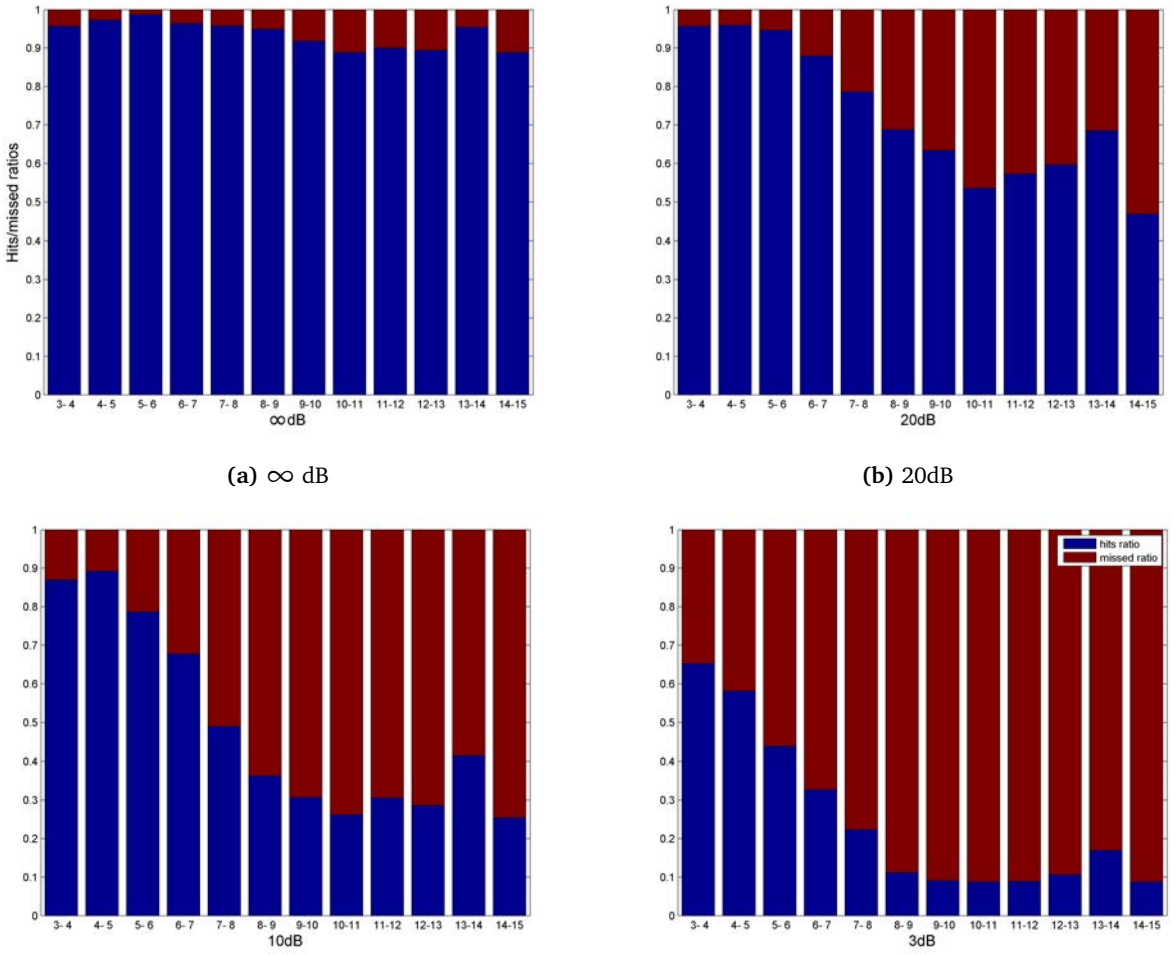

(a) ∞ dB

(b) 20dB

(c) 10dB

(d) 3dB

Figure 4.6: Hits/misses ratios vs radius of used subset (grouped by bins of 1 cm) for various levels of colored noise. The considered subsets have a conditioning ratio under 3.

When colored noise is added, the influence of the radius is obvious, as the hit rates collapse promptly with the size of the subset radius. In the 20 dB case, 90% of the dipoles are successfully localized when using a subset radius up to 6 cm, and up to 80% in the 10 dB case with a similar radius. In strong noise situations (3 dB), a radius under 4 cm is necessary to retrieve half of the dipole position with less than a 1 cm error. Please note that each dipole can be represented several times across the bins. Indeed, one can find different well conditioned ($r_c \leq 3$) subsets of sensors included in more or less larger spheres, with different localization performances.

A logical hypothesis would be that the best localization will be obtained when using sensors with a maximum signal to noise ratio, meaning sensors close to the dipole position, thus situated inside a sphere of minimum radius (but of course still keeping a good spatial conditioning). A second analysis can be performed to explore this hypothesis: how many dipoles can we correctly localize when using, among the well conditioned sensor subsets ($r_c \leq 3$), the one having a minimum radius?

Unlike the previous graphs (Figure 4.6), the hit/miss ratios using only one sensor subset per dipole (the minimum radius one) are presented in Figure 4.7. As expected, the ratios of hits/misses are slightly lower (each dipole being represented only once). The difference appears clearly for the high radius subsets, where the dipoles that were

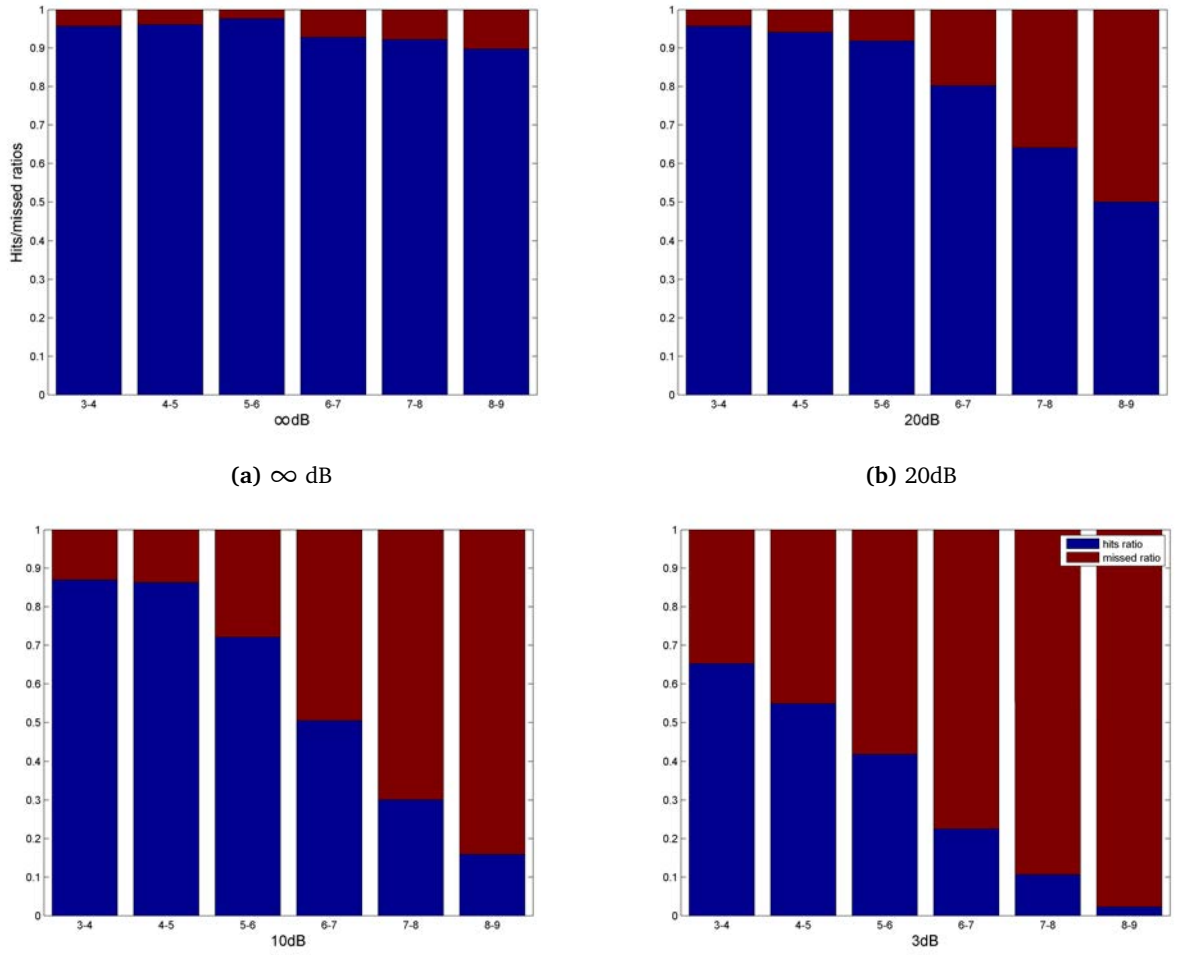

(a) ∞ dB

(b) 20dB

(c) 10dB

(d) 3dB

Figure 4.7: Hits/misses ratios vs minimum radius fulfilling the 3 conditioning ratio (grouped by bins of 1 cm) for various levels of colored noise.

correctly localized with a lower radius subset are not considered anymore (for every dipole, only the minimum radius is kept in the analysis). A first observation is that, if there are enough well conditioned sensors within a radius smaller than 5 cm, more than 80% of dipoles are localized down to a signal to noise ratio of 10 dB. The proportion of good localization for this type of configuration (sensors within a 5 cm radius around the dipole) decreases to almost 50% for stronger noises (3 dB). On the contrary, if the noise is rather low (20 dB), even when sensors as far as 9 cm from the source are needed to have a good spatial conditioning, about 50% of the sources can still be localized. Note that, in most of the cases, this situation appears when the dipole to be localized is actually far from all the sensors, and thus when the SNR *on all the sensors* is low (recall that the signal to noise ratios used in these simulations refer to a fixed level of noise regardless of the position of the dominant dipole with respect to the sensors, see chapter 3, Subsection 3.4.2).

In other words, the dipoles far from all the sensors are those needing the higher radius to reach the conditioning threshold, but are also those most impacted by the noise, explaining the collapse of the hits/misses ratio over a radius of $5-6$ cm in noisy cases.

To conclude with this section, we finally present bar graphs in Figure 4.8 representing, for each level of noise,

the ratio of retrieved dipoles (hits) when using the minimal subset radius with conditioning $r_c \leq 3$ (Figure 4.8a), and when using the maximum radius (*i.e.*, the whole set of sensors, Figure 4.8b). Over this ratio, we stack the ratio of dipoles that were missed when using the minimal radius but retrieved when using a higher subset radius, and respectively missed when using all the sensors but retrieved when using a lower subset radius (still considering subsets with conditioning ratio of 3). The remaining ratio represents the ratio of dipoles that cannot be localized (missed) whatever the used subset radius. As seen in Figure 4.8a, for all the noise levels, using a higher radius than the minimal one is only useful for about 5% of the 509 dipoles (*i.e.*, allow to recover the dipole position within a 1 cm error). To put it differently, among the dipoles localizable with any subset of well conditioned sensors, regardless of its radius, only about 5% are lost when the localization is performed with the smallest set of sensors, and this applies for all noise levels. Inversely, as illustrated in Figure 4.8b, when the whole set of sensors is used instead of the minimum radius one, about 10% of the localizable dipoles are missed for 20 and 10 dB, and 16% in the 3 dB case. It is noteworthy that, for this strong noise situation, only about 30% of the dipoles are actually localizable, all sensor subsets considered. Or, in other words, choosing to localize using all sensors instead of a (well conditioned) smaller subset leads to a division by two of the number of hits.

To conclude, the previous analysis indicates that a sensor selection criterion based on a minimal subset radius fulfilling a conditioning $r_c \leq 3$ seems relevant. This strategy will be assessed in the next section in the realistic case where the position of the dominant dipole to be retrieved is unknown.

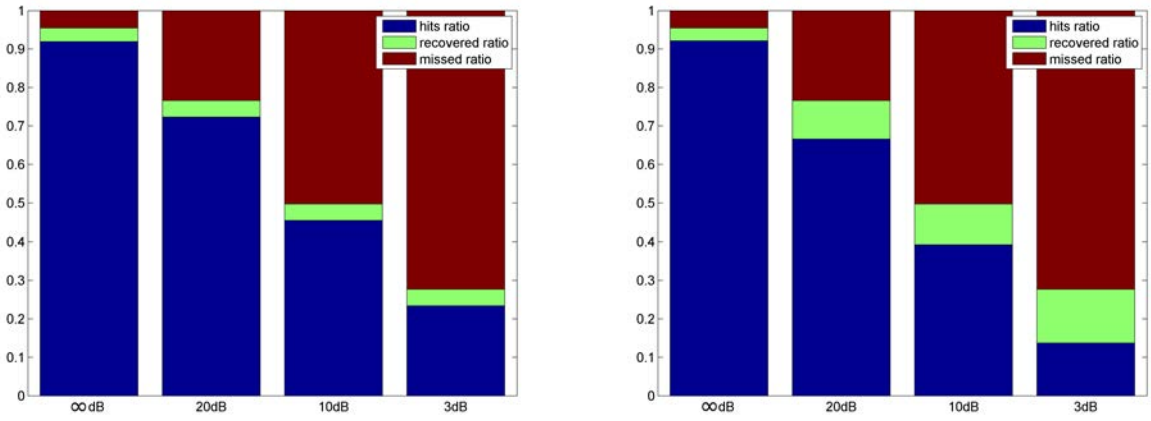

(a) **(b)**

Figure 4.8: For each level of noise, a ratio of hits (a) when the minimum radius fulfilling the 3 conditioning ratio is used, (b) when all the sensors are used. Among the dipoles not successfully localized within these subset configurations, we show (in green) the ratio of dipoles which can be recovered using another (higher for (a) lower for (b)) radius still fulfilling the 3 conditioning ratio. The remaining dipoles are those that cannot be localized with any subset with conditioning under 3.

4.2 Proposed local approach

In chapter 3 we found out that using the ipsi-lateral set of sensors with respect to the source significantly enhanced the localization accuracy, bringing us to study the opportunity of a local strategy for ECD fitting. Indeed, if it seems clear that the ipsi-lateral configuration is a medically guided choice of a subset of sensors providing better results than no choice at all, our previous analysis indicates that more objective criteria could be chosen in order do define an

optimal subset of sensors. Based on the spatial conditioning ratio of the sensors and on their distance to the source, as introduced in the previous section, we propose a genuine strategy for sensor subset selection. In particular, we show that in the presence of noise, restricting the subset of sensors to the ones surrounding the source while satisfying maximum conditioning ($r_c \leq 3$) is a relevant selection rule for a reliable ECD fitting procedure.

As before, we propose a strategy of simulation in order to evaluate the achieved improvements in realistic source localization scenarios, *i.e.*, when the actual source location is unknown (unlike in the previous section). We derive a local ECD fitting strategy described in the algorithm 1, which consists of a multi-start ECD optimization scheme where at each step the subset of closest and well conditioned sensors (conditioning ratio under 3) with respect to the current dipole estimated position is used. The optimization criterion is classical: minimize $f_{loc}(\mathbf{x})$, defined as the normalized squared error restricted to the potentials of the selected subset of closest sensors $\boldsymbol{\phi}^{loc}$ or, equivalently, maximize a locally defined goodness-of-fit:

$$\begin{aligned} f_{loc}(\mathbf{x}) &= \frac{\|\boldsymbol{\phi}^{loc} - \boldsymbol{\phi}_0^{loc}(\mathbf{x})\|}{\|\boldsymbol{\phi}^{loc}\|} \\ GOF_{loc}(\mathbf{x}) &= \sqrt{1 - f_{loc}(\mathbf{x})^2} \end{aligned} \tag{4.2}$$

with $\boldsymbol{\phi}_0^{loc}(\mathbf{x})$ the projection on the local set of sensors of the current dipole (with position and orientation parameters $\mathbf{x}$).

Algorithm 1 Local ECD fitting

1: Define 20 initialization points using the Riesz-energy minimization ((3.2))
2: **for** each initialization point **do**
3: **while** GOF_{loc} is increasing **do**
4: Select the closest sensors (euclidean distance) to the current solution so that a spatial conditioning ratio $r_c \leq 3$ is met
5: ECD fitting optimization
6: Define the new initialization point as the ECD solution
7: **end while**
8: **end for**

The procedure described by the algorithm 1 yields 20 solutions, all of them maximizing a local *GOF* (note that the solutions are not all necessarily different among themselves).

As before, we consider three levels of coherent noise (20 dB, 10 dB and 3 dB) as well as the no noise (∞ dB) case and we simulate 100 realization of this (background) noise for each noise level. To limit the computational burden of the simulations, we fix the orientations of the 509 dipoles to be radial (perpendicular to the surface of the sphere).

As mentioned previously, the proposed procedure can potentially yield 20 different localizations (although in practice this is seldom the case, as several initialization points might converge to the same solution). All or most of these solutions have a good local goodness of fit GOF_{loc} (recall that the *GOF* has higher values when evaluated on a reduced set of sensors). It is not obvious that choosing the best GOF_{loc} will automatically yield the correct solution/ best localization. In other words, the problem of choosing the correct localization solution becomes much more acute when using the local strategy described above: if the best (global) *GOF* is consistently similar to the correct localization when using all of the sensors, it is not guaranteed that the best local *GOF* is that reliable.

We have decided, thus, to separate the problem of choosing the right solution from the problem of finding it. Consequently, we first analyze if the proposed local strategy is indeed able to find the correct solution by manually (oracle) choosing the best solution among the 20 rendered by the algorithm.

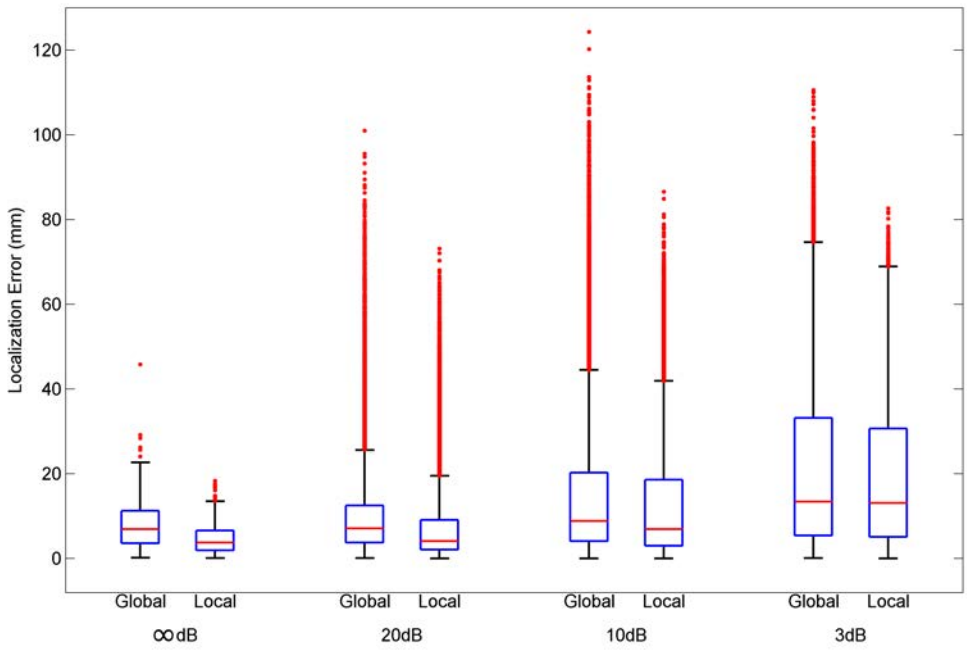

Figure 4.9: Boxplots of the localization errors (manually chosen closest candidates over the 20 multi-starts) when using the whole set of sensors (Global) and the proposed local strategy (Local), for the no noise ideal case and for 3 levels of coherent noise (20, 10 and 3 dB).

In a real context, however, it is impossible to pick this best solution when no prior on the source localization is available. Therefore, we analyze the localization performance when the choice is based on the GOF_{loc} (Equation (4.2)) computed on the local subset of sensors or on an *ad-hoc* criterion combining the local GOF_{loc} and the global GOF (the rationale being that both should be good for a dominant dipole).

As a compromise, we also propose an intermediary solution (between the 20 solutions obtained for the 20 initializations and the unique solutions picked by GOF_{loc} or GOF criteria). More precisely, we bypass this choice problem by proposing to the clinician a subset of plausible solutions, leaving the final choice to his expertise. In order to facilitate the clinician's choice, we merge the spatially clustered solutions and we eliminate the implausible ones (*i.e.*, those far from the gray matter and/or with negative GOFs).

4.2.1 Oracle chosen solutions

In a first-line analysis step, we question the accuracy of our local approach independently of the choice problem: if we can pick the best solution among the $N = 20$ multi-start convergence points, do we significantly enhance the localization performance when compared to a global (*ALL* configuration) approach?

As seen in Figure 4.9, the local method always gives lower medians and third quartiles on any of the tested noise levels.

It is noteworthy that it even outperforms the global approach in the no noise case. This rather surprising result can be explained by the propagation model errors that are higher on sensors close to the brain boundaries, systematically used in the *ALL* configuration but rather seldom when using a local strategy. Indeed, the local method, in

addition to keeping potentials with higher SNR, also globally uses less peripheral potential measurements for which the propagation model is less confident.

The benefits of our approach are appreciable, almost dividing by 2 the median value in the no noise (from 6.2 mm to 3.3 mm) and the 20 dB case (from 6.4 mm to 3.7 mm), while the boxplots tend to be similar between the two approaches when the noise level increases (from 7.9 mm to 6.1 mm in the 10 dB case and from 11.7 mm to 11.6 mm in the 3 dB case).

4.2.2 Can we pick the best solution?

While these results are encouraging, the problem of picking the best solution among the 20 multi-starts when the actual position of the dipole is unknown still remains. A first choice would be of course the dipole maximizing the GOF on the sensors, as usually chosen. In the context of our local approach, the dipole is localized maximizing the GOF_{loc} criterion, *i.e.*, a GOF evaluated on a limited amount of local sensors (Equation (4.2)), and it seems natural to select (among the 20 localizations) the solution maximizing this local GOF. In order to verify this rationale, we applied the GOF_{loc} selection rule on our simulated data for the four considered levels of noise (Figure 4.10). The results reveal that this local GOF criterion is irrelevant. Particularly in the no noise case, the localization errors reach 6.2cm in median. Further analyzing the produced local GOF for all the 20 solutions, it is observed that the GOF values are often very high even for erroneous solutions very far from the true dipole. This can be explained by the fact that the potentials on a set of low potential electrodes (far from the sources of interest) can be easily fitted by distant dipoles, yielding ghost sources and luring the localization process. Even more generally, having a good local GOF is easier on a subset of sensors, because less measurements need to be fitted. The most striking example is in fact given by the results in chapter 3 (table 3.2, where one can see that the GOF values are varying inversely with respect to the number of used sensors).

In the presence of noise, the medians are lower but still unsatisfactory (over 1 cm, see Figure 4.10) when compared to the performance obtained when the oracle best solution is manually chosen. In the 20 dB case, for example, the median value of the errors is equal to 15.4 mm when the local GOF selection strategy is adopted, while it reduces to 3.7 mm when the best solution is selected (see Figure 4.9).

It is important to remind here that the additive noise is spatially coherent, as it is produced by a set of 5 disturbing dipoles. One can imagine that the proposed approach might be lured by these dipoles when local sensors surrounding them are used for the localization, localizing them in place of the dipole of interest. Further analyzing this aspect, it appears that such a side effect does not significantly impact the performance, as the local approach identifies one of these dipoles of nuisance (*i.e.*, attributes a highest local GOF to a solution close to a dipole of nuisance) in place of the dominant dipole of interest in less than 1% of cases, independently of the noise level (*i.e.*, of the strength of these nuisance dipoles). The most likely explanation is then that, similarly as in the no noise case, erroneously placed dipoles explain the potentials on a reduced set of sensors, and one must be prudent in selecting the solution based solely on the local GOF.

The different previous arguments ultimately disqualify a GOF_{loc} based selection approach.

As an alternative, we might consider the GOF on the whole set of sensors (global GOF) in the decision process, in concordance with the hypothesis of the dominant dipole. Indeed, following this hypothesis, the solution should explain a large proportion of the potentials over the whole set of available sensors.

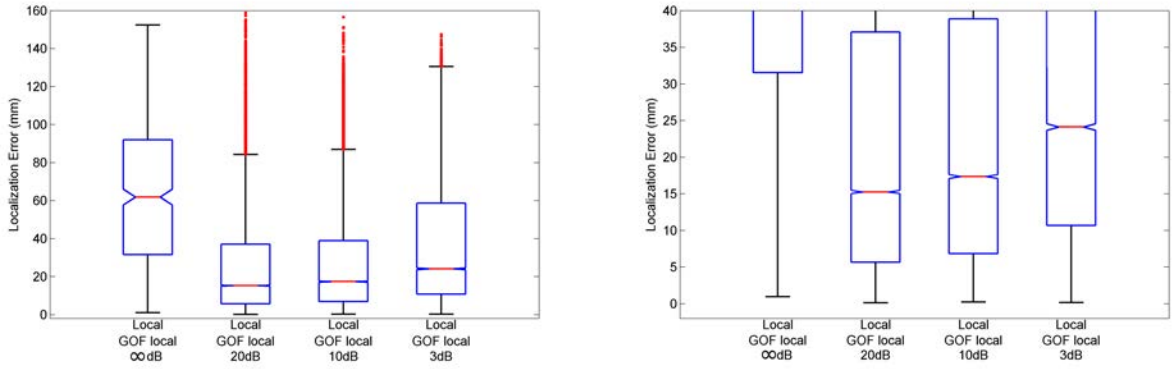

(a) **(b)**

Figure 4.10: Boxplots of localization errors when the solution is selected based on the maximum of the local GOF, for various levels of noise. The right figure is a zoom of the left one to appreciate the median values in the noisy case.

We then propose a two-step selection criterion involving both the local and global GOFs. The rationale behind is the following: assume that the noise level is known or can be estimated. Then, even a perfect estimation of the dominant dipole cannot have a 100% GOF_{loc}, because it only explains the part of the dipole on the sensors. Consequently, one does not have to look for a maximum GOF_{loc}, but rather try to fit a theoretical GOF. Assuming that the spatial signature of the dominant dipole (*i.e.*, the theoretical potentials $\boldsymbol{\phi}_0^{loc}$ in (4.2)) is decorrelated from the noise, then the expected target local GOF can be written as:

$$\begin{aligned} T_{GOF} &= \sqrt{1-\frac{\|\boldsymbol{\phi}_n^{loc}\|^2}{\|\boldsymbol{\phi}^{loc}\|^2}} \\ &= \sqrt{\frac{\|\boldsymbol{\phi}_0^{loc}\|^2}{\|\boldsymbol{\phi}^{loc}\|^2}} = \sqrt{\frac{\|\boldsymbol{\phi}_0^{loc}\|^2}{\|\boldsymbol{\phi}_0^{loc}\|^2+\|\boldsymbol{\phi}_n^{loc}\|^2}} \\ &= \sqrt{\frac{1}{1+\frac{\|\boldsymbol{\phi}_n^{loc}\|^2}{\|\boldsymbol{\phi}_0^{loc}\|^2}}} \end{aligned} \tag{4.3}$$

with $\|\boldsymbol{\phi}_n^{loc}\|$ the norm of the noise on the selected subset of sensors, $\|\boldsymbol{\phi}_0^{loc}\|$ the norm of the potentials generated by the dominant dipole and $\|\boldsymbol{\phi}^{loc}\|$ the norm of the measured potentials.

Considering the averaged SNR in dB $L_{SNR} \in \{\infty dB, 20dB, 10dB, 3dB\}$ (see also subsection 3.4.2), equation (4.3) writes also:

$$T_{GOF} = \sqrt{1/(1+r)}, \quad \text{with} \quad r = 10^{-L_{SNR}/10} \tag{4.4}$$

which gives $T_{GOF} \in \{1, 0.99, 0.95, 0.82\}$. This target GOF allows to set an interval in which the dipole we are looking for should fit the measurements. We have tested several intervals of the form $[(1-\alpha)T_{GOF} \quad (1+\alpha)T_{GOF}]$, with $\alpha \in \{0.05, 0.1, 0.2\}$. Among the 20 solutions given by the multi-start procedure and the local fitting on a subset of sensors, we should then choose the ones yielding a GOF_{loc} within the $[(1-\alpha)T_{GOF} \quad (1+\alpha)T_{GOF}]$ interval. Dipoles having local GOFs below the lower bound will then be eliminated. On the other hand, for low and medium noise levels (*i.e.*, $L_{SNR} \in \{\infty dB, 20dB, 10dB\}$), the upper bound of the previous defined interval is greater than 1, so it is useless, as no GOF can be > 1. For the $3dB$ noise level, even if $(1+\alpha)T_{GOF} < 1$, eliminating the dipoles having the local GOFs $> (1+\alpha)T_{GOF}$ does not improve the results. The explanations come from the way we defined the noise level L_{SNR}, which is a common noise level for all dipoles, regardless of their position with respect to the electrodes.

Consequently, it will in practice be lower for peripheral sources but higher for close to the sensors sources, which risk to be eliminated if we force a lower than necessary GOF. Based on this reasoning and on the simulation results, we have thus decided to use only the lower bound $(1-\alpha)T_{GOF}$ in the solution selection procedure, which will be done in two steps:

1. The solutions with high local GOFs ($GOF_{loc} > (1-\alpha)T_{GOF}$) are selected. Recall that the threshold T_{GOF} varies with the noise level (4.4).

2. Among the selected solutions based on this local GOF threshold, we select the solution for which the global GOF is maximal, *i.e.*, maximally explaining the whole set of sensors (in concordance with the dominant dipole hypothesis).

This two-step criterion, denoted Local → Global criterion in the following, describes the fact that a confident solution should explain its surrounding potentials, as well as the whole set of potentials in the dominant dipole case.

In order to have a complete picture of selection criteria, besides maximizing the local GOF_{loc} or applying the combined global/local strategy explained above, we also evaluate the performance when using the global GOF only, ignoring the local GOF used to optimize the dipole position. For the purpose of comparison, we also add in Figure 4.11 localization error boxplots when the localization is performed using the whole set of sensors (Global strategy, selection based on the (global) GOF).

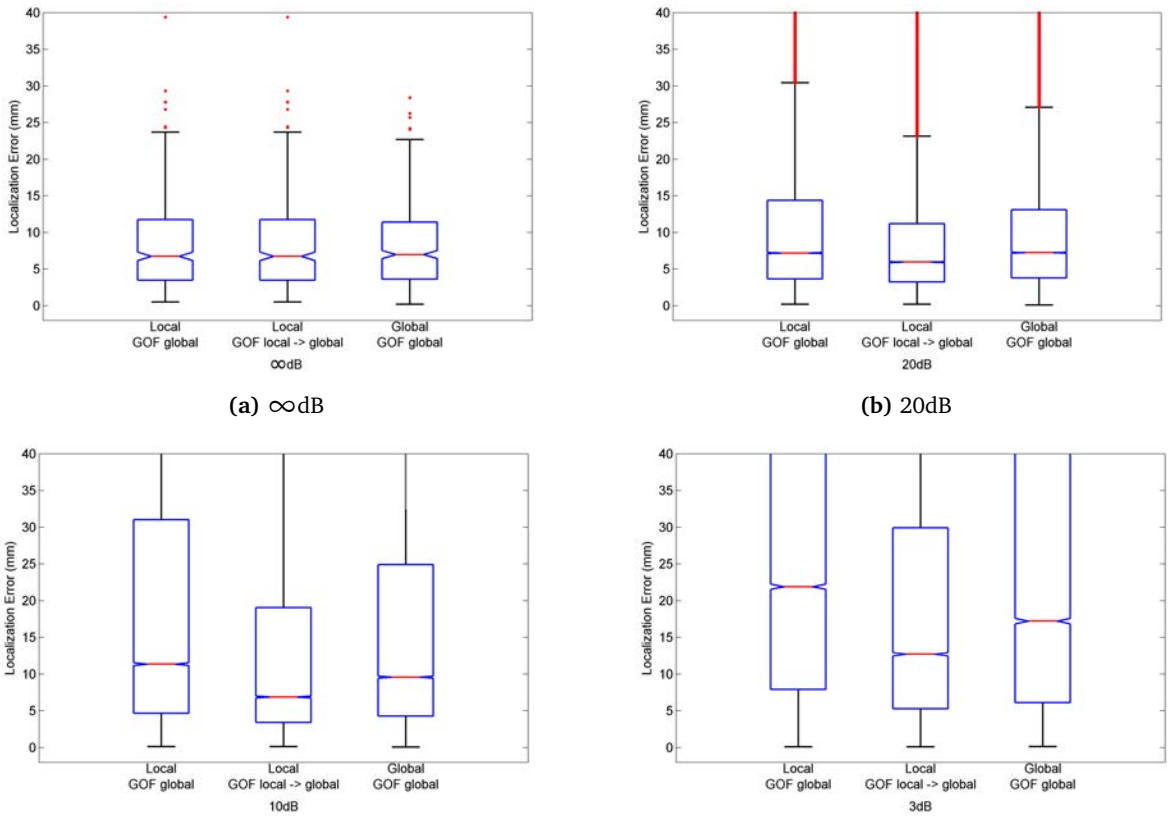

(a) ∞dB **(b)** 20dB

(c) 10dB **(d)** 3dB

Figure 4.11: Boxplots of localization errors when using various strategies for selecting the solution. From left to right: GOF global and mixed local → global GOF criterion when the local approach is used, GOF global when all the sensors are considered for the localization.

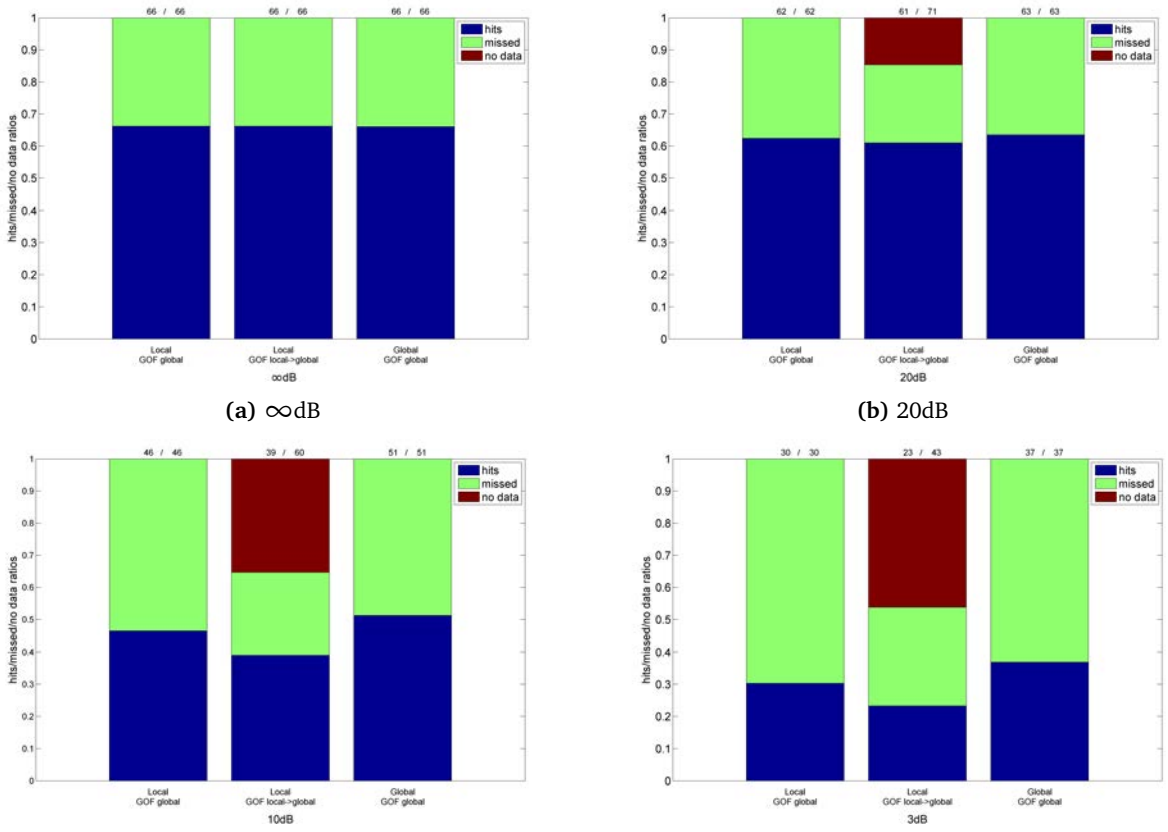

(a) ∞dB **(b)** 20dB

(c) 10dB **(d)** 3dB

Figure 4.12: Ratio of successful localization errors when using various strategies for selecting the solution. From left to right: *GOF* global and mixed local → global *GOF* criterion when the local approach is used, *GOF* global when all the sensors are considered for the localization. Two statistics are given above each stack bar. The first one is the percentage of hits with respect to the total number of dipoles (height of blue bar), the second is the percentage of hits with respect to the number of taken decisions (blue bar with respect to blue+green bars).

While a very similar performance is achieved in the no noise case, the proposed mixed criterion local → global indeed enhances the selection process in presence of noise. One can see that reduced medians are provided, compared to when the solution is picked based solely on the global *GOF*. The global localization approach (with global *GOF* selection) is also significantly outperformed in presence of noise. In particular, we observe that a robustness to noise is achieved, the medians slightly raising from 6.0 mm to 6.9 mm when the noise level increases from 20 dB to 10 dB, while it goes from 7.2 mm to 11.4 mm when the global *GOF* criterion is combined to the local approach, and from 7.2 mm to 9.6 mm when the global approach is used. Even in the 3 dB case, the local approach (with *GOF* global and mixed criteria) provides 1.2 cm localization error in median, while this of the global approach reaches 1.7 cm, and about 2.2 cm when the global *GOF* criteria is combined with the local approach.

However, these positive results, when the two-step selection is applied, have to be tempered. The analysis of the results can be done using stacked bars, as illustrated in figure 4.12. Indeed, a decision is not necessarily taken for each trial, as all of the 20 local *GOF*s are sometimes below the threshold (red bars for noisy cases (b), (c), (d)). The method renders a solution (blue + green bars) in 86.2% of the cases in the 20 dB noise configuration, 82.2% with 10 dB and 53.7% with 3 dB (100% in the no noise case). Among these solutions, the correct ones are represented by the central blue and green bars (Fig 4.12). Their percentage with respect to the total number of dipoles is given above each stacked bar (first value), while their percentage with respect to the taken decisions (blue + green) is

given by the second value. By making less decisions, the confidence of the localization results is improved as showed by the comparison between the two-step selection strategy and this based on the global *GOF* only (no local *GOF* pre-thresholding). The most glaring example is provided by the 3 dB case in which a decision is taken in about one case over only two (53.7%), but with a high median difference between the non-selective (Global *GOF* only) selection rule and the selective one based on the local *GOF*: a drop from a median of 2.2cm to 1.2cm is observed.

For this reason, and despite these encouraging results, we still feel that this selection is sub-optimal with regard to the theoretical performance that can potentially be achieved, *i.e.*, when the best solution is manually picked (see Section 4.2.1). This illustrates the limit of the *GOF* criterion and claims for the search of alternative approaches for the selection of the solution. We leave this question for further research, and in this thesis we limit ourselves to indicate some alternative directions in the two next sections.

4.2.3 Anatomical constraint

Given the difference remaining between the error boxplots when the best solution is selected (Figure 4.9) and when various selection strategies are applied (Figure 4.11), it clearly appears that making a decision solely based on *GOF* criterion fails in providing the best solution in a large number of configurations. Additional constraints need to be introduced to eliminate false positives and to provide reliable solutions.

When it comes to brain source localization, a common constraint is to consider that plausible solutions have to lie in the gray matter. Following the 1 cm acceptable error margin adopted in this work, we start by discarding the solution away from more than 1 cm of the gray matter (more precisely, distance of more than 1 cm to any point of the gray matter mesh). In the Figure 4.13, we provide localization error boxplots similar to those presented in Figure 4.11 with this anatomical pre-selection rule.

Based on this additional pre-selection rule, we can see that the medians are indeed significantly enhanced when compared to those of the previous section (Figure 4.11). The median in the 20 dB case now reaches 5.7 mm (while it was equal to 6.2 mm), and even the third quartile is below 1 cm, reaching 9.7 mm. In the 10 dB case, the median drops from 6.8 mm to 5.7 mm, and even in the strong noise 3 dB case the median is below the 1cm decision value, and equals 9.8 mm. These performances are obtained at the inevitable price of lower percentages of rendered solutions (see no data bars in Figure 4.12). Looking at the Figure 4.14 and comparing it to this of the previous section, we observe that the ratio of successful localization has been maintained (in particular in the 20 and 10 dB cases), and that the supplementary number of non-decision was related to mis-localized dipoles.

To sum up, the introduction of this constraint of plausibility maintains the ratio of true positives while reducing this of false positives. The ratio of true positives over the number of taken decisions (true positives+false positives) is indeed significantly enhanced in the presence of noise. The two-step local → global decision rule combined with this gray matter plausibility rule creates more confidence in the output of the algorithm.

4.2.4 Set of plausible solutions

Besides a completely autonomous methodology for ECD brain source localization, this thesis has been conducted with the ambition to provide practical tools at the direction of the clinician. With this perspective, we propose a localization scheme involving the clinician in the decision process. Instead of eliciting a single solution, we provide a set of plausible solutions among which the clinician can choose the most probable. Alternatively he can reject the

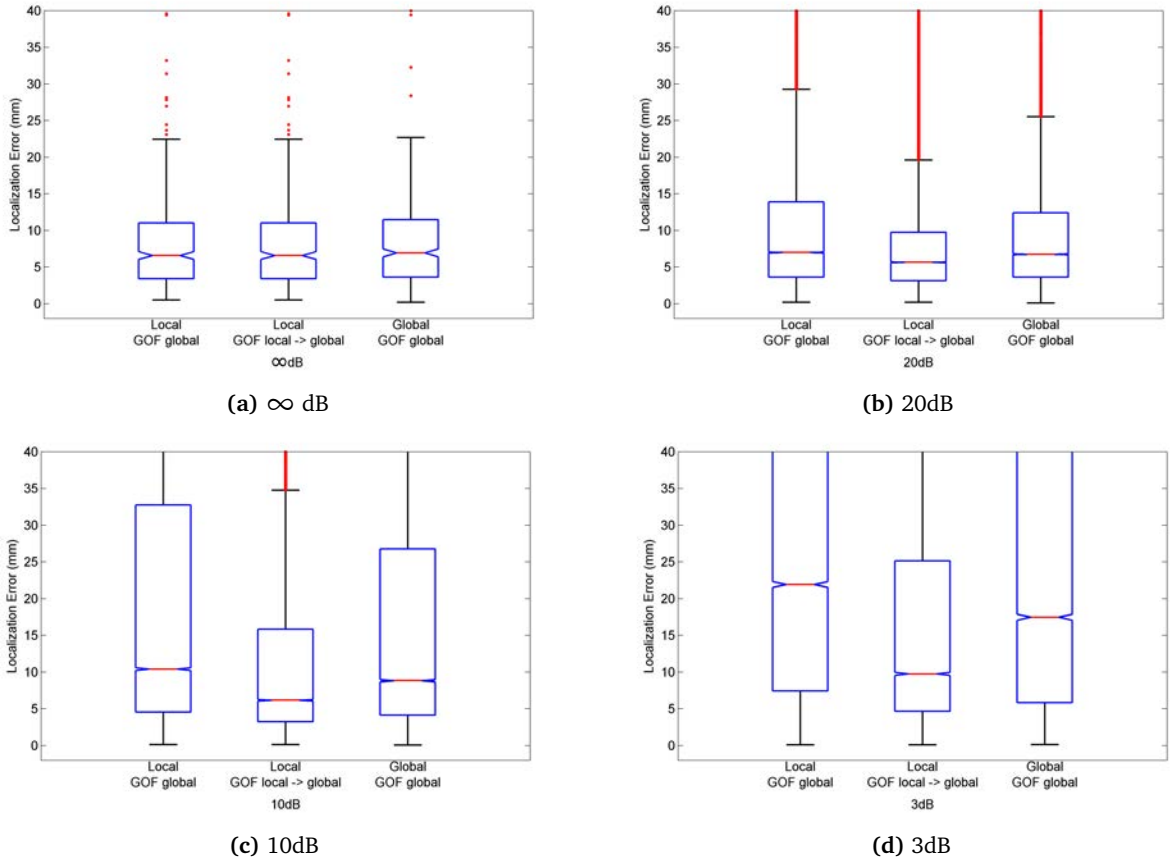

(a) ∞ dB **(b)** 20dB

(c) 10dB **(d)** 3dB

Figure 4.13: Boxplots of localization errors when discarding unplausible solutions (far from the gray matter), using various strategies for selecting the solution. From left to right: *GOF* local, *GOF* global and the mixed *GOF* local - *GOF* global criteria when the local proposed approach is used, *GOF* global when all the sensors are considered.

whole set of solutions if they seem globally erroneous and/or if he cannot make a decision. In the default case of an optimal automated selection strategy, such semi-automated approach avoids misleading the clinician by selecting a false positive, while the true dipole might be among the $N = 20$ found solutions.

The set of plausible solutions is built as follows: after discarding the implausible solutions (outside the gray matter), we apply a nearest neighbor strategy to merge the remaining dipoles between them: two dipoles are merged together if they are close of 1 cm or less. The resulting set of merged dipoles is finally considered and can be presented to a clinician for expertise.

Using this strategy, we question the confidence of the set of solutions that will be produced to the clinician. In Figure 4.15 the percentage of hits is given: a set is declared as a hit if it includes a dipole less than 1 cm distant to the true solution. In Figure 4.16 histograms of the number of solutions per set are given. We compare the results obtained using the local strategy without thresholding (Global *GOF* only), the local strategy with a thresholding based on local *GOF*s (noise dependent threshold values as defined earlier, and final decision based on the global *GOF*), as well as the global strategy (All configuration with maximum global *GOF* decision rule).

In the absence of noise, and comparing with the plausibility selection strategy proposed in the previous section, the number of set hits is increased in the local approach only while the score of 71% of hits is preserved for the global approach. This tends to prove that while the global *GOF* might be a relevant way to select the best possible

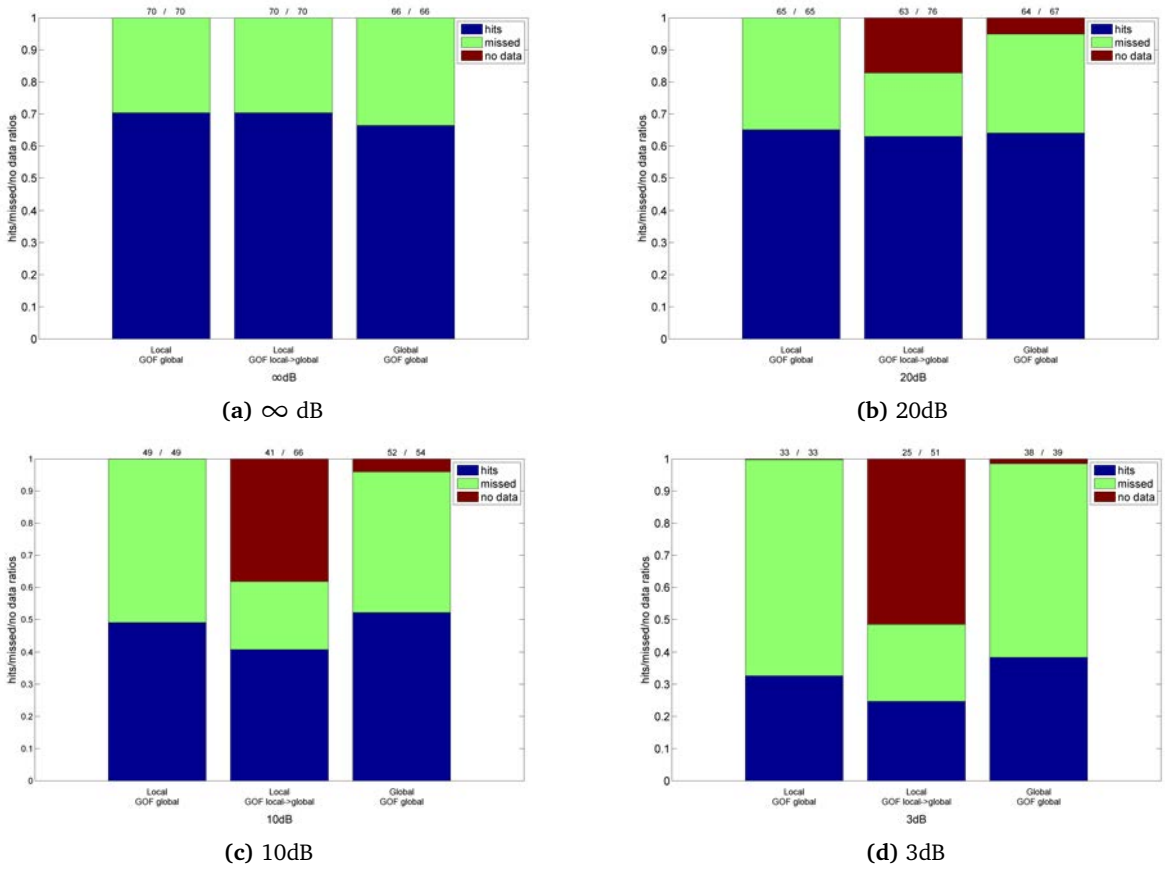

(a) ∞ dB **(b)** 20dB

(c) 10dB **(d)** 3dB

Figure 4.14: Ratio of localization errors when discarding implausible solutions (far from the gray matter), using various strategies for selecting the solution. From left to right: *GOF* local, *GOF* global and the mixed *GOF* local - *GOF* global criteria when the local proposed approach is used, *GOF* global when all the sensors are considered. As in Figure 4.12, the percentages of hits with respect to the (total number of dipoles)/(total number of taken decisions) are given above each stacked bar.

solution in ideal conditions (*i.e.*, the *GOF* is reliable when a large number of sensors is used for the localization in absence of noise), the selection based on local and/or global *GOF* in the local approach is sub-optimal and does not consistently provide the best solution. Looking at the histograms of the number of solutions per set, the local approach renders a higher number of dipoles, overburdening the final selection process. Besides, it appears that the local *GOF* thresholding has a limited influence on the selection process in this case, indeed, as mentioned above, the local *GOF*s are all very high in the absence of noise and are not discriminative.

When the noise is strong, as illustrated by the 3 dB case, a large number of distinct solutions are produced (about ten on average, both for the local and the global approaches). The global *GOF* is accurate in selecting the true positive when it exists using the global (All-sensor configuration) approach (hits ratio of 41% is maintained), while this ratio collapses from 39% to 33% with the local approach. Thresholding the dipoles using the local *GOF*s drastically reduces the number of candidates (a unique solution is produced in 47% of the cases, less than 5 candidates for almost all configurations). However the enhancement of hits ratio per set is limited when compared to the global *GOF* selection strategy (a slight increase from 25% to 28%, which is a weak ratio per se).

The gain of this set selection strategy is more relevant in a reasonable level of noise, for which the number of produced dipoles is indeed severely reduced by local *GOF* thresholding (about 4 dipoles on average in the 20 dB case and between 2 and 3 in the 10 dB case), while the ratio of hits and the relative ratio of hits (number of hits in

the total number of votes (hits+false positives)) shows appreciable increases. The first increases from 63% to 68% (respectively from 41% to 45%) in the 20 dB case (respectively in the 10 dB case), while the second goes from to 76% to 80% (respectively from 66% to 69%). The increase of both of these values is only 2% when no local *GOF* threshold is applied, showing the importance of this pre-selection.

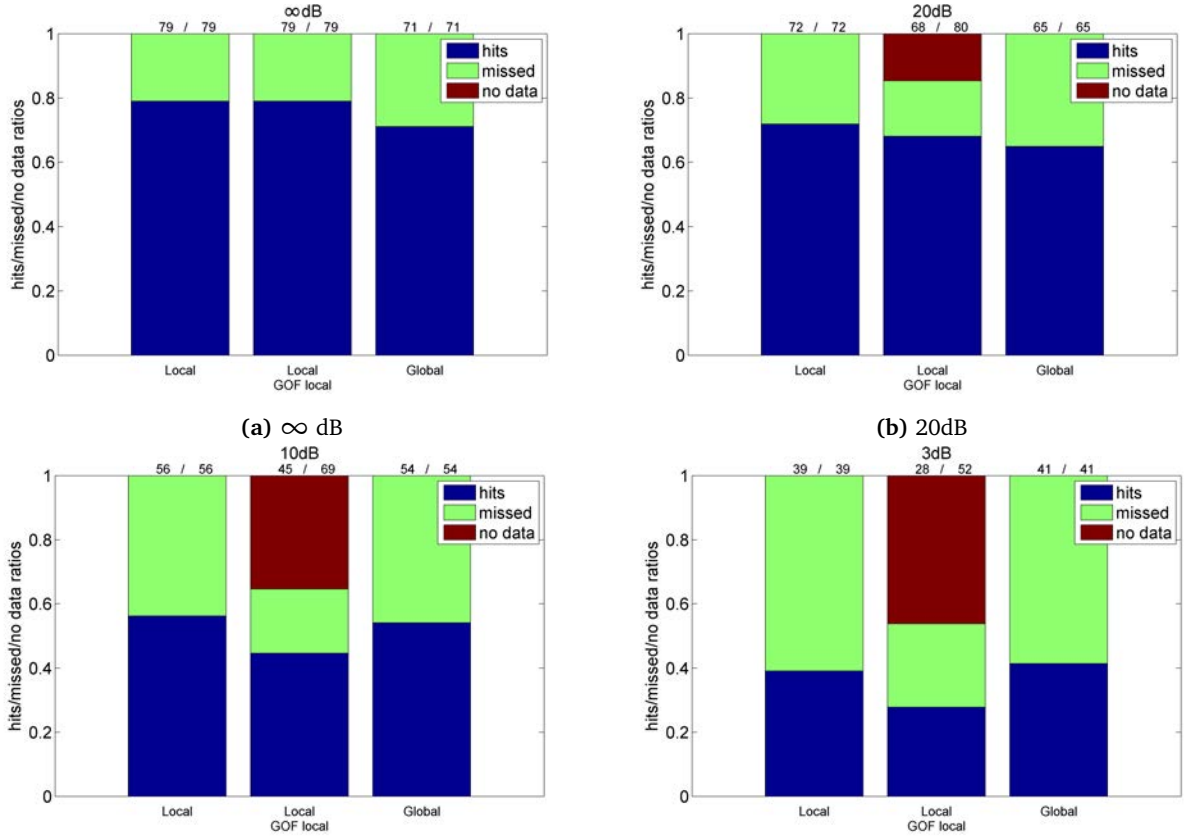

(a) ∞ dB **(b)** 20dB

(c) 10dB **(d)** 3dB

Figure 4.15: Ratio of hit set (containing a dipole less than 1 cm from the true dipole) when discarding implausible solutions (far from the gray matter). From left to right: local approach, local approach with thresholding based on local *GOF*, global approach. As in Figure 4.12, the percentages of hits with respect to the (total number of dipoles)/(total number of taken decisions) are given above each stacked bar.

4.3 Confidence map for SEEG dipole fitting

We pursue the objective to provide practical localization guidelines addressed to the clinician. We now quantify the level of reliability of the localization result when the retrievable dipole lies in a given zone of the brain. This aims to provide to the clinician a degree of confidence when facing a localization result within a given distance to the electrode, helping him in accepting or rejecting this result balancing between quantitative facts and his own clinical evaluation of the excitable epileptic area.

We delimit four different zones of the brain in terms of distance to the cloud of sensors. The first zone corresponds to a 2 cm envelope surrounding the set of sensors, *i.e.*, the brain area (fitted sphere area) with a distance of less than 2 cm from its closest sensor. The second zone is the outer envelope between 2 and 3 cm, the third zone goes from 3 to 4 cm, and the last zone is the remaining outer space with a distance of more than 4 cm from the sensors. The repartition of the 509 simulated dipole positions over these four zones is as follows (from the inner to the outer

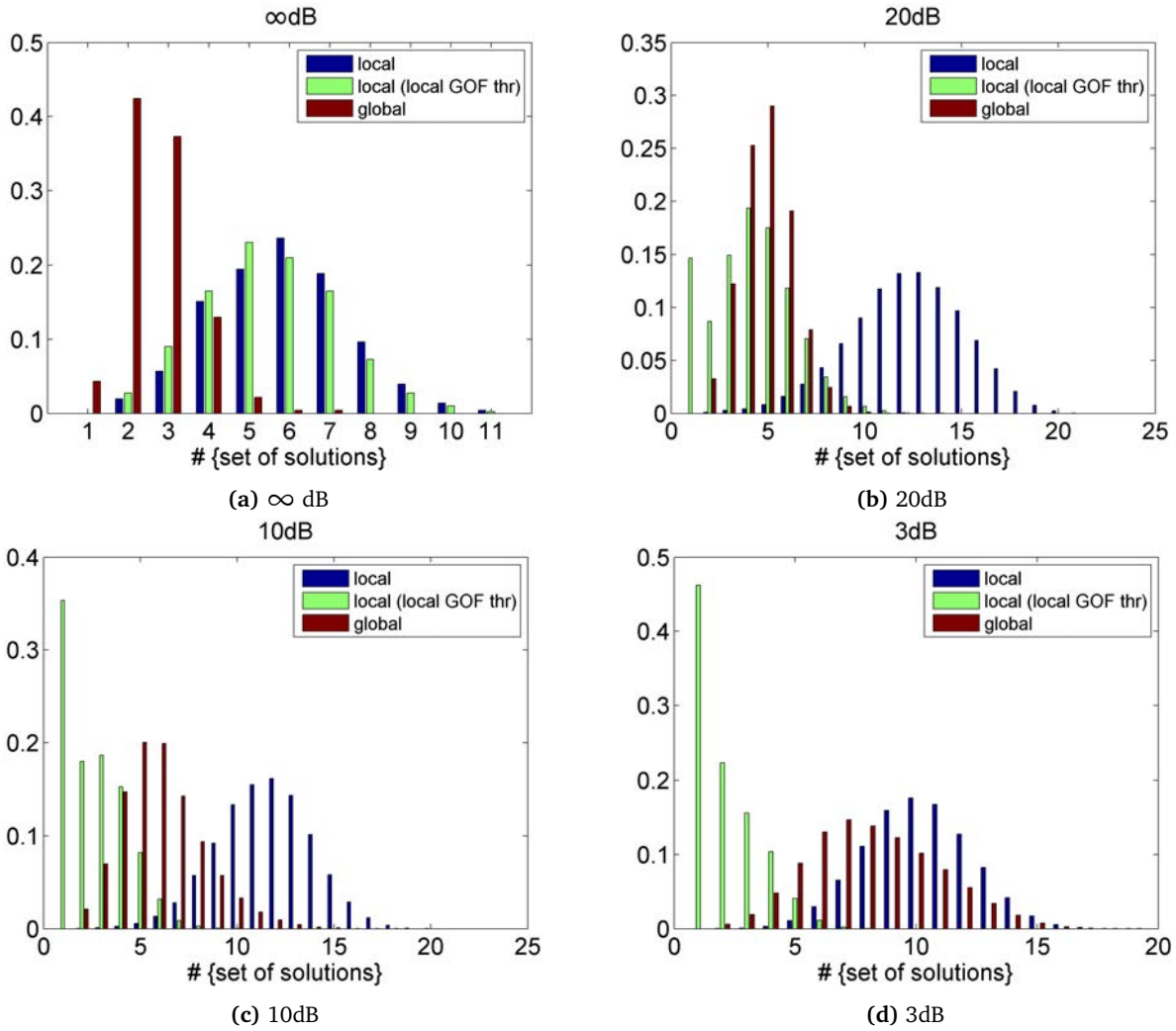

(a) ∞ dB **(b)** 20dB **(c)** 10dB **(d)** 3dB

Figure 4.16: Number of dipoles per set when discarding implausible solutions (far from the gray matter), using the local approach, the local approach with thresholding based on local *GOF*, and the global approach.

zone): 206, 122, 83 and 98. We evaluate the per zone reliability both when using the local and the global approach, considering the best localization result (manual selection), the result when a unique dipole is chosen (based on the local → global *GOF* criterion and the global *GOF* criterion respectively), and the subset selection strategy (using the local *GOF* thresholding strategy when the local approach is used). Please note that for all these different strategies the anatomical (gray matter) constraint is applied.

Considering the manual selection of the best dipole, we extract the hit rates (percentage of successfully localized dipoles belonging to the zone) and the false positive (FP) rates (defined as the number of false positives identified in a given zone over the total number of dipoles localized in this zone). These results are given in Table 4.1, and the high differences between the outcomes of the local and global approaches are marked in red when favorable to the Local approach and in blue when favorable to the Global approach (too low hit rates (under 50%) and too high FP rates (over 50%) being ignored). The hit rates are consistently higher when the local approach is used, while the percentage of false positives is consistently lower, confirming the theoretical superiority of the local strategy over the global one. This is especially the case when the dipole that is to be retrieved is at mid-distance from the electrodes (2 to 4 cm) in context of a reasonable noise condition. For example, in the 20 dB case, the hit rate drops from 95% to

		Local approach				Global approach			
Zones (mm)		0-20	20-30	30-40	40+	0-20	20-30	30-40	40+
∞dB	Hit Rate	99	99	93	48	96	83	45	4
	FP Rate	0	3	21	41	8	37	59	90
20dB	Hit Rate	98	95	69	20	95	81	36	5
	FP Rate	4	19	42	65	12	41	65	86
10dB	Hit Rate	93	74	24	3	90	62	13	1
	FP Rate	25	40	69	91	31	56	81	92
3dB	Hit Rate	78	36	4	0	77	35	3	0
	FP Rate	45	58	89	97	50	65	91	98

Table 4.1: Hit rates and the percentage of false positives zone by zone when the best solution is manually selected, both for the local and the global approach.

		Local approach				Global approach			
Zones (mm)		0-20	20-30	30-40	40+	0-20	20-30	30-40	40+
∞dB	Hit Rate	94	84	55	20	96	83	45	4
	FP Rate	10	31	47	66	9	34	50	90
20dB	Hit Rate	91	82	37	3	93	81	36	5
	FP Rate	18	28	31	51	14	36	58	86
10dB	Hit Rate	78	52	1	0	86	61	12	1
	FP Rate	29	27	66	100	35	51	77	92
3dB	Hit Rate	50	8	0	0	71	32	2	0
	FP Rate	40	43	95	100	53	60	89	98

Table 4.2: Hit rates and the percentage of false positives zone by zone when a unique dipole is selected using either the local (local → global GOF criterion) or the global (global GOF criterion) approach

81% and from 69% to 36% respectively for dipoles in the $20-30$ mm zone and the $30-40$ mm zone, while the FP rates increase from 19% to 41% and from 42% to 65% respectively. These hit rates tend to be similar when the noise level and/or the distance to the electrodes increase. For practical concerns, one can be confident in a localization result if the identified dipole lies within a distance from 3 cm from the electrodes in favorable context of noise (20 dB in the table), or within 2 cm with higher noise level (up to 10 dB). A careful examination has to be done when the identified dipole is more than 3 cm away from the sensors or when the noise increases.

Examining these statistics when a single dipole is selected based on *GOF* criteria (Table 4.2), the local approach loses its clear superiority over the global approach, emphasizing the lack of robustness of the *GOF*-based choice criteria. In some cases the hit rate is even far higher with the global approach when the noise level is high (10 dB case, emphasized in blue in the table). The local approach, however, keeps rendering lower FP rates, mainly due to the local *GOF* thresholding applied in the local → global selection strategy, at the cost of lower hit rates. Besides, the same conclusions apply here in terms of a reliability zone, *i.e.*, a localization result can be trusted if it lies within a 30 mm distance from the sensors in a reasonable level of noise (20 dB), or within a 20 mm distance in stronger noise environments (10 dB), but unsurprisingly becomes more and more questionable when found with the largest distance from the sensors and/or when the noise level increases.

Finally, we evaluate the per zone reliability of the localization procedure when sets of plausible dipoles are taken

as the output of the localization procedure (Subsection 4.2.4). Again two statistics are computed, the first gives the ratio of sets containing a well localized dipole ($\text{hit}_{\in \text{set}}$ ratio) and the second the average number of produced false positives per zone (# FP). Analyzing the results of Table 4.3, it appears that the hit ratio for the global approach is equal to those obtained when manually picking the best dipole (Table 4.1), meaning that all the well localized dipoles are indeed selected when using this subset procedure. Unfortunately, this is not the case for the local approach, as the local *GOF* thresholding strategy adopted to limit the amount of false positives tends to eliminate relevant solutions. As explained in Subsection 4.2.4, the local approach tends to produce a relatively high number of false positives when the noise level is favorable (∞ dB to 20 dB), however, it succeeds in providing a high ratio of successfully localized dipoles in zones close to the sensors (up to 30 mm), and it outperforms the global approach while still producing less than one false positive per set on average. When the noise level decreases, both approaches show a similar performance, and the localization outcome becomes less and less confident.

In summary, all these tables indicate that we can trust the outcome of a localization procedure if the SNR is favorable enough and if the dipole is localized closely enough to the set of sensors, with a balance between these two parameters. With a 20 dB noise level, sources can be identified up to 3 cm away from the sensors, this distance reduces to 2 cm in the 10 dB case. Practically, this means that if a dipole is found away from these inner zones, the result has to be criticized carefully. In these ranges of dipole to sensor distances and noise levels, the local approach and global approach are giving similar results when trying to select the solution from *GOF* criteria (Table 4.2), which stands as a frustrating result when looking at the significantly higher performance obtained for the local approach when the best solution is manually chosen (Table 4.1). A compromise can be found by opting for the subset selection strategy, indeed preserving a high rate of successful localization when using the local approach at the cost of a necessary (clinical) manual selection if several solutions are rendered. Considering the rather low number of false positives that are produced by the method, this might be a relevant strategy employing both objective solutions extracted from the data and the neurophysiologic expertise of the clinician.

If we consider the case of a favorable noise level (20dB averaged SNR in this thesis), the zone within which the sources can be identified goes up to 3 cm, including 328 of the 509 simulated positions. Considering that these positions are determined by a regular sampling of the gray matter mesh, it suggests that about 65% of the brain is covered by the realistic SEEG implantation adopted all along this thesis (nearly 90% of the dipoles identified in this area vs about 25% of false positives among the identified sources in this area). Besides, it means that if any point of a region of interest is less than $3cm$ away from a sensor, and if a favorable noise level (20dB case) can be guaranteed by the pre-processing step (basically by averaging several events), then we can put confidence in the localization procedure. This distance is reduced to $2cm$ when the achievable noise level is less favorable (10dB case), *e.g.*, when the observed event is of a weak amplitude.

4.4 Application on real signals

This last section aims to verify the previously presented arguments and simulation results on real signals. The first subsection considers that the position of the source to be localized is known and evaluates the localization performance as a function of the number of employed sensors/ radius of the neighborhood. This needs of course a known source, and for this we use the epileptic spikes already studied in the previous chapter, for which the position of the dipole is known.

		Local approach				Global approach			
Zones (mm)		0-20	20-30	30-40	40+	0-20	20-30	30-40	40+
∞dB	$hit_{\in set}$ Rate	97	91	69	35	96	83	45	4
	#FP	0.87	0.86	0.78	1.04	0.43	0.22	0.12	0.24
20dB	$hit_{\in set}$ Rate	97	90	46	4	95	81	36	5
	#FP	0.83	0.44	0.13	0.04	0.43	0.22	0.14	0.19
10dB	$hit_{\in set}$ Rate	86	39	1	0	90	62	13	1
	#FP	0.65	0.10	0.01	0	0.85	0.37	0.19	0.11
3dB	$hit_{\in set}$ Rate	57	9	0	0	77	35	3	0
	#FP	0.50	0.03	0	0	2.13	0.49	0.15	0.07

Table 4.3: Results using the "Set of plausible solutions" strategy of section 4.2.4. Hit rates and average number of produced false positives zone by zone.

The second and the third subsections evaluate the local method proposed in this chapter (Section 4.1), again on real SEEG measurements. The employed signals are the same as those already used in chapter 3, *i.e.*, intracerebral stimulations (ICS) and interictal epileptic spikes.

4.4.1 Proof of concept: localizing with a local subset of sensors

The same data as described in Subsection 3.5.2 are used. As mentioned above, we first evaluate the opportunity to reduce the set of sensors within a given distance to the source of interest, such as evaluated under simulations in Subsection 4.1.2. We considered 9 different sensor subsets, by increasing the sphere radius containing the sensors, centered on the assumed source position R'6. The first configuration contains the 10 closest sensors, those within a sphere of radius 1.5cm. We then increase the radius by steps of 5 mm to define the next configurations, increasing thus the number of used sensors, until including the whole set of 90 sensors (recall that for this patient all sensors were placed in the left hemisphere). 5.5cm configuration was not included because it contained mostly the same sensors and presented similar results on preliminary simulations. In parallel, we evaluate the cross influence of the SNR by averaging an increasing number of spiking events. As mentioned in the previous chapter, 20 spikes have been identified by a trained expert. For each peak, the time instant of its highest value was retained. We then select, on each sensor, k instants among the 20 (with $k \in \{1, 2, 3, 5, 7, 10, 15, 19, 20\}$) and average these k recorded potentials. Localization has been performed on 100 random combinations of k among 20 (except of course for $k = 1$ or $k = 19$, when only 20 combinations are possible, and for the single combination for $k = 20$) and the localization errors were averaged. Following the definition of SNR adopted in this thesis in Subsection 3.4.2, we have estimated the SNR for each combination of k spikes. The signal power is computed as the power of the averaged potential at the instant of the spike, while the noise power is estimated using a window of signal appearing 1s to 5s after the spiking time windows, by averaging k values randomly chosen in this window. The respective estimated SNR for $k \in \{1, 2, 3, 5, 7, 10, 15, 19, 20\}$ are the following: $\{-3.3, -2.4, -1.0, 1.1, 2.7, 4.2, 6.3, 7.0, 7.3\}$dB). From these values, this might appear to be a difficult localization context when considering the results obtained under simulation in the 3dB case. However the spiking events of interest (supposed to be located in R'6) are $\sim$ 12.5mm distant from the closest sensor (the sensors of R' excluded). Under simulation, most of the dipoles located under $2cm$ from the closest

sensor had indeed an individual SNR well over 3dB. We can then expect successful localization result considering a sufficient number of spike averaging k.

Figure 4.17 shows the obtained localization error with respect to sensor $R'6$ considering the 9 different sensor subsets, for each amount k of averaged spikes (after averaging over their respective 100 sub-averages). The results confirm that a minimum amount of sensors with good spatial disparity is needed. In this experiment, the 16 sensors situated below 2 cm from R'6 belong to two parallel electrodes, explaining the bad localization results, whatever the number of averaged instants k.

It is straightforward to see that increasing the SNR by averaging more spike events indeed enhance the localization accuracy. When enough spikes are considered, (10 in this example, SNR of 4.2dB), the localization is robust to the inclusion of additional sensors in the subset. But when the number of available spikes is low for averaging, this example case illustrates that an adequate sensor configuration close to the source has to be chosen. In this particular experiment, a good trade-off (localization error below 1 cm) is obtained by averaging 5 to 10 spikes (1.1 to 4.2dB) on a subset of 24 sensors within a radius of 2.5 cm around the source position.

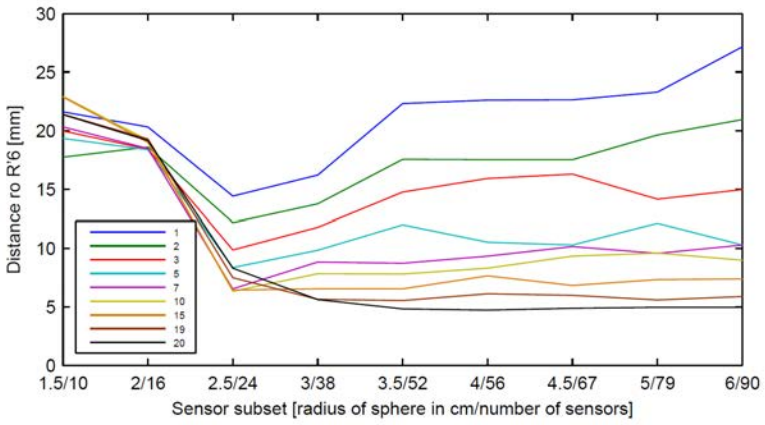

Figure 4.17: Estimated position (distance to $R'6$) vs subset of sensors. Each curve represents a given amount of averaged spikes (mean of 100 subaverages).

We do not present them here, but sensibly the same type of curves are obtained for the ICS spikes, with the notable exception of the most peripheral stimulation (TB'8-9), for which increasing the size of the neighborhood worsen the results even when we average a great number of spikes (see results with **all**-configuration in subsection 3.5.1).

4.4.2 Local approach on ICS

We now evaluate our local sensor subset strategy on real data of ICS, for which the position of the source is known. We consider here only one of the three electrical stimulation sites used in Chapter 3, section 3.5.1, the most difficult to localize (TB'8-9, situated close to the brain frontier). The other two ICS sites were indeed well localized also when using the **all**-sensors configuration, while the localization of the most external one failed when using too far away sensors (see figure 3.16 and table 3.4).

The instants of the stimulations were detected as described previously and the localization results using **all** and **ipsi** configurations were compared to the results using the proposed local approach. To separate the localization performance from the solution choice problem (among the multi-starts), only the Oracle (best) results for each

approach were considered for a first analysis. As in the previous subsection, we also evaluated the joint influence of the SNR by averaging more and more ICS spikes (from the 62 detected spikes, we chose $k \in \{10, 20, 30, 40\}$ spikes at random and averaged measurements between these spikes for each sensor; 10 random combinations of k among 62 were next considered for the box-plots in figure 4.18).

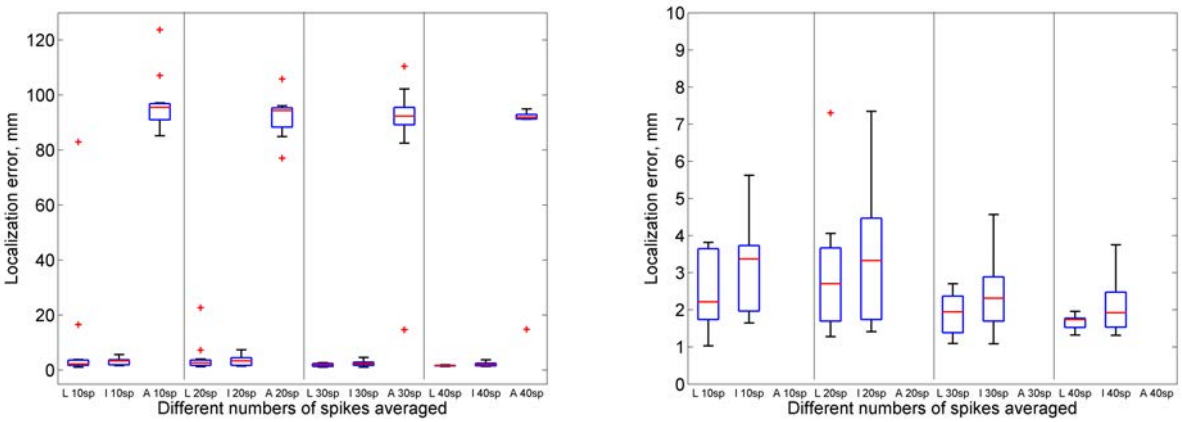

(a) **(b)**

Figure 4.18: Localization results on ICS data using different numbers of stimulation spikes in the averaging (*i.e.*, different SNR, one for each column). The number of averaged spikes varies in $\{10, 20, 30, 40\}$. We compare the local approach (L), the ipsi-lateral configuration (I) and the all-sensors configuration (A). Figure a gives the general picture, whereas b shows a zoom to better compare Ipsi and Local approaches.

As we can see in Figure 4.18, the local approach clearly works better than using all sensors (which was expected, as the ipsilateral configuration is a particular, medically guided, local approach). Although there are some separate outlier cases when using all sensors that yield lower localization errors, they are always above 1cm.

Comparing now our local and the medically guided ipsilateral approaches (figure 4.18(b)), we can conclude that our local approach potentially yields better results than the ipsilateral approach, with a more marked difference for low SNR (*i.e.*, reduced number of ICS spikes considered for averaging). Of course, better SNR (more spikes) improves both local and ipsilateral approaches in terms of medians.

In order to evaluate the selection procedure among choosing the highest GOF_{loc} (evaluated on the subset of sensors used for the localization), the highest GOF_{glob} (*i.e.*, computed on all available sensors, even if the localization is performed on a subset) or the two step procedure described in subsection 4.2.2, we also plot in figure 4.19 the performances of all evaluated localization procedures (including the final selection step) for different SNR/ number of averaged ICS spikes. Again, the global picture is given in subfigure (a), while a zoom on the best approaches is given in subfigure (b). As we have used the most external ICS, the error obtained using all sensors and choosing the final solution among the multi-starts based on the global GOF yields the worst results. At the opposite, the use of a local subset followed by an Oracle choice yields constantly the best results, even for low SNR. Note that the Oracle can be seen as a choice made by a specialist after presenting the (at most) 20 multi-start solutions, see subsection 4.2.3. Unfortunately, among the 'automated' GOF based choices, only the GOF computed over the whole set of ipsilateral sensors combined with the ipsilateral localization yield localization errors below 1cm. The local GOF_{loc} with local approach is the next best, but even for rather good SNR (40 averaged spikes), the error is still about 15mm. The two step approach, based on the combination between local and global GOFs after using a local

subset for localization is clearly misled by the low performances of the global (**all**-sensors) approach. These deceiving results are in fact explained by the non-fulfilling of one of the important starting hypothesis, *i.e.*, the dominant dipole. Indeed, when analyzing the SEEG signals for the external ICS, one can observe (see figure 3.15) that high amplitude regular activities appear in the opposite hemisphere (mainly on electrode H), indicating the existence of at least an additional important active source.

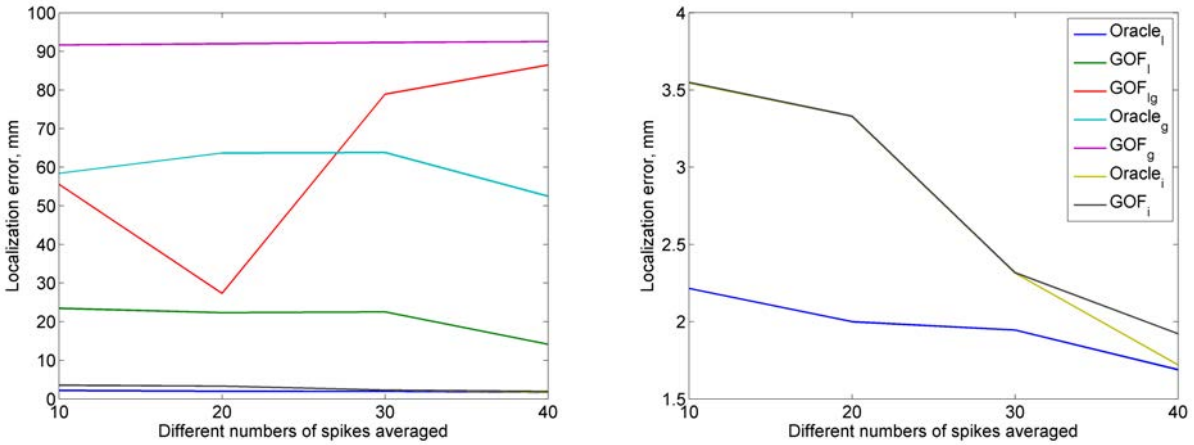

(a) All criteria **(b)** Zoomed best criteria

Figure 4.19: Localization results on ICS spikes using different numbers of spikes in the averaging (*i.e.*, different SNR, one for each column). The number of averaged spikes varies in $\{10, 20, 30, 40\}$.

4.4.3 Local approach on real epileptic spikes

Finally, this last subsection aims to validate or evaluate the localization performances of the different approaches (sensor configurations + final choice) on real epileptic spike data. The data used was the same as described in Subsection 3.5.2.

The analysis follows the same steps as in the previous subsection: first comparing the Oracle solutions for the different subsets, next introducing the choice problem. It is important to recall that the tested patient was only implanted in the left hemisphere, so no **all** configuration could be evaluated. So we take all the available sensors but they correspond to **ipsi** configuration.

Before applying the localization methods, the 20 most distinct spikes on $R'6$ sensor were selected (after the spike selection as done before in the previous chapter). Afterwards, combinations of these spikes were tested varying the number of spikes (k among 20), in order to evaluate the SNR effect. As in the first subsection above (subsection 4.4.1), we evaluated the localization procedures on 100 random combinations of k among 20. The boxplots for some specific k values ($k \in \{1, 5, 10, 15\}$) are given in figure 4.20.

The results confirm the ones observed on ICS spikes: localizing with a local subset is in principle more performant than using all available sensors, here the ipsilateral ones. The differences between the two procedures are more important for low SNR (when the local approach is clearly better than the ipsilateral one), but they remain significant for better SNR (15 averaged spikes, $\sim$ 6.3dB), when the local approach has a median well below 1cm, unlike the ipsilateral. This good median localization performance is in fact obtained also for a lower SNR (10 averaged spikes,

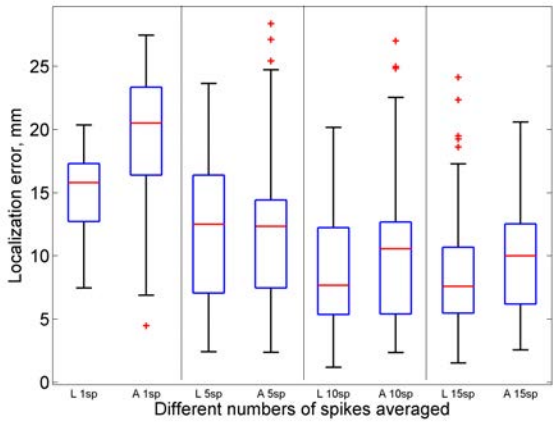

Figure 4.20: Localization results on epileptic spikes using different numbers of spikes in the averaging (*i.e.*, different SNR, one for each column). The number of averaged spikes varies in $\{1, 5, 10, 15\}$. We compare the local approach (L), the ipsi-sensors configuration (I).

$\sim$ 4.2dB). Recall that these results are obtained using an Oracle choice among the 20 or less obtained solutions (both for the local and the ipsilateral configurations).

The effect of the automatic *GOF* based choice is illustrated in figure 4.21, which shows the median results of repeated (100 times) application of localization methods (the only variables here being the different spikes selected and the initialization points of the localization).

As before (see figure 4.19), the local configuration plus the Oracle choice is systematically better than the other solutions, including the ipsilateral Oracle, and it passes below a 1cm error starting from 6 averaged spikes. Using other subsets (local or ipsilateral) and selection strategies (local, global or combined local→global) yield worse results (medians above 1cm, except when averaging on all or almost all the spikes), with rather few differences among them, except for the local *GOF* based choice (green curve in subfigure (a)), completely misleading.

Finally, the SNR effect is as expected, the more spikes we average, the lower the localization errors, all methods considered.

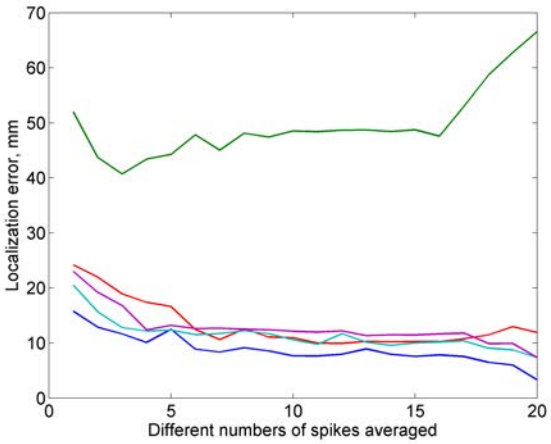

(a) All criteria

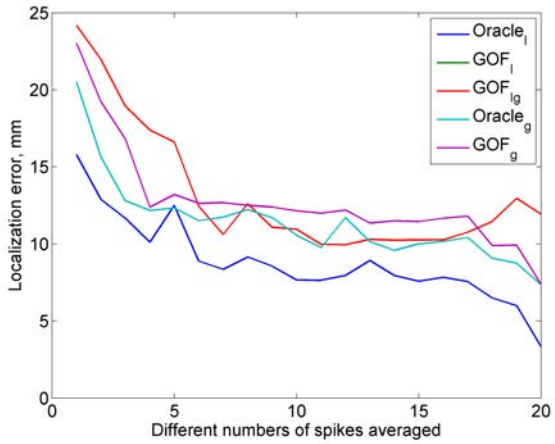

(b) Zoomed best criteria

Figure 4.21: Localization results on epileptic spikes data using different sensors subsets (ipsi, index g vs. local, index l) and selection strategies: Oracle vs. maximization of the GOF, evaluated on the local subset (GOF_l), on ipsi sensors GOF_g or using the combined strategy introduced subsection 4.2.2 (GOF_{lg})

4.5 Conclusion

In this last chapter we propose a local approach for dipolar brain source localization, based on an iterative selection of the closest sensors to the current solution at each step of the optimization. This selection relies on an original spatial conditioning criterion explicitly taking into account a well balanced repartition of the sensors in space. It also implicitly guarantees a sufficient number of recruited sensors to carry out a successful dipole fitting procedure. We have demonstrated under simulation the superiority of this approach over the global one (*i.e.*, when all the sensors are recruited), the median of the localization errors is significantly reduced when the best solution is picked among the set of final solutions, in the no noise case as well as in favorable conditions of correlated noise. However, the automatic selection of these best solutions based on classical GOF criteria shows its limits and renders suboptimal performance. To avoid this drawback we propose a two-step selection scheme where we start by discarding the solution with too low local GOF (the measurements around the solution are not well explained) and by selecting the best global GOF among the remaining solutions (under dominant dipole hypothesis, the solution should explain a large portion of the measurements). In favorable conditions of noise, this approach does indeed enhance the ratio of true positives while limiting the ratio of false positives.

Nevertheless, numerous valid localizations are still lost through this selection procedure. As an alternative, and with the objective to propose practical tools at the direction of the clinicians, a set of eligible solutions is produced and the final choice is left to the expertise of the clinician. This avoids the discarding of successful localization due to the selection of an erroneously high (global) GOF. In order to help the clinician to decide or to discard the localization outcomes, we also evaluate the reliability of the produced solutions with respect to their distance to the set of sensors. In favorable conditions of correlated noise (corresponding to a level of noise from 20 dB to 10 dB as defined in this thesis), confidence can be put in an identified dipole if it lies closer than 3cm away from a sensor (respectively about $2cm$ for 10dB). This helps in identifying zones of confidence (depending on the level of noise), and to criticize the relevance of a given solution to put in balance with the expert priors on the location of the source to be identified.

These findings under simulated data are concordant with the results obtained on real data. Especially in the case of ICS data, a case of particularly high SNR, the site of the stimulation is consistently found while using a local set of sensors, or even the set of ipsi-lateral sensors to the source. We face a more delicate case study when the site of interictal spikes is to be identified. First, it appears that enhancing the SNR by averaging is mandatory for a relevant solution to be produced. Averaging over 20 events allows to enhance the SNR from -3.3dB to 7.3dB, still representing a case of rather low signal to noise ratio. However, the source being distant from less than 1cm to the closest sensors, it is successfully localized in most sensor configurations. When fewer events are averaged (lower SNR), the best localization results are indeed achieved when using a limited number of sensors surrounding the epileptic source (as identified by the expert) by using our sensor selection strategy.

From this analysis, several questions are raised and might be the object of promising future research. To begin with, a better criterion than the GOF needs to be found for accurate solution selection. Also, the identification of zones of confidence inversely poses the question of a guided implantation of the sensor setup, guaranteeing that all the brain volume, or at least all points of a region of interest, are identifiable with respect to this sensor setup, *i.e.*, each point of the region of interest lies within a given distance to the set of sensors given an acceptable level of noise.

Conclusion and perspectives

Summary of the thesis

Stereo-electroencephalography (SEEG) is a cutting-edge diagnostic tool explored by neurophysiologists and neurosurgeons as part of the presurgical evaluation. This electrode setup is implanted in the deep brain structures depending on the localization of the suspected epileptogenic zone rumored to be responsible of the epileptic seizures. They can precisely characterize the electrical activity of these structures, detecting patterns of electrical abnormality that can help in delimiting more precisely the seizure foci. Moreover, in the context of pre-surgical evaluation, intracerebral electrical stimulations are applied to assess the localization of functional areas such as memory visual recognition ... These intracerebral electrical stimulations represent for us exogenous sources perfectly all parameters are known they are therefore spatially and temporally deterministic. These stimuli can be explored to evaluate the performance of inverse problem solving by different methods and algorithms. While this modality is restricted to the exploration of the very local structures within which they are implanted, the objective of this thesis is to broaden the field of vision and of application of the SEEG. In particular, these measurements give access to deeper recordings of the brain activity and are closer to the generators of interest, thus providing a promising tool toward more precise reconstruction of the brain electric map of the region of interest. However the particular implantation of this setup in comparison to scalp EEG measurements raises questions about the feasibility of such brain source localization from SEEG and calls for an analysis of the favorable conditions giving rise to reliable localization results.

We adopt the assumption of a dominant source, a situation often met when considering interictal spike events. An over-determined non-linear problem is then to be solved. The resolution is based on a classical Sherg's Equivalent Current Dipole fitting approach solved using Sequential Quadratic Programming. Using such basic resolution scheme, several decisive aspects of the source localization problem are analyzed, to begin with the influence of the forward model on the accuracy of the source localization results. In this context of intracerebral recordings where the brain tissue conducting the electrical fields from the source to the electrodes share conductivities of equivalent order (relatively to the very low conductivity of the skull bone), we evaluate the opportunity to explore simple analytical model in comparison to a heavy numerical FEM model. While we found out that an Infinite Homogeneous Medium model (IHM) provides insufficient modeling precision, a One Sphere Medium model however brings satisfactory estimation of the lead field projection coefficients in the direct vicinity of the source. Indeed this model takes into account the main propagation barrier, *i.e.*, the skull bone, and brings sufficient accuracy with respect to the targeted localization precision of few millimeters.

Based on the extended simulations presented in the **chapter 3** (509 dipoles are homogeneously spread over the gray matter mesh and their projections are computed based on a FEM model considering the three Cartesian orientations), we then evaluate the precision of the localization with respect to a standard SEEG configuration classically

met in clinical routine: 9 needle electrodes or multi-sensors (139 sensors) are implanted in the right hemisphere suspected to hold the epileptic foci, while 3 electrodes of control are implanted in the opposite (contra) left hemisphere. From our experiments, at least a dozen non-coplanar sensors are necessary to reach the 1cm localization precision, and should be positioned close enough to the source of interest within the same hemisphere. A source positioned in an unexplored hemisphere cannot be localize due to the approximation of the forward model. Besides, the addition of supplementary sensors do not necessarily enhance the localization precision, in particular when these sensors belong to the opposite hemisphere. This is illustrated by the results obtained when the ipsi lateral sensors (with respect to the source) where used compared to when all the available sensors where recruited in the localization procedure. These observations are further confirmed when coherent noise of disturbance sources are added to the measurements. The recruitment of local electrodes is likely to reduce the uncertainties and to regularize the inverse problem, however it appears that choosing the ipsi lateral sensors do not guarantee to reach better localization robustness. This selection of local sensors has to be adapted for each particular case of source location.

To this end, a method for ECD localization based on local measurements is proposed in the **chapter 4**. A genuine selection procedure is introduced controlling the balance between spatial repartition of the sensors, their numbers as well as spatial extent, based on a spatial conditioning criterion. The theoretical superiority of this local approach is proved under simulations, however the optimization still relies on a multi-start strategy and this local approach tends to produce several distinct points of convergence. The selection of the best solution among these points is a difficult task improperly carried out by the classical goodness of fit (GOF) criteria. A decision strategy based on several GOF (computed separately on the local set of recruited sensors and on the whole set of sensors) indeed limit the number of false positives at the price of true positive rejections. As an alternative, a decision scheme involving the clinician in the decision process is drawn, indeed increasing the ratio of potential successful localizations. In a clinical perspective, this is also a way to involve the expert in the decision process. To assist him in the decision, we also provide reliability zones within which an identified dipole can be trusted. These zones go up to 3cm away from the set of electrodes when the SNR is favorable, meaning that the use of the SEEG modality can be indeed broaden from its original hyper-local role (under bipolar montage) and used to reconstruct the activity of mid-distant cerebral structures.

In both chapters and conclusions our hypothesis are confronted to real data collected at the CHU of Nancy. In the **chapter 3**, the feasibility of SEEG brain source localization in real environment of source and measurements is demonstrated on data set of intracerebral stimulation, and on a case of real interictal spikes related to a temporal lobe epileptic patient. These experiments are deepened in the **chapter 4**, the effect of the pre-processing step aiming at increasing the SNR of the activity of interest is illustrated, showing that in context of relatively low SNR a subset of local sensors indeed provides the most reliable localization results. The extent of used sensors is limited to a sphere with radius between 4 and 5cm, corroborating the results obtained under simulations. Blind source localizations are then carried out on the same set of data using the proposed local approach, confirming the location of the suspected epileptic foci as identified by the neurophysiologists during the preoperative clinical evaluation.

Discussion and Perspectives

It can be argued that the use of over-simplistic analytical forward model inevitably leads to sub-optimal localization results, however we insist on the balance between on the one hand the weight of the forward model computation

(in terms of necessary anatomical data as well as computation resource) and on the other hand the expected gain in localization accuracy. Nevertheless a better compromise might be achieved by adopting a Boundary Element Method model (BEM) interpolated in each measurement point based on the potentials evaluated on the surface of each considered boundaries. In particular this might better take into account the real shape of the non-spherical skull bone, yielding more precise localization of sources close to the skull border, while keeping the computational cost within reasonable bounds. It has been demonstrated that more sophisticated FEM model are not needed for the wanted precision in clinical application and that such modeling brings similar localization results [Birot et al. 2014].

From a signal processing point of view, the importance of the pre-processing step has been demonstrated to be a pre-requisite for successful localization results. Beyond the re-referencing procedure and the basic averaging step presented in this thesis work, an extended study of the influence of source separation techniques and signal subspace identifications such as carried out in Romo Vasquez *et al.* [Romo Vazquez 2010] might be of great interest.

The Goodness of Fit (GOF) widely used as the criterion for final solution selection has been demonstrated to work very poorly in a wide range of situations. Alternative criteria are then to be explored, to begin with criteria based on correlation in place of least squared objective function. Indeed forward models are likely to introduce spurious offset on the estimated sensor potentials, artificially decreasing the GOF. To avoid such effect and put the accent on the spatial repartition of the potentials in place of an exact potential matching on the sensors, one might consider target function based on correlation of the actual potentials with the estimated one, also avoiding the scaling effect due to an improper estimation of the brain matter conductivities.

The basic ECD inversion scheme adopted in this work, as relevant as it is to evaluate the brain source localization feasibility independently of any large set of parameters usually involved in more complex inversion method, quickly find its limits when several sources are simultaneously active. For this reason, one might be interested in distributed models where the set of observed potentials is regressed on a large number of source candidates. These methods are relevant when several co-occurring sources are to be identified, and can be regularized by introducing probabilistic prior information on the suspected locations of the sources as well as sparse constraint to avoid the spread of the solutions over a large number of dipolar elements. Such methodologies are currently explored in the team ESPaCE [Le Cam et al. 2015; 2017] in the continuity of this thesis work.

Finally from a clinical point of view, this study might be considered as a milestone toward an harmonization of SEEG setup implantation. Indeed, as defended in this thesis, a limited number of sensors properly spread over the brain volume is sufficient to identify any active source within the gray matter (provided a sufficient SNR level is reach), at least within the zones of interest. The established customs of SEEG implantations are varying from a clinical neurophysiology center to another. Providing a guideline for a unified implantation scheme will help in facilitating the data sharing, the exchange of expertise as well as the formation of new comers to this modality. Ultimately, it would guarantee an optimal coverage of the brain structures for better understanding of the underlying epileptic mechanism as well as other neurophysiological questions such as the comprehension of the neuronal network at the basis of elaborated visual or auditory cerebral functions [Coito et al. 2015].

Bibliography

*, . . (2016). Distributing points on the sphere. School of Mathematis and Statistics, University of New South Wales, Sidney. 59

Achard, S., Salvador, R., Whitcher, B., Suckling, J., and Bullmore, E. (2006). A resilient, low-frequency, small-world human brain functional network with highly connected association cortical hubs. *The Journal of neuroscience*, 26(1):63–72. 23, 24

Albera, L., Kachenoura, A., Comon, P., Karfoul, A., Wendling, F., Senhadji, L., and Merlet, I. (2012). ICA-based EEG denoising: a comparative analysis of fifteen methods. *Bulletin of the Polish Academy of Sciences: Technical Sciences*, 60(3):407–418. 46

Altakroury, H., Koessler, L., Hofmanis, J., and Louis-Dorr, V. (2016). In vivo estimation of head conductivities frequency response with ies and seeg-eeg. *Neurophysiologie Clinique/Clinical Neurophysiology*, 46(2):78–79. 38

Ansari-Asl, K. (2005). *Mesure de couplage statistique entre signaux EEG: application à l'évaluation quantitative des relations fonctionnelles entre structures cérébrales en épilepsie*. PhD thesis, Université Rennes 1. ix, 24

Astrand, E., Wardak, C., and Ben Hamed, S. (2014). Selective visual attention to drive cognitive brain–machine interfaces: from concepts to neurofeedback and rehabilitation applications. *Frontiers in systems neuroscience*, 8:144. ix, 27

B. Ranck Jr., J. (1963). Specific impedance of rabbit cerebral cortex. *Experimental Neurology*, 7(2):144 – 152. 37

Babiloni, C., Frisoni, G. B., Pievani, M., Vecchio, F., Lizio, R., Buttiglione, M., Geroldi, C., Fracassi, C., Eusebi, F., Ferri, R., et al. (2009). Hippocampal volume and cortical sources of eeg alpha rhythms in mild cognitive impairment and alzheimer disease. *Neuroimage*, 44(1):123–135. 23

Baillet, S., Mosher, J. C., and Leahy, R. M. (2001). Electromagnetic brain mapping. *Signal Processing Magazine, IEEE*, 18(6):14–30. 40

Bangera, N. B., Schomer, D. L., Dehghani, N., Ulbert, I., Cash, S., Papavasiliou, S., Eisenberg, S. R., Dale, A. M., and Halgren, E. (2010). Experimental validation of the influence of white matter anisotropy on the intracranial EEG forward solution. *Journal of Computational Neuroscience*, 29(3):371–387. 37

Barkley, G. L. and Baumgartner, C. (2003). Meg and eeg in epilepsy. *Journal of clinical neurophysiology*, 20(3):163–178. 26

Bénar, C.-G., Grova, C., Kobayashi, E., Bagshaw, A. P., Aghakhani, Y., Dubeau, F., and Gotman, J. (2006). Eeg–fmri of epileptic spikes: concordance with eeg source localization and intracranial eeg. *Neuroimage*, 30(4):1161–1170. 29

Betts, J. G. e. a. (2013). Anatomy & physiology. *Open Stax College*. ix, 18

Birot, G., Spinelli, L., Vulliémoz, S., Mégevand, P., Brunet, D., Seeck, M., and Michel, C. M. (2014). Head model and electrical source imaging: a study of 38 epileptic patients. *NeuroImage: Clinical*, 5:77–83. 55, 107

Boggs, P. T. and Tolle, J. W. (1996). Sequential quadratic programming. *Acta Numerica*, pages 1–000. 44

Brody, D. A., Terry, F. H., and Ideker, R. (1973). Eccentric dipole in a spherical medium: generalized expression for surface potentials. *Biomedical Engineering, IEEE Transactions on*, BME-20(2):141–143. 35

Bromfield, E. B., Cavazos, J. E., and Sirven, J. I. (2006). Basic mechanisms underlying seizures and epilepsy. 23

Bullmore, E. and Sporns, O. (2009). Complex brain networks: graph theoretical analysis of structural and functional systems. *Nature Reviews Neuroscience*, 10(3):186–198. 24

Burger, H. C. and van Milaan, J. B. (1943). Measurements of the specific resistance of the human body to direct current. *Acta Medica Scandinavica*, 114(6):584–607. 38

Buzsáki, G. and Watson, B. O. (2012). Brain rhythms and neural syntax: implications for efficient coding of cognitive content and neuropsychiatric disease. *Dialogues Clin Neurosci*, 14(4):345–367. ix, 22

Chang, N., Gulrajani, R., and Gotman, J. (2005). Dipole localization using simulated intracerebral EEG. *Clinical neurophysiology : official journal of the International Federation of Clinical Neurophysiology*, 116(11):2707–2716. 29, 45

Chatrian, G., Lettich, E., and Nelson, P. (1985). Ten percent electrode system for topographic studies of spontaneous and evoked eeg activities. *American Journal of EEG technology*, 25(2):83–92. 28

Cho, J.-H., Hong, S. B., Jung, Y.-J., Kang, H.-C., Kim, H. D., Suh, M., Jung, K.-Y., and Im, C.-H. (2011). Evaluation of algorithms for intracranial eeg (ieeg) source imaging of extended sources: feasibility of using ieeg source imaging for localizing epileptogenic zones in secondary generalized epilepsy. *Brain topography*, 24(2):91–104. 29

Chui, C. K. (2014). *An introduction to wavelets*, volume 1. Academic press. 46

Cohen, D. et al. (1968). Magnetoencephalography: evidence of magnetic fields produced by alpha-rhythm currents. *Science*, 161(3843):784–786. 26

Coito, A., Plomp, G., Genetti, M., Abela, E., Wiest, R., Seeck, M., Michel, C. M., and Vulliemoz, S. (2015). Dynamic directed interictal connectivity in left and right temporal lobe epilepsy. *Epilepsia*, 56(2):207–217. 107

Cosandier-Rimélé, D., Badier, J.-M., Chauvel, P., and Wendling, F. (2007). A physiologically plausible spatio-temporal model for EEG signals recorded with intracerebral electrodes in human partial epilepsy. *IEEE transactions on biomedical engineering*, 54(3):380–8. 38, 56

Cuffin, B. N. (1991). Eccentric spheres models of the head. *Biomedical Engineering, IEEE Transactions on*, 38(9):871–878. 36

Dannhauer, M., Lanfer, B., Wolters, C. H., and Knösche, T. R. (2011). Modeling of the human skull in EEG source analysis. *Human brain mapping*, 32(9):1383–1399. 37

de Curtis, M. and Avanzini, G. (2001). Interictal spikes in focal epileptogenesis. *Progress in neurobiology*, 63(5):541–567. 49

de Peralta Menendez, R. G., Andino, S. G., Lantz, G., Michel, C. M., and Landis, T. (2001). Noninvasive localization of electromagnetic epileptic activity. I. method descriptions and simulations. *Brain topography*, 14(2):131–137. 41

de Peralta Menendez, R. G., Hauk, O., Andino, S. G., Vogt, H., and Michel, C. (1997). Linear inverse solutions with optimal resolution kernels applied to electromagnetic tomography. *Human brain mapping*, 5(6):454–467. 40

Debener, S., Minow, F., Emkes, R., Gandras, K., and Vos, M. (2012). How about taking a low-cost, small, and wireless eeg for a walk? *Psychophysiology*, 49(11):1617–1621. 28

Dümpelmann, M., Fell, J., Wellmer, J., Urbach, H., and Elger, C. E. (2009). 3d source localization derived from subdural strip and grid electrodes: a simulation study. *Clinical neurophysiology : official journal of the International Federation of Clinical Neurophysiology*, 120(6):1061–9. 29

Dümpelmann, M., Ball, T., and Schulze-Bonhage, A. (2012). sLORETA allows reliable distributed source reconstruction based on subdural strip and grid recordings. *Human brain mapping*, 33(5):1172–1188. 29

Eysenck, H. J. (1958). *Introduction To Psychology*, volume 2. Flat World Knowledge. ix, 16, 19

Ferree, T. C., Eriksen, K. J., and Tucker, D. M. (2000). Regional head tissue conductivity estimation for improved EEG analysis. *Biomedical Engineering, IEEE Transactions on*, 47(12):1584–1592. 37

Fonov, V., Evans, A. C., Botteron, K., Almli, C. R., McKinstry, R. C., and Collins, D. L. (2011). Unbiased average age-appropriate atlases for pediatric studies. *NeuroImage*, 54(1):313 – 327. 54

Frank, E. (1952). Electric potential produced by two point current sources in a homogeneous conducting sphere. *Journal of Applied Physics*, 23(11):1225–1228. 35

Friston, K. J., Holmes, A. P., Poline, J., Grasby, P., Williams, S., Frackowiak, R. S., and Turner, R. (1995). Analysis of fmri time-series revisited. *Neuroimage*, 2(1):45–53. 26

Fuchs, M., Wagner, M., and Kastner, J. (2004). Confidence limits of dipole source reconstruction results. *Clinical Neurophysiology*, 115(6):1442 – 1451. 42

Geddes, L. and Baker, L. (1967). The specific resistance of biological material – a compendium of data for the biomedical engineer and physiologist. *Medical and biological engineering*, 5(3):271–293. 38, 55

Geselowitz, D. (1998). The zero of potential. *IEEE engineering in medicine and biology magazine : the quarterly magazine of the Engineering in Medicine & Biology Society*, 17(1):128132. 47

Gharib, S., Sutherling, W. W., Nakasato, N., Barth, D. S., Baumgartner, C., Alexopoulos, N., Taylor, S., and Rogers, R. L. (1995). Meg and ecog localization accuracy test. *Electroencephalography and clinical neurophysiology*, 94(2):109–114. 29

Glover, F. and Kochenberger, G. A. (2003). *Handbook of metaheuristics*. Springer Science & Business Media. 44

Gorodnitsky, I. F., George, J. S., and Rao, B. D. (1995). Neuromagnetic source imaging with FOCUSS: a recursive weighted minimum norm algorithm. *Electroencephalography and Clinical Neurophysiology*, 95(4):231 – 251. 40

Gotman, J. (2008). Epileptic networks studied with eeg-fmri. *Epilepsia*, 49(s3):42–51. 26

Greenblatt, R. E. (1993). Probabilistic reconstruction of multiple sources in the bioelectromagnetic inverse problem. *Inverse Problems*, 9(2):271. 40

Hallez, H., Vanrumste, B., Grech, R., Muscat, J., De Clercq, W., Vergult, A., D'Asseler, Y., Camilleri, K. P., Fabri, S. G., Van Huffel, S., and Others (2007). Review on solving the forward problem in eeg source analysis. *Journal of NeuroEngineering and Rehabilitation*, 4(1):46. ix, 19

Hämäläinen, M. S. and Ilmoniemi, R. (1994). Interpreting magnetic fields of the brain: minimum norm estimates. *Medical & biological engineering & computing*, 32(1):35–42. 40

Hansen, P. C. (1999). *The L-curve and its use in the numerical treatment of inverse problems*. IMM, Department of Mathematical Modelling, Technical Universityof Denmark. 40

Haueisen, J., Tuch, D., Ramon, C., Schimpf, P., Wedeen, V., George, J., and Belliveau, J. (2002). The influence of brain tissue anisotropy on human EEG and MEG. *NeuroImage*, 15(1):159 – 166. 37

Hayes, B. (2013). Les grappes de sphères collantes. *Pour la Science*, (427):64–71. 59

Hoekema, R., Wieneke, G., Leijten, F., van Veelen, C., van Rijen, P., Huiskamp, G., Ansems, J., and van Huffelen, A. (2003). Measurement of the conductivity of skull, temporarily removed during epilepsy surgery. *Brain Topography*, 16(1):29–38. 37

Hofmanis, J. (2013). *Contribution to the cerebral forward model by depth electric stimulation and SEEG measurements : application in epilepsy*. PhD thesis, Ecole doctorale IAEM Lorraine. ix, 24, 37, 53, 55

Hofmanis, J., Caspary, O., Louis-Dorr, V., Ranta, R., and Maillard, L. (2013). Denoising depth eeg signals during dbs using filtering and subspace decomposition. *Biomedical Engineering, IEEE Transactions on*, 60(10):2686–2695. 69

Hofmanis, J., Louis-Dorr, V., Caspary, O., and Maillard, L. (2011). Automatic depth electrode localization in intracranial space. In *BIOSIGNALS*, pages 459–462. 24, 31, 38, 69

Hu, S., Stead, M., and Worrell, G. A. (2007). Automatic identification and removal of scalp reference signal for intracranial EEGs based on independent component analysis. *Biomedical Engineering, IEEE Transactions on*, 54(9):1560–1572. 48

Hu, S., Stead, M., and Worrell, G. A. (2008). Removal of scalp reference signal and line noise for intracranial EEGs. In *Networking, Sensing and Control, 2008. ICNSC 2008. IEEE International Conference on*, pages 1486–1491. IEEE. 48

Huang, M., Mosher, J., and Leahy, R. (1999). A sensor-weighted overlapping-sphere head model and exhaustive head model comparison for MEG. *Physics in medicine and biology*, 44(2):423. 36

Hyvärinen, A. and Oja, E. (2000). Independent component analysis: algorithms and applications. *Neural Networks*, 13(45):411 – 430. 46

Khosla, D., Don, M., and Kwong, B. (1999). Spatial mislocalization of EEG electrodes effects on accuracy of dipole estimation. *Clinical Neurophysiology*, 110(2):261 – 271. 38

Kobayashi, E., Bagshaw, A. P., Bénar, C.-G., Aghakhani, Y., Andermann, F., Dubeau, F., and Gotman, J. (2006). Temporal and extratemporal bold responses to temporal lobe interictal spikes. *Epilepsia*, 47(2):343–354. 26

Kobayashi, K., Yoshinaga, H., Ohtsuka, Y., and Gotman, J. (2005). Dipole modeling of epileptic spikes can be accurate or misleading. *Epilepsia*, 46(3):397–408. 20

Koessler, L., Benar, C., Maillard, L., Badier, J.-M., Vignal, J. P., Bartolomei, F., Chauvel, P., and Gavaret, M. (2010a). Source localization of ictal epileptic activity investigated by high resolution eeg and validated by seeg. *Neuroimage*, 51(2):642–653. 29

Koessler, L., Cecchin, T., Caspary, O., Benhadid, A., Vespignani, H., and Maillard, L. (2011). Eeg–mri co-registration and sensor labeling using a 3d laser scanner. *Annals of biomedical engineering*, 39(3):983–995. 38

Koessler, L., Colnat-Coulbois, S., Cecchin, T., Hofmanis, J., Dmochowski, J. P., Norcia, A. M., and Maillard, L. G. (2017). In-vivo measurements of human brain tissue conductivity using focal electrical current injection through intracerebral multicontact electrodes. *Human Brain Mapping*, 38(2):974–986. 38

Koessler, L., Salido-Ruiz, R., Ranta, R., Louis-Dorr, V., Gavaret, M., and Maillard, L. (2010b). Influence of source separation and montage on ictal source localization. In *Engineering in Medicine and Biology Society (EMBC), 2010 Annual International Conference of the IEEE*, pages 2898–2901. 47

Korats, G. (2016). *Estimation de sources corticales : du montage laplacian aux solutions parcimonieuses (Cortical source imaging : from the laplacian montage to sparse inverse solutions)*. PhD thesis, Citeseer. 41

Kosterich, J. D., Foster, K. R., and Pollack, S. R. (1983). Dielectric permittivity and electrical conductivity of fluid saturated bone. *Biomedical Engineering, IEEE Transactions on*, (2):81–86. 38

Kucewicz, M. T., Cimbalnik, J., Matsumoto, J. Y., Brinkmann, B. H., Bower, M. R., Vasoli, V., Sulc, V., Meyer, F., Marsh, W., Stead, S. M., et al. (2014). High frequency oscillations are associated with cognitive processing in human recognition memory. *Brain*, page awu149. 21

Kuijlaars, A. B. J. and Saff, E. B. (1998). Asymptotics for minimal discrete energy on the sphere. *Transactions of the American Mathematical Society*, 350(2):523–538. 59

Lagarias, J. C., Reeds, J. a., Wright, M. H., and Wright, P. E. (1998). Convergence properties of the Nelder–Mead Simplex method in low dimensions. *SIAM Journal on Optimization*, 9(1):112–147. 44

Lawson, C. L. and Hanson, R. J. (1974). *Solving least squares problems*, volume 161. SIAM. 40

Le Cam, S., Caune, V., Ranta, R., Korats, G., and Louis-Dorr, V. (2015). Combining bayesian source imaging with equivalent dipole approach to solve the intracranial eeg source localization problem. In *Engineering in Medicine and Biology Society (EMBC), 2015 37th Annual International Conference of the IEEE*, pages 642–645. IEEE. 107

Le Cam, S., Ranta, R., Caune, V., Korats, G., Koessler, L., Maillard, L., and Louis-Dorr, V. (2017). Seeg dipole source localization based on an empirical bayesian approach taking into account forward model uncertainties. *NeuroImage*, 153:1–15. 107

Madhu, N., Ranta, R., Maillard, L., and Koessler, L. (2012). A unified treatment of the reference estimation problem in depth EEG recordings. *Medical & Biological Engineering & Computing*, 50(10):1003 – 1015. 48, 49

Maillard, L., Vignal, J.-P., Gavaret, M., Guye, M., Biraben, A., McGonigal, A., Chauvel, P., and Bartolomei, F. (2004). Semiologic and electrophysiologic correlations in temporal lobe seizure subtypes. *Epilepsia*, 45(12):1590–1599. 23

Menon, V. (2012). *Resting state brain activity: Implications for systems neuroscience*. Frontiers E-books. 46

Michel, C. M., Lantz, G., Spinelli, L., de Peralta, R. G., Landis, T., and Seeck, M. (2004a). 128-channel EEG source imaging in epilepsy: clinical yield and localization precision. *Journal of Clinical Neurophysiology*, 21(2):71–83. 41

Michel, C. M., Murray, M. M., Lantz, G., Gonzalez, S., Spinelli, L., and de Peralta, R. (2004b). EEG source imaging. *Clinical neurophysiology*, 115(10):2195–2222. 40, 41, 42

Mosher, J. C. and Leahy, R. M. (1998). Recursive MUSIC: a framework for EEG and MEG source localization. *Biomedical Engineering, IEEE Transactions on*, 45(11):1342–1354. 41

Mosher, J. C., Lewis, P. S., and Leahy, R. M. (1992). Multiple dipole modeling and localization from spatio-temporal MEG data. *IEEE Transactions on Biomedical Engineering*, 39(6):541–557. 41

Mountcastle, V. B. (1997). The columnar organization of the neocortex. *Brain*, 120(4):701–722. 17

Munck, d. J. and Peters, M. J. (1993). A fast method to compute the potential in the multisphere model. *IEEE transactions on biomedical engineering*, 40(11):1166–1174. 36

Nelder, J. A. and Mead, R. (1965). A simplex method for function minimization. *The computer journal*, 7(4):308–313. 44

Neufeld, M., Blumen, S., Aitkin, I., Parmet, Y., and Korczyn, A. (1994). Eeg frequency analysis in demented and nondemented parkinsonian patients. *Dementia and Geriatric Cognitive Disorders*, 5(1):23–28. 23

Nicholson, P. W. (1965). Specific impedance of cerebral white matter. *Experimental Neurology*, 13(4):386–401. 37

Nocedal, J. and Wright, S. (2006). *Numerical optimization*. Springer Science & Business Media. 43

Okada, Y. (1985). Discrimination of localized and distributed current dipole sources and localized single and multiple sources. *Biomagnetism: Applications and Theory*, pages 266–272. 40

Oostendorp, T., Delbeke, J., and Stegeman, D. F. (2000). The conductivity of the human skull: results of in vivo and in vitro measurements. *Biomedical Engineering, IEEE Transactions on*, 47(11):1487–1492. 37, 38

Oostenveld, R. and Praamstra, P. (2001). The five percent electrode system for high-resolution eeg and erp measurements. *Clinical neurophysiology*, 112(4):713–719. 28

Palmini, A. (2006). The concept of the epileptogenic zone: a modern look at penfield and jaspers views on the role of interictal spikes. *Epileptic disorders*, 8(2):10–15. 27

Pascual-Marqui, R., Michel, C., and Lehmann, D. (1994). Low resolution electromagnetic tomography: a new method for localizing electrical activity in the brain. *International Journal of Psychophysiology*, 18(1):49 – 65. 41

Pascual-Marqui, R. D. (2007). Discrete, 3D distributed, linear imaging methods of electric neuronal activity. part 1: exact, zero error localization. *ArXiv e-prints*. 41

Penfield, W. and Boldrey, E. (1937). Somatic motor and sensory representation in the cerebral cortex of man as studied by electrical stimulation. *Brain: A journal of neurology*. 17

Peralta-Menendez, D., Gonzalez-Andino, S. L., et al. (1998). A critical analysis of linear inverse solutions to the neuroelectromagnetic inverse problem. *Biomedical Engineering, IEEE Transactions on*, 45(4):440–448. 40

Quiroga, R. and Garcia, H. (2003). Single-trial event-related potentials with wavelet denoising. *Clinical Neurophysiology*, 114(2):376 – 390. 46

Ramantani, G., Cosandier-Rimélé, D., Schulze-Bonhage, A., Maillard, L., Zentner, J., and Dümpelmann, M. (2013). Source reconstruction based on subdural eeg recordings adds to the presurgical evaluation in refractory frontal lobe epilepsy. *Clinical Neurophysiology*, 124(3):481–491. 29

Ranta, R., Le Cam, S., Tyvaert, L., and Louis-Dorr, V. (2017). Assesing human brain impedance using simultaneous surface and intracerebral recordings. *Neuroscience*, 343:411–422. 32

Ranta, R. and Madhu, N. (2012). Reference estimation in EEG: Analysis of equivalent approaches. *Signal Processing Letters, IEEE*, 19(1):12–15. 46, 48

Ranta, R., Salido-Ruiz, R., and Louis-Dorr, V. (2010). Reference estimation in EEG recordings. In *Engineering in Medicine and Biology Society (EMBC), 2010 Annual International Conference of the IEEE*, pages 5371–5374. IEEE. 48

Renard, Y., Lotte, F., Gibert, G., Congedo, M., Maby, E., Delannoy, V., Bertrand, O., and Lécuyer, A. (2010). Openvibe: An open-source software platform to design, test, and use brain–computer interfaces in real and virtual environments. *Presence*, 19(1):35–53. 28

Rivet, B., Souloumiac, A., Attina, V., and Gibert, G. (2009). xDAWN algorithm to enhance evoked potentials: Application to brain-computer interface. *Biomedical Engineering, IEEE Transactions on*, 56(8):2035–2043. 49

Romo Vazquez, R. d. C. (2010). *Contribution à la détection et à l'analyse des signaux EEG épileptiques: débruitage et séparation de sources*. PhD thesis, Vandoeuvre-les-Nancy, INPL. 107

Roth, B. J., Balish, M., Gorbach, A., and Sato, S. (1993). How well does a three-sphere model predict positions of dipoles in a realistically shaped head? *Electroencephalography and Clinical Neurophysiology*, 87(4):175 – 184. 36

Rush, S. and Driscoll, D. A. (1968). Current distribution in the brain from surface electrodes. *Anesthesia & Analgesia*, 47(6):717–723. 37

Salido-Ruiz, R. A. (2012). *Problèmes inverses contraints en EEG : applications aux potentiels absolus et ' a l influence du signal de r t' dans l analyse de l EEG*. PhD thesis, Université de Lorraine. 49

Sardouie, S. H., Shamsollahi, M. B., Albera, L., and Merlet, I. (2015). Interictal EEG noise cancellation: GEVD and DSS based approaches versus ICA and DCCA based methods. *IRBM*, 36(1):20–32. 49

Sarvas, J. (1987). Basic mathematical and electromagnetic concepts of the biomagnetic inverse problem. *Physics in medicine and biology*, 32(1):11. 34

Scherg, M. (1990). Fundamentals of dipole source potential analysis. *Auditory evoked magnetic fields and electric potentials. Advances in audiology*, 6:40–69. 42

Sekihara, K., Nagarajan, S. S., Poeppel, D., Marantz, A., and Miyashita, Y. (2001). Reconstructing spatio-temporal activities of neural sources using an MEG vector beamformer technique. *IEEE transactions on bio-medical engineering*, 48(7):760–71. 41

Sharbrough, F. W. (2005). Chapter 12: Nonspecific abnormal eeg patterns. *Electroencephalography: basic principles, clinical applications, and related fields*, pages 197–215. 22

Sholl, D. A. (1956). The organization of the cerebral cortex. 16

Swan, M. (2012). Sensor mania! the internet of things, wearable computing, objective metrics, and the quantified self 2.0. *Journal of Sensor and Actuator Networks*, 1(3):217–253. 28

Swartz, B., Tomiyasu, U., Delgado-Escueta, A., Mandelkern, M., and Khonsari, A. (1992). Neuroimaging in temporal lobe epilepsy: test sensitivity and relationships to pathology and postoperative outcome. *Epilepsia*, 33(4):624–634. 25, 26

Talairach, J., David, M., and Tournoux, P. (1958). *L'exploration chirurgicale stéréotaxique du lobe temporal dans l'épilepsie temporale: repérage anatomique stéréotaxique et technique chirurgicale*. Masson. 28

Tao, J. X., Ray, A., Hawes-Ebersole, S., and Ebersole, J. S. (2005). Intracranial eeg substrates of scalp eeg interictal spikes. *Epilepsia*, 46(5):669–676. 20

Tesche, C. and Karhu, J. (2000). Theta oscillations index human hippocampal activation during a working memory task. *Proceedings of the National Academy of Sciences*, 97(2):919–924. 21

Towle, V. L., Bolaños, J., Suarez, D., Tan, K., Grzeszczuk, R., Levin, D. N., Cakmur, R., Frank, S. A., and Spire, J.-P. (1993). The spatial location of EEG electrodes: locating the best-fitting sphere relative to cortical anatomy. *Electroencephalography and Clinical Neurophysiology*, 86(1):1 – 6. 38

Urigüen, J. A. and Garcia-Zapirain, B. (2015). Eeg artifact removalstate-of-the-art and guidelines. *Journal of neural engineering*, 12(3):031001. ix, 20

Vallaghé, S. (2008). *EEG and MEG forward modeling : computation and calibration*. PhD thesis, University of Nice-Sophia Antipolis. 37, 55

Van Harreveld, A., Murphy, T., and Nobel, K. (1963). Specific impedance of rabbit's cortical tissue. *American Journal of Physiology–Legacy Content*, 205(1):203–207. 37

Van Hoey, G., Vanrumste, B., D'Havé, M., Van de Walle, R., Lemahieu, I., and Boon, P. (2000). Influence of measurement noise and electrode mislocalisation on EEG dipole-source localisation. *Medical and Biological Engineering and Computing*, 38(3):287–96. 38, 45

Varela, F., Lachaux, J.-P., Rodriguez, E., and Martinerie, J. (2001). The brainweb: phase synchronization and large-scale integration. *Nature reviews neuroscience*, 2(4):229–239. 21

Vespignani, H. (2003). *L'EEG: de la technique à la clinique*. John Libbey Eurotext. 21

von Ellenrieder, N., Beltrachini, L., and Muravchik, C. H. (2012a). Electrode and brain modeling in stereo-eeg. *Clinical Neurophysiology*, 123(9):1745–1754. 29

von Ellenrieder, N., Beltrachini, L., and Muravchik, C. H. (2012b). Electrode and brain modeling in stereo-EEG. *Clinical neurophysiology : official journal of the International Federation of Clinical Neurophysiology*, 123(9):1745–1754. 38, 45, 55

Vulliemoz, S., Thornton, R., Rodionov, R., Carmichael, D. W., Guye, M., Lhatoo, S., McEvoy, A. W., Spinelli, L., Michel, C. M., Duncan, J. S., et al. (2009). The spatio-temporal mapping of epileptic networks: combination of eeg–fmri and eeg source imaging. *Neuroimage*, 46(3):834–843. 26

Vázquez, R. R., Vélez-Pérez, H., Ranta, R., Dorr, V. L., Maquin, D., and Maillard, L. (2012). Blind source separation, wavelet denoising and discriminant analysis for EEG artefacts and noise cancelling. *Biomedical Signal Processing and Control*, 7(4):389 – 400. 46, 47

Wang, Y. and Gotman, J. (2001). The influence of electrode location errors on EEG dipole source localization with a realistic head model. *Clinical Neurophysiology*, 112(9):1777 – 1780. 38

Wendling, F., Chauvel, P., Biraben, A., and Bartolomei, F. (2010). From intracerebral eeg signals to brain connectivity: identification of epileptogenic networks in partial epilepsy. *Frontiers in systems neuroscience*, 4:154. 23, 24

Wilson, F. N. and Bayley, R. H. (1950). The electric field of an eccentric dipole in a homogeneous spherical conducting medium. *Circulation*, 1(1):84–92. 35

Wilson, S. B. and Emerson, R. (2002). Spike detection: a review and comparison of algorithms. *Clinical Neurophysiology*, 113(12):1873–1881. 49

Wipf, D. and Nagarajan, S. (2009). A unified Bayesian framework for MEG/EEG source imaging. *NeuroImage*, 44(3):947 – 966. 41

Yao, D. (2000). Electric potential produced by a dipole in a homogeneous conducting sphere. *IEEE transactions on bio-medical engineering*, 47(7):964–966. 35

Yvert, B., Fischer, C., Bertrand, O., and Pernier, J. (2005). Localization of human supratemporal auditory areas from intracerebral auditory evoked potentials using distributed source models. *NeuroImage*, 28(1):140–53. 45

Zaveri, H. P., Pincus, S. M., Goncharova, I. I., Duckrow, R. B., Spencer, D. D., and Spencer, S. S. (2009). Localization-related epilepsy exhibits significant connectivity away from the seizure-onset area. *Neuroreport*, 20(9):891–895. 56

Zhang, Y., van Drongelen, W., Kohrman, M., and He, B. (2008). Three-dimensional brain current source reconstruction from intra-cranial ecog recordings. *NeuroImage*, 42(2):683–695. 29

Declaration

I herewith declare that I have produced this paper without the prohibited assistance of third parties and without making use of aids other than those specified; notions taken over directly or indirectly from other sources have been identified as such. This thesis has not previously been presented in identical or similar form to any other examination board.

May 23, 2017, Nancy

Abstract

The spatio-temporal analysis of brain activity has a large number of applications, from the comprehension of cognitive mechanisms to the study of pathologies such as epilepsy. Several modalities are commonly used in clinical investigations, such as imaging methods (CT,MRI) or measurements of the electro-magnetical activity (EEG, MEG). They differ in temporal and spatial resolution, as well as in cost of implementation and invasiveness for the patient. The EEG provides a good compromise as a noninvasive investigative approach providing a high temporal resolution. Numerous studies are based on the EEG measurements for solving the inverse problem. However, these recordings suffer from the severe attenuation of the electrical propagation through the skull bone as well as the addition of external artifacts. We would like to broaden the possibilities of source localization techniques by exploiting intra-cranial Stereo-EEG (SEEG) recordings, consisting of shaft electrodes implanted in the brain volume in the direct vicinity of the brain generators. This data thus benefits from a high signal to noise ratio compared to that observed in surface EEG. Nevertheless, the spatial repartition of the measurement points highly varies between EEG and SEEG, the necessary conditions required for successful brain source localizations from SEEG data remain to be studied.

We propose, in a first step, a feasibility study of source imaging from the SEEG, based on an equivalent current dipole inversion method associated with an analytical one-sphere propagation model, able to bring localization precision of the order of a few millimeters. Based on a typical SEEG clinical implantation, we evaluate the localization performance when different subsets of sensors are considered. In the presence of realistic noise, we observe that the addition of distant sensors with respect to the source can lead to a degradation of the localization accuracy. These conclusions lead us to propose a local sensor selection approach in order to optimize the reliability of the results. The strengths and weaknesses of this approach are analyzed, and rules of good use to assess the quality of a location are stated. This study is carried out based on a realistic simulation framework, for a relevant exploration of the different parameters impacting on the quality of the SEEG source imaging. The approaches are applied on SEEG recordings collected at the CHRU of Nancy to evaluate their performance when facing real measurements.

Keywords: SEEG, Source localization, Equivalent Current Dipole, Intra-cranial Stimulation, Epileptic Spikes

Résumé

L'étude spatio-temporelle de l'activité cérébrale a de multiples applications, de la compréhension des mécanismes cognitifs à l'étude des pathologies telle que l'épilepsie. Différentes modalités sont actuellement utilisées dans la recherche clinique, qu'il s'agisse de méthodes d'imagerie (CT, IRM) ou de mesures de l'activité électromagnétique (EEG, MEG). Ces techniques diffèrent en résolution spatiale et temporelle ainsi qu'en termes de coût et d'invasivité pour le patient. L'EEG offre un bon compromis en tant que méthode d'investigation non-invasive avec une résolution temporelle élevée. De nombreuses études se sont attachées à la résolution du problème inverse à partir de ces mesures de surface. Cependant, l'EEG souffre de la forte atténuation du champ électrique propagée à travers l'os du crâne et de la présence de sources de bruits externes. De ce fait, nous aimerions élargir l'éventail des possibilités en matière de techniques de localisation de sources par l'exploitation de données issues de la Stéréo-EEG (SEEG), qui consiste en l'introduction d'électrodes d'enregistrement au plus près des générateurs. Ces mesures bénéficient ainsi d'un rapport signal à bruit bien supérieur à celui observé en EEG. Néanmoins la disposition spatiale des capteurs est très différente entre EEG et SEEG, et il est nécessaire d'étudier les conditions favorables à une localisation concluante de l'activité cérébrale à partir de données SEEG.

Nous proposons dans un premier temps une étude de faisabilité de l'imagerie de sources à partir de la SEEG, basée sur une méthode d'inversion de type dipôle équivalent associée à un modèle de propagation à une sphère, capable d'amener à une précision de localisation de l'ordre de quelques millimètres. En se basant sur une implantation clinique usuelle de la SEEG, nous évaluons les performances de localisation lorsque différents sous-ensembles de capteurs sont considérés. En présence de bruit réaliste, nous constatons que l'ajout de capteurs lointains peut amener à une dégradation de la précision de localisation. Ces conclusions nous amènent à proposer une approche de sélection des capteurs locaux dans le but d'optimiser la fiabilité des résultats. Les atouts et faiblesses de cette approche sont analysés, et des règles de bon usage afin d'évaluer la qualité d'une localisation sont énoncées. L'ensemble de cette étude est menée dans un cadre de simulation réaliste afin d'explorer de façon pertinente les différents paramètres pouvant influer sur la qualité de résolution du problème inverse. Les approches sont appliquées sur des enregistrements SEEG récoltés au CHRU de Nancy afin de confronter les méthodes de localisation proposées à des mesures réelles.

Mots-Clés : SEEG, Localisation de sources, Dipôle Equivalent, Stimulation Intra-crânienne, Pointes Epileptiques